MINISTÉRIO DA CIÊNCIA, TECNOLOGIA E INOVAÇÕES
INSTITUTO NACIONAL DE PESQUISAS ESPACIAIS

sid.inpe.br/mtc-m21d/2022/07.14.13.58-TDI

ASSESSING THE PERFORMANCE OF PBL PARAMETERIZATION SCHEMES IN THE CENTRAL AMAZON BASIN DURING GOAMAZON2014/5

José Antonio Mantovani Júnior

Master's Dissertation of the Graduate Course in Meteorology, guided by Dr. Gilberto Fernando Fisch, approved in June 06, 2022.

URL of the original document:
<http://urlib.net/8JMKD3MGP3W34T/479FG98>

INPE
São José dos Campos
2022

PUBLISHED BY:

Instituto Nacional de Pesquisas Espaciais - INPE
Coordenação de Ensino, Pesquisa e Extensão (COEPE)
Divisão de Biblioteca (DIBIB)
CEP 12.227-010
São José dos Campos - SP - Brasil
Tel.:(012) 3208-6923/7348
E-mail: pubtc@inpe.br

MINISTÉRIO DA CIÊNCIA, TECNOLOGIA E INOVAÇÕES
INSTITUTO NACIONAL DE PESQUISAS ESPACIAIS

sid.inpe.br/mtc-m21d/2022/07.14.13.58-TDI

ASSESSING THE PERFORMANCE OF PBL PARAMETERIZATION SCHEMES IN THE CENTRAL AMAZON BASIN DURING GOAMAZON2014/5

José Antonio Mantovani Júnior

Master's Dissertation of the Graduate Course in Meteorology, guided by Dr. Gilberto Fernando Fisch, approved in June 06, 2022.

URL of the original document:
<http://urlib.net/8JMKD3MGP3W34T/479FG98>

INPE
São José dos Campos
2022

Cataloging in Publication Data

Mantovani Júnior, José Antonio.

M319a Assessing the performance of PBL parameterization schemes in the central Amazon basin during GOAmazon2014/5 / José Antonio Mantovani Júnior. – São José dos Campos : INPE, 2022.
xxvi + 126 p. ; (sid.inpe.br/mtc-m21d/2022/07.14.13.58-TDI)

Dissertation (Master in Meteorology) – Instituto Nacional de Pesquisas Espaciais, São José dos Campos, 2022.
Guiding : Dr. Gilberto Fernando Fisch.

1. Nonlocal PBL schemes. 2. Local PBL schemes. 3. Weather Research and Forecasting model. 4. Ceilometer. 5. Subgrid turbulence mixing. I.Title.

CDU 551.509.313(811)

MINISTÉRIO DA CIÊNCIA, TECNOLOGIA E INOVAÇÕES

INSTITUTO NACIONAL DE PESQUISAS ESPACIAIS

DEFESA FINAL DE DISSERTAÇÃO DA JOSÈ ANTONIO MANTOVANI JÙNIOR BANCA Nº174/2022 , REGISTRO 233844/2020.

No dia 06 de junho de 2022, as 10h00, Videoconferência, o(a) aluno(a) mencionado(a) acima defendeu seu trabalho final (apresentação oral seguida de arguição) perante uma Banca Examinadora, cujos membros estão listados abaixo. O(A) aluno(a) foi **APROVADO(A)** pela Banca Examinadora, por unanimidade, em cumprimento ao requisito exigido para obtenção do Título de Mestre em Meteorologia. O trabalho precisa da incorporação das correções sugeridas pela Banca e revisão final pelo(s) orientador(es).

Título: "Assessing the performance of PBL parameterization schemes in the central Amazon basin during GOAmazon2014/5".

Membros da Banca

Dr. Luiz Augusto Toledo Machado – Presidente - INPE

Dr. Gilberto Fernando Fisch – Orientador - INPE

Dr. José Augusto Paixão Veiga - Membro Externo - Estadual do Amazonas (UEA)

Documento assinado eletronicamente por **LUIZ AUGUSTO TOLEDO MACHADO (E)**, **Usuário Externo**, em 22/06/2022, às 15:18 (horário oficial de Brasília), com fundamento no § 3º do art. 4º do Decreto nº 10.543, de 13 de novembro de 2020.

Documento assinado eletronicamente por **gilberto fernando fisch (E)**, **Usuário Externo**, em 22/06/2022, às 22:03 (horário oficial de Brasília), com fundamento no § 3º do art. 4º do Decreto nº 10.543, de 13 de novembro de 2020.

Documento assinado eletronicamente por **José Augusto Paixão Veiga (E)**, **Usuário Externo**, em 23/06/2022, às 08:24 (horário oficial de Brasília), com fundamento no § 3º do art. 4º do Decreto nº 10.543, de 13 de novembro de 2020.

A autenticidade deste documento pode ser conferida no site http://sei.mctic.gov.br/verifica.html, informando o código verificador **9933261** e o código CRC **2A5736D4**.

Referência: Processo nº 01340.004147/2022-02 SEI nº 9933261

"Seja você quem for, seja qual for a posição social que você tenha na vida, a mais alta ou a mais baixa, tenha sempre como meta muita força, muita determinação e sempre faça tudo com muito amor e com muita fé em Deus, que um dia você chega lá. De alguma maneira você chega lá."

Ayrton Senna da Silva

A meus pais ***José Antonio*** *e* ***Miriam***

ACKNOWLEDGEMENTS

This study was financed in part by the Coordenação de Aperfeiçoamento de Pessoal de Nível Superior - Brasil (CAPES) - Finance Code 001, and I would like to thank the CAPES for the support and funding that allowed the execution of this research work.

I would also like to thank the National Institute for Space Research (INPE) and its Meteorology Graduate Program (PGMET) for hosting my Master degree's.

I would like to thank the Laboratório Nacional de Computação Científica (LNCC) for computational resources from the Santos Dumont supercomputer that allowed the execution of this research work.

I am extremely grateful to my supervisors Dr. Gilberto Fernando Fisch and Dr. José Antonio Aravéquia for all the help, advice, and encouragement during my Master's period.

I thank the GOAmazon2014/5 team for their effort to produce the observational data employed in this research.

I would like to express gratitude to all my colleagues, in special Dr. Rayonil Carneiro and Me. Luciano Ritter, which collaborates with this research.

Many thanks to my family for unconditionally loving, and encouraging my studies during my whole life.

ABSTRACT

Numerical weather prediction models include the effects of vertical subgrid-scale turbulence through planetary boundary layer (PBL) parameterization schemes, which performance relies on meteorological conditions and interest region features. Despite the recognized importance of PBL schemes to accurate weather forecasting, climate studies, and air quality modeling, few studies assessed its performance over the Amazon rainforest. This study compares eleven PBL schemes in the state-of-the-art Advanced Research WRF model version 4.2.2 for the 2014 and 2015 years (rainy and dry seasons) over the central Amazon basin. These PBL schemes include five nonlocal PBL schemes - the Medium Range Forecast model (MRF), the Yonsei University (YSU), the Asymmetrical Convective Model version 2 (ACM2), the Shin-Hong (SH), and the Quasi-Normal Scale Elimination with the eddy-diffusivity mass-flux term (QNSE-EDMF), and six local PBL schemes - the Bougeault-Lacarrere (BouLac), the Grenier-Bretherton-McCaa (GBM), the Mellor-Yamada-Nakanishi-Niino levels 2.5 (MYNN2.5) and 3 (MYNN3), the Mellor-Yamada-Janjic (MYJ), and the University of Washington (UW). The comparison results reveal differences amongst surface meteorological variables, turbulent fluxes, and PBL depth and vertical structures during both the daytime and nighttime. There is no single PBL scheme option that outperforms others in all evaluated variables, on the other hand, for each variable under different conditions (season/year) a specific PBL scheme shows a better performance. The 2-m air temperature is better predicted by nonlocal PBL schemes, while both 2-m relative humidity and 10-m wind speed are better predicted by local PBL schemes. Turbulent heat fluxes are also better predicted by TKE-based PBL schemes. The key variable related to PBL schemes, the PBL height (PBLH), was investigated and benchmarked by ceilometer measurements from the GOAmazon2014/5 campaign. Both local MYNN2.5 and MYNN3 and hybrid QNSE schemes produced deeper PBL in both nocturnal and diurnal periods in all evaluated periods. In general, local PBL schemes produced better results during the daytime, and a nonlocal PBL scheme predicted the PBLH with better performance at night in most cases. The PBLH spatial distribution was also investigated and differences between daytime and nighttime period were found, with nonlocal PBL schemes presenting a behavior influenced by the basin hydrography. In short, the PBLH is deeper above the land and shallower above rivers during the daytime and the opposite at night.

Keywords: Nonlocal PBL schemes. Local PBL schemes. Weather Research and Forecasting model. Ceilometer. Subgrid turbulence mixing.

AVALIAÇÃO DO DESEMPENHO DE ESQUEMAS DE PARAMETRIZAÇÃO DE CLP NA REGIÃO CENTRAL DA BACIA AMAZÔNICA DURANTE O GOAMAZON2014/5

RESUMO

A previsão numérica do tempo inclui o efeito da turbulência vertical de escala subgrade através de esquemas de parametrização de camada limite planetária (CLP), os quais o desempenho depende das condições meteorológicas e características da região de interesse. Apesar da reconhecida importância dos esquemas de parametrização de CLP para a acurácia de previsões de tempo, estudos climáticos e modelagem da qualidade do ar, poucos estudos avalariam seu desempenho sobre a floresta tropical Amazônica. O estudo compara onze esquemas de parametrização de CLP no modelo estado da arte Advanced Research WRF versão 4.2.2 para as estações (chuvosa e seca) de 2014 e 2015 sobre a região central da bacia Amazônica. Os onze esquemas de parametrização de CLP incluem cinco esquemas não locais de parametrização de CLP - o Medium Range Forecast model (MRF), o Yonsei University (YSU), o Asymmetrical Convective Model version 2 (ACM2), o Shin-Hong (SH) e o Quasi-Normal Scale Elimination com termo de difusividade e fluxo de massa (QNSE-EDMF), e seis esquemas locais de parametrização de CLP - o Bougeault-Lacarrere (BouLac), o Grenier-Bretherton-McCaa (GBM), o Mellor-Yamada-Nakanishi-Niino níveis 2.5 (MYNN2.5) e 3 (MYNN3), o Mellor-Yamada-Janjic (MYJ), e o University of Washington (UW). Os resultados comparativos revelaram diferenças entre as variáveis meteorológicas de superfície, os fluxos turbulentos e a profundidade e estruturas verticais da CLP durante o dia e à noite. Não há um único esquema de parametrização de CLP que supera o desempenho de todos os outros em todas as variáveis avaliadas, por outro lado, para cada variável sob diferentes condições (estação/ano) um esquema de parametrização de CLP específico mostra um melhor desempenho. A temperatura do ar em 2 m é melhor prevista pelos esquemas não locais de CLP, enquanto que tanto a umidade relativa do ar em 2 m como a velocidade do vento em 10 m são melhor previstas pelos esquemas locais de CLP. Os fluxos de calor turbulentos também são melhor previstos pelos esquemais locais de CLP. A variável chave relacionada aos esquemas CLP, a altura da CLP (CLPH), foi investigada e referenciada por medições de ceilômetro da campanha GOAmazon2014/5. Tanto os esquemas locais MYNN2.5 e MYNN3 como o esquema híbrido QNSE produziram uma CLP mais profunda tanto em períodos noturnos quanto diurnos em todos os períodos avaliados. Em geral, os esquemas locais de CLP produziram resultados melhores durante o dia, e um esquemas não local de CLP previu a CLPH com melhor desempenho à noite na maioria dos casos. A distribuição espacial da CLPH também foi investigada e foram encontradas diferenças entre o período diurno e o noturno, com alguns esquemas de CLP apresentando um comportamento influenciado pela hidrografia da bacia. Em resumo, a CLPH é mais profunda acima da terra e mais rasa acima dos rios durante o dia e o oposto durante à noite.

Palavras-chave: Esquemas não locais de CLP. Esquemas locais de CLP. Modelo Weather Research and Forecasting. Ceilômetro. Mistura turbulenta de escala subgrade.

LIST OF FIGURES

Page

LIST OF TABLES

Page

LIST OF ABBREVIATIONS

BL	–	Boundary Layer
PBL	–	Planetary Boundary Layer
PBLH	–	Planetary Boundary Layer Height
CBL	–	Convective Boundary Layer
SBL	–	Stable Boundary Layer
ML	–	Mixed Layer
SL	–	Surface Layer
LS	–	Land Surface
TKE	–	Turbulent Kinect Energy
LES	–	Large Eddy Simulation
WRF	–	Weather Research and Forecasting model
ARW	–	Advanced Research WRF model
NWP	–	Numerical Weather Prediction
GOAmazon2014/5	–	Observations and Modeling of the Green Ocean Amazon
T3	–	main GOAmazon2014/5 research site
DOE	–	U.S. Department of Energy
ARM	–	Atmospheric Radiation Measurement
AMF	–	ARM Mobile Facility
IOP	–	Intensive Operating Periods
LT	–	Local Time
ENSO	–	El Niño-Southern Oscillation
GFS	–	Global Forecast System
NCEP	–	National Center for Environmental Prediction
RK3	–	Third-order Runge Kutta time-integration scheme
UTC	–	Universal Time Coordinated
INPE	–	Instituto Nacional de Pesquisas Espaciais
CPTEC	–	Centro de Previsão do Tempo e Estudos Climáticos
CPT-WRF	–	Operational version of WRF model from CPTEC
SDumont	–	Santos Dumont supercomputer
LNCC	–	Laboratório Nacional de Computação Científica
EDMF	–	Eddy-Diffusivity Mass-Flux approach
ACM2	–	Assymetrical Convective Model 2 PBL scheme
BouLac	–	Bougeault and Lacarrére PBL scheme
GBM	–	Grenier-Bretherton-McCaa PBL scheme
MRF	–	Medium Range Forecast model PBL scheme
MYNN2.5	–	Mellor-Yamada-Nakanishi-Niino Level 2.5 PBL scheme
MYNN3	–	Mellor-Yamada-Nakanishi-Niino Level 3 PBL scheme
MYJ	–	Mellor-Yamada-Janjic PBL scheme
QNSE	–	Quasi-Normal Scale Elimination PBL scheme
SH	–	Shing-Hong PBL scheme
UW	–	University of Washington PBL scheme
YSU	–	Yonsei University PBL scheme

LIST OF SYMBOLS

ρ	–	air density
ν	–	kinematic viscosity
θ	–	potential temperature
q	–	vapor mixing ratio
U	–	horizontal wind speed or zonal velocity component (indicated when used)
V	–	meridional velocity component
W	–	vertical velocity component
t	–	time
Δ	–	horizontal grid resolution
Δt	–	time-step
l_ϵ	–	energy-containing turbulence scales (length scale)
C	–	atmospheric variables (u, v, θ, q)
S_i	–	sources and sinks term
Ri	–	Richardson number
Ri_{cr}	–	critical Richardson number
Rib	–	bulk Richardson number
Rig	–	gradient Richardson number
K_c	–	eddy viscosity coefficient $(c : m, h, H, V)$
e	–	TKE intensity
ϵ	–	TKE dissipation
Pr	–	Prandlt number
l	–	mixing length scale
S	–	absolute magnitude shear
T_2	–	2-m air temperature
RH_2	–	2-m relative humidity
U_{10}	–	10-m wind speed
H	–	sensible heat flux
LE	–	latent heat flux
u_*	–	friction velocity
τ	–	momentum flux
PBLH	–	PBL height
h	–	either above ground height or PBLH (indicated when used)
PCP	–	precipitation

CONTENTS

1 INTRODUCTION

Numerical Weather Prediction (NWP) models do not explicitly resolve physical subgrid-scale processes due to constraints associated with the numerical resolution, for instance, the computing resource capabilities and their expensive costs. Therefore, different parameterization schemes handle these subgrid-scale processes during the model run and are a component of primary importance (STENSRUD, 2009; DZEBRE; ADARAMOLA, 2020). NWP uncertainties have several sources such as governing equations and their numerical implementations, initial conditions, data assimilation, adopted domain properties, grid resolution, and parameterization schemes (OLAFSSON; BAO, 2020; LANGE et al., 2021a). Among physical subgrid-scale processes, subgrid turbulence mixing is one principal source of uncertainty in NWP models (ZHANG, 2021). Turbulence is the mechanism responsible for the vertical exchange of momentum, heat, humidity, and pollutants in the Planetary Boundary Layer (PBL) (STULL, 1988) and plays a key role in the PBL development, evolution, and daily cycle (BOPAPE et al., 2021). A PBL parameterization scheme includes unresolved turbulence effects in NWP models diagnosing vertical mixing in terms of model-resolved variables (STENSRUD, 2009).

Accurate prognostic of boundary layer parameters has recognized importance given its impacts on near-surface forecasting and long-term climate simulations, moreover are essential to achieve both realistic forecast and air quality prediction (SOARES et al., 2004; HU et al., 2010). The PBL height (PBLH) is a key variable that determines many atmospheric processes with impacts on a wide range of studies that use it as a key length scale (LIU; LIANG, 2010). PBL scheme affects the accuracy of predicted PBLH, consequently, other meteorological parameters are impacted and their choice may cause significant differences in predicted variables (LANGE et al., 2021a). Furthermore, both the optimum selection and performance of PBL schemes rely upon intrinsic features of the interest region and season of the year (YANG et al., 2021). Recent studies highlight the importance of simulations validation with observational data and the development of sensitivity analysis to optimally setup the model choosing the suitable parameterization schemes (LANGE et al., 2021a; LANGE et al., 2021b).

PBL parameterization schemes improved over the last decades covering different atmospheric stability regimes and PBL features (LOUIS, 1979; MELLOR; YAMADA, 1982; BOUGEAULT; LACARRERE, 1989; JANJIĆ, 1990; HONG; PAN, 1996; GRENIER; BRETHERTON, 2001; SUKORIANSKY et al., 2005; HONG et al., 2006; PLEIM, 2007a;

NAKANISHI; NIINO, 2009; ANGEVINE et al., 2010; SHIN; HONG, 2015; ZHANG et al., 2020). These schemes determine vertical profiles of subgrid-scale fluxes related to eddy transport, either diagnosing the vertical turbulent mixing or prognoses it by employing different turbulence closure models, mixing approaches, and PBLH evaluation methods (YANG et al., 2021; WANG et al., 2021). They are often classified based on turbulence closure order and mixing treatment, and linked to specific stability conditions. Local closure PBL schemes are indicated to stable stratification due to their small-eddies local mixing, and nonlocal PBL schemes to unstable stratification due to account large-eddy effects (COHEN et al., 2015). Several studies have shown that PBL scheme choice has significant impacts on NWP, climate modeling, air quality and pollutants dispersion simulations (WANG et al., 2016; JIA; ZHANG, 2020; YANG et al., 2021; LANGE et al., 2021b; SEGURA et al., 2021; SRIVASTAVA; BLOND, 2022; JO et al., 2022).

Different PBL schemes were tested using the Weather Research and Forecasting (WRF) model under several model versions, world regions, meteorological conditions, and methodologies (DZEBRE; ADARAMOLA, 2020; WANG et al., 2020; WANG et al., 2021; GHOLAMI et al., 2021; PENG et al., 2021; LANGE et al., 2021a; LANGE et al., 2021b; SEGURA et al., 2021; ARAVIND et al., 2022). The WRF is a state-of-the-art mesoscale model designed for real-time operational forecasting and atmospheric research (POWERS et al., 2017), which is one of the most employed NWP models. WRF model version 4.0 (SKAMAROCK et al., 2019) owns twelve PBL scheme options ranging from a nonlocal first-order closure scheme to more sophisticated schemes as one-and-a-half-order closure scheme with hybrid mixing treatment. Although many studies investigated the performance of PBL schemes over North America, Europe, and Asia during the last decades (JIA; ZHANG, 2020), few studies evaluate its performance over tropical regions, specifically over the Amazon rainforest.

Amazon rainforest has been a research focus through the last decades due to its recognized global importance. The Amazonian boundary layer was a study subject for many field campaigns across the years (HARRISS et al., 1988; GARSTANG et al., 1990; OLIVEIRA; FITZJARRALD, 1993; FISCH et al., 2009; ANDREAE et al., 2015). Moreover, recent Observations and Modeling of the Green Ocean Amazon (GOAmazon2014/5) campaign (MARTIN et al., 2016) collected an unprecedented data set enabling the investigation of observed PBL and its modeling (KAUFMANN; FISCH, 2016; CARNEIRO et al., 2019; CARNEIRO; FISCH, 2020; CARNEIRO et al., 2021), evaluation of physical parameterizations (ANABOR et al., 2016; WANG et al., 2020; WANG et al., 2021), shallow to deep convection (HENKES et al., 2021), land cover data and topography

(RAFEE et al., 2015; CHAMECKI et al., 2020), precipitation (TAI et al., 2021; BISCARO et al., 2021), clouds regime and life cycle (GIANGRANDE et al., 2020; ZAVERI et al., 2022), atmospheric chemistry and pollution (BELA et al., 2015; RAFEE et al., 2017; MEDEIROS et al., 2017; SHRIVASTAVA et al., 2019; NASCIMENTO et al., 2021; MACHADO et al., 2021), and many others that have allowed the advance in the understanding of the Amazon rainforest atmosphere. Despite these efforts, little attention appears to develop studies dedicated to assessing the performance of PBL schemes in the Amazonian boundary layer modeling.

This research focuses on the role of PBL schemes in the Amazonian boundary layer modeling, with emphasis on its options present in the Advanced Research WRF (ARW) model taking advantage of in situ measurements obtained through the GOAmazon2014/5. The PBL schemes predictability is evaluated in the central Amazon basin for the rainy and dry seasons during the GOAmazon2014/5 Intensive Operating Periods (IOPs). The study aims to assess the forecasting sensitivity of meteorological variables, turbulent fluxes, and PBL structure to different PBL parameterization schemes. Thus, short-term forecasts are performed sharing the same model configuration (except for PBL scheme), and GOAmazon2014/5 data sets are used as benchmark to evaluate its performance. The purpose is to enhance the understanding concerning the predictability of PBL schemes to referred parameters and from intercomparison examine the advantages and disadvantages of different approaches identifying the better setup. This study investigated the potential of PBL schemes for representing the PBL diurnal cycle over the central Amazon basin.

The dissertation is organized as follows. Chapter 2 contains a brief literature review of the subjects investigated here: the theoretical background of subgrid turbulence mixing, the description of evaluated PBL schemes, and an overview of previous studies using PBL schemes over the Amazon basin and other locations. Chapter 3 describes the observational data from GOAmazon2014/5, a brief description of the ARW model, the model configuration and experimental setup, and the statistical metrics employed in the performance analysis of PBL schemes. Results and general discussion are presented in Chapter 4. The conclusions are outlined in Chapter 5.

1.1 Objectives

The main goal of this research is to evaluate the predictability of the PBL parameterization schemes in forecasting the observed Amazonian PBL, maintaining the same model configurations amongst the forecasts to investigate the PBL scheme impacts on meteorological variables, turbulent fluxes, and PBL depth and structure.

The specific objectives are:

• to describe the advantages and disadvantages of using different PBL schemes and to compare the results with in situ observations collected during rainy and dry seasons from the GOAmazon2014/5 field campaign in both typical (2014) and El Niño-Southern Oscillation (2015) years;

• to assess the performance of the PBL parameterization schemes under convective (daytime PBL) and stable (nighttime PBL) regimes;

• and to determine the best model setup(s) based on both visual and performance analysis.

2 LITERATURE REVIEW

This chapter briefly describes the treatment of subgrid turbulence mixing in NWP models and the PBL schemes evaluated in the present study. The last subsection provides an overview of previous studies that tested PBL schemes.

2.1 Subgrid turbulence mixing

The grid resolution (Δ) employed in NWP and general circulation models is higher than the energy-containing turbulence scales (l_ϵ), which is named the mesoscale limit ($\Delta >> l_\epsilon$). Since all turbulent scales in this limit are unresolved, a parameterization scheme is needed to handle the subgrid turbulence mixing and account for its effects on the grid-resolved motions (ZHANG, 2021). Turbulence modeling in NWP models is fulfilled by applying Reynolds-averaging into the governing equations (STULL, 1988). The general form of an atmospheric budget equation is

$$\frac{DC}{Dt} = S_i \tag{2.1}$$

where C is the general atmospheric variables i.e., mechanical or thermodynamic variables ($C : u, v, \theta, q$), and S_i represents sources and sinks of C (e.g., radiation and other physical processes). The Equation (2.1) is rewritten expanding the total rate of change term ($\frac{DC}{Dt}$) as

$$\frac{\partial C}{\partial t} + U\frac{\partial C}{\partial x} + V\frac{\partial C}{\partial y} + W\frac{\partial C}{\partial z} = S_i \tag{2.2}$$

where $\frac{\partial C}{\partial t}$ represents the local time rate of change for the variable C, the terms $U\frac{\partial C}{\partial x}$, $V\frac{\partial C}{\partial y}$, and $W\frac{\partial C}{\partial z}$ are the three-dimensional advection, and U, V, W are the wind speed components in the three-dimensional space. Then, each variable in the atmospheric motion is decomposed into a mean value $\bar{C}$ representing the atmospheric base state (grid-resolved) and fluctuations c' representing the deviation from the atmospheric base state (unresolved PBL subgrid-scales). After the Reynolds-averaging decomposition into the Equation (2.2) and some algebraic manipulations yield a budget equation for the mean variable $\bar{C}$ as

$$\frac{D\bar{C}}{Dt} = \frac{\partial \bar{C}}{\partial t} + \bar{U}\frac{\partial \bar{C}}{\partial x} + \bar{V}\frac{\partial \bar{C}}{\partial y} + \bar{W}\frac{\partial \bar{C}}{\partial z} \equiv \bar{S}_i - \frac{\partial \overline{u'c'}}{\partial x} - \frac{\partial \overline{v'c'}}{\partial y} - \frac{\partial \overline{w'c'}}{\partial z}. \tag{2.3}$$

The nonlinear nature of the advection terms produces the fluctuation terms in Equation (2.3) after the Reynolds-averaging procedure, such as $\overline{w'c'}$, which are covariance terms related to subgrid-scale turbulent fluxes. These covariance terms appear as a form of divergence produced through three-dimensional spatial motions and there is no linear solution for them, leading to the turbulence closure problem which turbulence equations will always contain more unknowns than known terms and must be parameterized (HOLTSLAG; STEENEVELD, 2021; COHEN et al., 2015). Dzebre and Adaramola (2020) summarizes the turbulence closure problem by explaining the issue and introducing the approaches applied in NWP models. Further details on the full set of governing equations and the closure problem can be found in many textbooks (STULL, 1988; POPE, 2000; STENSRUD, 2009; OLAFSSON; BAO, 2020).

NWP models with the mesoscale limit assume the PBL as horizontally homogeneous and the subgrid turbulence mixing is treated separately as vertical and horizontal mixing. The one-dimensional PBL parameterization schemes are responsible for vertical subgrid-scale mixing, meanwhile, the horizontal mixing is treated with a two-dimensional eddy-diffusivity formulation based on the horizontal resolvable-scale velocity deformation (DEARDORFF, 1972), as in the ARW model. The sources of uncertainties regard to subgrid mixing parameterization in NWP models are the nonlocal flux, turbulent mixing length, and horizontal mixing parameterization (ZHANG, 2021).

2.2 PBL parameterization schemes

The PBL schemes are one-dimensional parameterization schemes developed to handle the vertical subgrid-scale fluxes in the atmospheric column by determining the flux profiles within the convective boundary layer (CBL) and stable boundary layer (SBL), which provides atmospheric tendencies for temperature, moisture, clouds, and horizontal momentum (SKAMAROCK et al., 2019). The vertical subgrid-scale fluxes are parameterized through vertical diffusion equations (SHIN; HONG, 2011). Assuming horizontal homogeneous conditions, a small mean vertical wind, and neglecting other sources and sinks, the Equation (2.3) takes the form given as follows

$$\frac{\partial \bar{C}}{\partial t} = -\frac{\partial}{\partial z}\overline{w'c'}, \tag{2.4}$$

which indicates that the local time rate of change for the mean variable $\bar{C}$ at a certain height is the divergence of vertical turbulent flux (as heat/moisture or mo-

mentum) (HOLTSLAG; STEENEVELD, 2021). The ARW PBL schemes distribute vertically the surface fluxes generated due to boundary layer eddies and allow PBL growth by entrainment calculating the vertical turbulent diffusion within and above the PBL (HACKEROTT, 2018). The most widely used PBL parameterizations in atmospheric models are divided into two classes: the first-order K-theory closure with nonlocal mixing and one-and-a-half-order closure (hereafter 1.5-order) based on prognostic turbulence kinetic energy (TKE) equation with local mixing or hybrid eddy-diffusivity mass-flux (EDMF) approach (ZHANG et al., 2020). Table 2.1 summarizes main characteristics of evaluated PBL schemes in the present study.

Table 2.1 - Details of tested PBL schemes, such as turbulence closure order, mixing approach, method of PBLH definition and the threshold value.

PBL scheme	**Closure order**	**Mixing approach**	**PBLH definition**	**Threshold value**
YSU	1^{st}-order	Nonlocal	Buoyancy profile	0.0 (CBL) / 0.25 (SBL)
MRF	1^{st}-order	Nonlocal	*Rib*	0.5
ACM2	1^{st}-order	Hybrid	*Rib*	0.25
SH	1^{st}-order	Scale-aware	*Rib*	0.0 (CBL) / 0.25 (SBL)
QNSE	1.5-order	Hybrid	TKE	0.005 $m^2.s^{-2}$
UW	1.5-order	Local	*Rib*	0.0 (CBL) / 0.19 (SBL)
BouLac	1.5-order	Local	TKE	0.005 $m^2.s^{-2}$
GBM	1.5-order	Local	Explicit	-
MYJ	1.5-order	Local	TKE	0.1 $m^2.s^{-2}$
MYNN2.5	1.5-order	Local	TKE	0.0001 $m^2.s^{-2}$
MYNN3	2^{nd}-order	Local	TKE	0.0001 $m^2.s^{-2}$

SOURCE: Author production.

In nonlocal first-order closure PBL schemes, the vertical mixing coefficients (K_m, K_h) are diagnosed from local Richardson number (Ri) or a diagnostic mixing length (l) or even both approaches, and employ specific mixing lengths for mass and momentum. The local mixing is treated with the K-theory (LOUIS, 1979) and the nonlocal mixing is made with a countergradient term (HONG; PAN, 1996), or transilient matrices (PLEIM, 2007a), or a dependency function of grid size (SHIN; HONG, 2015). The PBLH is assumed as the lowest level where bulk Richardson number (Ri_b) reaches a predefined value or from a buoyancy profile (TROEN; MAHRT, 1986). The PBL schemes in the ARW model that falls in this category are the Medium Range Forecast Model (MRF) (HONG; PAN, 1996), Yonsei University (YSU) (HONG et al., 2006), As-

symetrical Convective Model version 2 (ACM2) (PLEIM, 2007a; PLEIM, 2007b), and Shin-Hong (SH) (SHIN; HONG, 2015). The 1.5-order closure PBL schemes compute the vertical mixing coefficients from a prognostic TKE equation and specific mixing lengths (MELLOR; YAMADA, 1974; MELLOR; YAMADA, 1982). The mixing treatment is either full local (K-theory) or makes use of the EDMF approach (SIEBESMA et al., 2007) to account for nonlocal mixing. Most of them define the PBLH as the level where TKE profiles exceed a threshold value. The PBL schemes in the ARW model that falls in this category are the Bougeault-Lacarrere (BouLac) (BOUGEAULT; LACARRERE, 1989), Grenier-Bretherton-McCaa (GBM) (GRENIER; BRETHERTON, 2001), Mellor-Yamada-Janjic (MYJ) (JANJIĆ, 1990; JANJIĆ, 1994), Mellor-Yamada-Nakanishi-Niino levels 2.5 (MYNN2.5) and 3 (MYNN3) (NAKANISHI; NIINO, 2006; NAKANISHI; NIINO, 2009), University of Washington (UW) (BRETHERTON; PARK, 2009), and the Quasi-Normal Scale Elimination with EDMF (QNSE-EDMF, hereafter QNSE) (SUKORIANSKY et al., 2005). Further details of each PBL scheme are described as follows.

2.2.1 Local closure PBL schemes

The local first-order closure (or K-Theory) uses only resolved variables at adjacent grid points to obtain the covariance values. The flux-gradient theory assumes that turbulence mixing occurs locally by turbulent eddies of a small vertical extent, which homogenize the atmospheric properties (STULL, 1988). Hence, the Equation (2.4) is approximated as

$$\frac{\partial \bar{C}}{\partial t} = \frac{\partial}{\partial z}\left[K_c\left(\frac{\partial \bar{C}}{\partial z}\right)\right], \tag{2.5}$$

here K_c is a diffusion (or mixing) coefficient of C (in $\mathrm{m}^2.\mathrm{s}^{-2}$ units). The Equation (2.5) states that the vertical turbulent flux of variable C is parameterized as proportional to local mean gradient (HOLTSLAG; STEENEVELD, 2021). In local first-order closure schemes (LOUIS, 1979), the diffusion coefficients are represented in terms of an empirical mixing length scale (l), absolute wind shear ($S = |\partial U/\partial z|$), and local stability given as

$$K_c = l^2 S f(Rig), \tag{2.6}$$

where Rig is the gradient Richardson number ($Rig = (g/T)(\partial\theta_v/\partial z)(|\partial U/\partial z|)^{-2}$)

related to the local stability at a given level, and l is taken from the surface layer similarity theory usually following Blackadar (1962). The Equation (2.6) in association with the Equation (2.5) states that vertical turbulent flux at certain height is dependent on local gradient of atmospheric variable C and varies with shear and local stability. This diagnostic local mixing formulation is more suitable for conditions with neutral and stable stratification as observed in nocturnal PBL (SBL) due to its downgradient bias, which difficulties the representation of nonlocal transport performed by thermals in the daytime PBL (CBL) under convective stratification conditions (STENSRUD, 2009; HOLTSLAG; STEENEVELD, 2021).

In order to circumvent the mentioned issues, Mellor and Yamada (1974) proposed to specify the diffusion coefficients by using a prognostic equation for mean TKE intensity, $\bar{e} = 0.5\left(\overline{u'^2} + \overline{v'^2} + \overline{w'^2}\right)$. A prognostic equation for TKE is employed to compute corresponding fluxes in each atmospheric column and is commonly given as

$$\frac{D\bar{e}}{Dt} = \left(\overline{w'u'}\frac{\partial \bar{U}}{\partial z} + \overline{w'v'}\frac{\partial \bar{V}}{\partial z}\right) + \frac{g}{\bar{\theta}}\overline{w'\theta'} + \frac{\partial}{\partial z}\left(\overline{w'e'} + \frac{1}{\rho}\overline{w'p'}\right) - \nu\left|\nabla \times \mathrm{u}\right|^2, \qquad (2.7)$$

where ν is the kinematic viscosity, and the right-hand side terms are, respectively, the local wind shear, buoyancy, vertical transport, and TKE dissipation (ϵ). The diffusion coefficients are computed from the prognostic TKE equation as

$$K_c = S_c l\sqrt{\bar{e}} \qquad (2.8)$$

where l is a mixing length and S_c is a constant dependent of C (stability functions). The Equation (2.8) associated with the Equation (2.5) forms the basis of local 1.5-order closure PBL schemes. The TKE creates a uniform diffusion through mixed-layer leading to entrainment and there is no separation between the PBL and free atmosphere (SKAMAROCK et al., 2019). The calculation of mixing length l is either prognostic or diagnostic, and the combination of the prognostic TKE equation and the mixing length is referred an $e-l$ parameterization (ZHANG et al., 2020). The main differences among 1.5-order closure PBL schemes are which terms are retained in the derivation of prognostic equations and the choice of parameter values as discussed by Jahn et al. (2017). The evaluated 1.5-order closure PBL schemes with local mixing in the present study are the BouLac, GBM, MYJ, MYNN2.5, MYNN3, and UW.

The BouLac PBL scheme (BOUGEAULT; LACARRERE, 1989) is a local 1.5-order closure scheme based on TKE prognostic Equation (2.7), which evolved from the turbulence scheme proposed by Therry and Lacarrère (1983). The second-order moments that arises from TKE equation are parameterized accordingly to the Equation (2.5) for momentum and TKE. For potential temperature (θ) in the CBL, a countergradient term is included similar to the Equation (2.17) and elsewhere is treated as the other variables. The vertical diffusion coefficient for momentum (K_m) is related to the prognostic TKE equation as in Equation (2.8), where S_c is C_K and l is l_K (eddy characteristic length scale) in Bougeault and Lacarrere (1989) notation. Meanwhile, the vertical diffusion coefficients for both heat and TKE intensity are given in the same way as $K_h = K_e = Pr^{-1}K_m$, where Pr is the Prandlt number. The TKE dissipation is estimated by the relation

$$\epsilon = C_\epsilon \bar{e}^{3/2}/l_\epsilon \tag{2.9}$$

where C_ϵ is an $\mathcal{O}(1)$ numerical coefficient. The main difference incorporated in the BouLac scheme is the specification method of the length scales ($C_K l_K$, l_ϵ/C_ϵ) which is related to the distance that a parcel can travel upward (l_{up}) or downward (l_{down}) in response to a local amount of TKE. These length scales are defined as

$$\int_z^{z+l_{up}} \beta\left(\theta\left(z\right) - \theta\left(z'\right)\right) dz' = \bar{e}\left(z\right), \tag{2.10}$$

and

$$\int_{z-l_{down}}^{z} \beta\left(\theta\left(z'\right) - \theta\left(z\right)\right) dz' = \bar{e}\left(z\right), \tag{2.11}$$

where $\beta(= g/\Theta)$, Θ is the reference potential temperature, z is the height, $\bar{e}$ is the mean TKE, and $\bar{\theta}$ is the mean potential temperature. Both l_K and l_ϵ are related to some average between l_{up} and l_{down}, which are, respectively, $l_K = \min(l_{up}, l_{down})$ and $l_\epsilon = (l_{up} l_{down})^{1/2}$. The C_K is defined as 0.4 and C_ϵ^{-1} is 1.4. Finally, the PBLH is assumed as the level where TKE equation reaches a sufficient small value.

The GBM PBL scheme (GRENIER; BRETHERTON, 2001) is a local 1.5-order closure scheme particularly designed to a PBL capped by stratocumulus cloud. The effect of cloud-top radiative cooling is included with an explicit entrainment closure at

the PBL top. This scheme includes two additional prognostic thermodynamic variables approximately conserved for moist reversible adiabatic processes, which are the liquid water potential temperature (θ_l) and the total water mixing ratio (q_t). The turbulent fluxes for these variables and momentum are derived from 1.5-order turbulence closure and both vertical mixing coefficients (K_m, K_h) are given from a prognostic TKE equation, as in equations (2.5) and (2.8). The formulation of the TKE equation carefully treats the moist thermodynamic processes and for the stratocumulus-capped boundary layer all longwave radiative flux divergence occurs at cloud top. The transport of TKE is greatly enhanced to obtain realistic profiles in the buoyancy-driven boundary layer by using a modified TKE diffusivity given as

$$K_e = \eta_{T_e} K_m \tag{2.12}$$

where K_m is the geometrically averaged eddy viscosity between adjacent flux levels and η_{T_e} is a tuned nondimensional coefficient fixed to 5. The turbulence master length scale is defined following Blackadar (1962) as

$$l = kz/(1 + kz\lambda), \tag{2.13}$$

where $k(= 0.4)$ is the von Kármán constant and the asymptotic length scale λ is given proportional to PBL depth z_i as $\lambda = \eta_l z_i$, with η_l set to 0.085 (GRENIER; BRETHERTON, 2001). An explicit PBL entrainment parameterization is assumed following the Turner-Deardorff closure (TURNER, 1973). Three implementations of the entrainment interface were tested: (1) the prognostic inversion approach where the PBLH is a prognostic variable, (2) the reconstructed inversion approach where the PBLH is reconstructed from thermodynamic values at the grid points, and (3) the restricted inversion approach where the PBLH is restricted to lie on a flux level. Hence, the PBLH is computed based on the Richardson number.

The MYJ PBL scheme (JANJIĆ, 1990; JANJIĆ, 1994; JANJIC, 2002) is a local 1.5-order closure scheme, which is a nonsingular implementation of the Mellor-Yamada Level 2.5 closure model (MELLOR; YAMADA, 1982) for all ranges of atmospheric turbulent regimes. The TKE equation is solved iteratively and its transport term is not solved along. On the other hand, it is estimated at a later step where the TKE is vertically diffused as its value at a given height is adjusted with respect to the

value at adjacent levels as explained by Maroneze et al. (2021). The turbulent fluxes for momentum, heat, and TKE are parameterized following the Equation (2.5). The vertical mixing coefficients are provided accordingly to the Equation (2.8), where S_c is given differently for momentum and heat and are both written in terms of dimensionless vertical gradients of wind speed and temperature. The turbulence length scale is given following Mellor and Yamada (1974) as

$$l = l_0 kz/kz + l_0, \tag{2.14}$$

where l_0 is the reference length scale. The TKE dissipation term is given as

$$\epsilon = \frac{\bar{e}^3}{B_1 l}, \tag{2.15}$$

where B_1 is a numerical constant. Janjic (2002) imposes an upper limit on the master length scale (l), which is proportional to $\sqrt{2\bar{e}}$ and a function of large-scale buoyancy and shear parameters. For unstable range, this function is defined from the requirement that the TKE production be nonsingular in the case of growing turbulence. For the stable range, the function is derived from the requirement that the ratio of vertical velocity deviation variance and TKE cannot be smaller than that corresponding to the regime of vanishing turbulence. The master length scale within the PBL is estimated using the usual integral formula, and above the PBL it is computed as a fraction of the vertical grid size. Finally, the PBLH is defined as the lowest model level at which TKE approaches its prescribed lower bound.

The MYNN2.5 and MYNN3 PBL schemes (NAKANISHI; NIINO, 2006; NAKANISHI; NIINO, 2009) differs in which terms are retained in the derivation of prognostic equations being, respectively, a 1.5-order (Level 2.5) and a second-order (Level 3) closure PBL schemes. The main difference between them is that the MYNN2.5 scheme predicts TKE as an extra prognostic variable, while the MYNN3 scheme variances of potential temperature, moisture, and their covariances (SKAMAROCK et al., 2019). The prognostic TKE equation in MYNN2.5 scheme includes stability functions for heat and momentum, which are accompanied by many numerical constants. The TKE dissipation equation is similar to the Equation (2.15), however, the TKE is multiplied by 2. The turbulent fluxes for both momentum and heat are given following the Equation (2.5), and vertical mixing coefficients are given similar to Equation (2.8) using their respective stability functions. The mixing length scale is calculated

as the harmonic average between a turbulent (l_T), a surface layer (l_S), and a buoyant (l_B) length scales as

$$\frac{1}{l} = \frac{1}{l_T} + \frac{1}{l_S} + \frac{1}{l_B}, \tag{2.16}$$

where the l_T is computed within the PBL based on TKE intensity. In the MYNN3 scheme, both potential temperature and moisture variances are added. The turbulent fluxes for momentum are given following the Equation (2.5), meanwhile, kinematic fluxes for virtual potential temperature, liquid water potential temperature, and total water content are specifically parameterized and involve the inclusion of a countergradient contribution. The vertical mixing coefficients for both momentum and heat are given similar to Equation (2.8), although using a modified stability function for momentum that is split into two parts with the first from the level 2.5 formulation and the second is a correction. The PBLH is computed as the level where TKE reaches a threshold value in both MYNN schemes.

The UW PBL scheme (BRETHERTON; PARK, 2009) is an evolution from the GBM scheme, where TKE is diagnosed instead of being prognostic based on TKE production-transport-dissipation balance (TKE storage is neglected). The TKE transport is parameterized using a relaxation of the local TKE to the convective layer mean rather than through vertical TKE diffusion. The explicit entrainment closure is considered to diagnose an effective entrainment diffusivity at the edge of convective layers. All turbulence is calculated using the downgradient diffusion following the Equation (2.5) and the vertical mixing coefficients are given as in the Equation (2.8) using appropriate stability functions. The turbulent master length scale (l) is given as in Equation (2.14), although using a reference length scale (l_0) equal to 30 m for SBL. The UW scheme make computations over a number of layers determined by diagnosing the stability of the thermodynamic profile based on the moist gradient Richardson number. The convective layer is identified as negative Ri (< 0) interfaces. A set of interfaces within $0 < Ri < Ri_c = 0.19$ is diagnosed as stably stratified turbulent layers and the 1.5-order turbulence closure is reduced to a first-order turbulence closure, i.e. vertical mixing coefficients are given as similar to Equation (2.6). The PBLH is defined as the inversion height between model levels using a Rib threshold.

2.2.2 Nonlocal and hybrid closure PBL schemes

Nonlocal mixing approach permits the use of multiple vertical levels to determine variables at a given grid point (COHEN et al., 2015). Several studies (TROEN; MAHRT, 1986; HOLTSLAG; MOENG, 1991; HOLTSLAG; BOVILLE, 1993; NOH et al., 2003) suggested a nonlocal parameterization that considers the countergradient vertical mixing due to larger eddies. In this approach, the Equation (2.4) takes the form as

$$\frac{\partial \bar{C}}{\partial t} = \frac{\partial}{\partial z}\left[K_c\left(\frac{\partial \bar{C}}{\partial z}\right) - \gamma_c\right], \tag{2.17}$$

where γ_c is a correction term applied to local mixing diffusion formulation that accounts for the large-scale eddy effects. The evaluated first-order closure PBL schemes with nonlocal mixing in the present study are the MRF, YSU, ACM2, and SH schemes. Those PBL schemes are correlated and practically evolved from each other.

The MRF PBL scheme (HONG; PAN, 1996) is a nonlocal first-order closure scheme which includes the nonlocal formulation, the Equation (2.17), for both θ and q within the mixed layer. The turbulence diffusion in the free atmosphere is treated with a local diffusion approach accordingly to Equation (2.5), where the vertical mixing coefficients are given following the Equation (2.6) with specific stability functions $f(Rig)$ for the stable and unstable regimes. The mixing length scale is given similar to the Equation (2.13), with λ_0 equal to 30 m. The vertical mixing coefficient for momentum within the PBL is formulated using a parabolic K-profile as

$$K_m = \kappa z w_s \left(1 - \frac{z}{h}\right)^p, \tag{2.18}$$

where $w_s\,(= u_* \phi_m^{-1})$ is the mixed-layer velocity scale, and the exponent $p(= 2)$ is a profile shape parameter. The ϕ_m term related to w_s is a wind profile function evaluated at the top of the surface layer. The countergradient terms for θ and q are given as

$$\gamma_c = b\frac{\overline{w'c'}}{w_s}, \tag{2.19}$$

where $\overline{w'c'}$ is the corresponding surface flux for both θ and q, and b is a coefficient of

proportionality. Profile functions similar to those in surface layer physics are used to ensure the compatibility between the surface layer top and the bottom of the PBL for momentum and mass variables, which are dependent of PBLH and different under unstable and stable regimes. From those profiles, the b factor is set to 7.8. The PBLH (h in the original paper notation) closes the system as given by

$$h = Rib_{cr} \frac{\theta_{va} \left|U(h)\right|^2}{g(\theta_v(h) - \theta_s)} \tag{2.20}$$

where Rib_{cr} is the critical bulk Richardson number, $U(h)$ is the horizontal wind speed at h, θ_{va} is the virtual potential temperature at lowest model level above the ground, $\theta_v(h)$ is the virtual potential temperature at h, and θ_s is the near-surface temperature defined as

$$\theta_s = \theta_{va} + \theta_T \left[= b \frac{\overline{(w'\theta_v{}')}_0}{w_s h} \right], \tag{2.21}$$

where θ_T is the scaled virtual temperature excess near-surface with a maximum limit of 3 K. The vertical mixing coefficients for heat and moisture are computed from the Equation (2.18) using a relationship of the Prandlt number (not reproduced here) related to profile functions and PBLH. The PBLH is obtained iteratively: firstly, h is estimated from the Equation (2.20) without consider the thermal excess, θ_T. This obtained h is used to compute the profile functions and the mixed-layer velocity, w_s. The PBLH is enhanced using both θ_T and w_s. The enhanced h is determined by checking the bulk stability between the lowest model level and levels above. The bulk Richardson number (Rib) between the surface layer and a level z is defined by

$$Rib\,(z) = \frac{g\left[\theta_v(z - \theta_s)\right] z}{\theta_{va} U(z)^2}, \tag{2.22}$$

where Rib_{cr} is set to 0.5. The computed Rib at level z is compared to Rib_{cr} and the value of h corresponding to Rib_{cr} is obtained by linear interpolation between two adjacent model levels as explained by Hong et al. (2006). Thus, both enhanced h and w_s are used to obtain the vertical mixing coefficient for momentum from the Equation (2.18) and mass variables using vertical mixing coefficient obtained using the Prandlt relationship. Finally, the countergradient terms are obtained accordingly to the Equation (2.19).

The YSU PBL scheme (HONG et al., 2006) evolved from the MRF scheme, which adds explicit entrainment to the MRF scheme formulation by using an asymptotic term proportional to the surface flux based on studies with large eddy simulation (LES) models. In the YSU scheme, the Equation (2.17) is rewritten as

$$\frac{\partial \bar{C}}{\partial t} = \frac{\partial}{\partial z}\left[K_c\left(\frac{\partial \bar{C}}{\partial z} - \gamma_c\right) - \overline{w'c'}_h\left(\frac{z}{h}\right)^3\right], \tag{2.23}$$

where $\overline{w'c'}_h$ is the turbulent flux at the inversion layer. This formula maintains the basic concept from the MRF scheme, but includes the entrainment flux at the inversion layer through the asymptotic term $-\overline{w'c'}_h(z/h)^3$ and considers the nonlocal formulation not only for mass variables, but also for momentum. The PBLH is defined as the level in which minimum flux exists at the inversion layer in contrast to the MRF scheme that defines the PBLH as the level where the boundary layer mixing diminishes. The Rib_{cr} is set to 0.0 for unstable and 0.25 for stable regime. All the rest of the formulation (as vertical mixing coefficients, countergradient term, PBLH definition) follows the MRF scheme as aforementioned. The main difference in comparison with the MRF scheme is the explicit entrainment, meanwhile, the entrainment is implicitly parameterized in the former. The free atmosphere diffusion is parameterized accordingly to the MRF scheme, with turbulent mixing length and stability formula based on observations.

The Shin-Hong PBL scheme (SHIN; HONG, 2015) is a scale-aware first-order closure scheme which follows the YSU scheme vertical mixing in both the SBL and free atmosphere. A "scale-aware" mixing approach is applied to CBL, where as the size of the numerical grid Δ is less than the PBL depth the nonlocal term is reduced in strength to allow that resolved variables make a fraction of transport consistent with the grid resolution. This is accomplished by computing separately the nonlocal transport related to strong updrafts and local transport due to small-scale eddies. Subsequently, the subgrid-scale nonlocal transport is multiplied by a grid-size dependency function with the total nonlocal transport profile from LES benchmark data. The subgrid-scale nonlocal heat transport is parameterized as follows

$$\overline{w'\theta'}^{S(\Delta_*)NL} = \overline{w'\theta'}^{NL} P_{NL}(\Delta_{*CS}), \tag{2.24}$$

$$P_{NL}(\Delta_{*CS}) = 0.243\frac{(\Delta_{*CS})^2 + 0.936(\Delta_{*CS})^{7/8} - 1.110}{(\Delta_{*CS})^2 + 0.312(\Delta_{*CS})^2 + 0.329} + 0.757, \tag{2.25}$$

$$C_{cs} = a_{cs}\left[\tanh\left(b_{cs}\left|u_*/w_* + c_{cs}\right| + d_{cs}\right) + e_{cs}\right], \tag{2.26}$$

where superscripts S and NL denote, respectively, subgrid-scale and nonlocal. The Equation (2.25) is a dependency function of nonlocal subgrid-scale heat transport on the grid size, and the empirical function in Equation (2.26) fit with LES data to a free convection case. Both Δ_* and C_{cs} are stability functions. Nonlocal transport profile has three physical parts (not reproduced here) to treating: the surface layer cooling, the mixed-layer heating, and entrainment each part being expressed through a linear function of $z_*(\equiv z/z_i)$, where z_i is the PBLH (in the original paper notation) being computed as in the YSU scheme. The subgrid-scale local transport is parameterized using an explicit grid-size-dependent function $P_L(\Delta_*)$ to compute the vertical diffusivity K_H in such a way to suppress the parameterized transport as grid sizes decreases as follows

$$\overline{w'\theta'}^{S(\Delta_*)L} = -K_{H,PBL}P_L(\Delta_*)\frac{\partial\bar{\theta}^{\Delta}}{\partial z}, \tag{2.27}$$

$$P_L(\Delta_*) = 0.280\frac{(\Delta_*)^2 + 0.870(\Delta_*)^{1/2} - 0.913}{(\Delta_*)^2 + 0.153(\Delta_*)^{1/2} + 0.278} + 0.720, \tag{2.28}$$

where the superscript L and subscript H denotes, respectively, local and heat. The vertical diffusivity $K_{H,PBL}$ is given following the Equation (2.18). This formulation gives the scale-aware nomination and allows handling the CBL at the grey zone resolution (200 m $\leq \Delta \leq$ 10 km).

The ACM2 PBL scheme (PLEIM, 2007a; PLEIM, 2007b) is a first-order closure scheme with hybrid mixing approach. A transilient matrix defines the mass flux between any pair of model layers, adjacent or not, in order to treat the nonlocal transport under convective conditions as given by

$$\frac{\partial\bar{C}_i}{\partial t} = \sum_j M_{ij}\bar{C}_{ij}, \tag{2.29}$$

where M_{ij} is the transilient matrix containing the mixing coefficients between layers i and j. The ACM2 scheme evolved from the ACM1 PBL scheme (PLEIM; CHANG, 1992), which Pleim (2007a) adds an eddy diffusion component to the nonlocal trans-

port to better represent the shape of the vertical profiles. Both local and nonlocal mass fluxes (upward and downward) within subgrid thermals driven by surface heating are explicitly defined and applicable not only for temperature, but for any atmospheric quantity. The ACM2 governing equation in discrete form for any scalar $\bar{C}_i$ in a model layer i combining local and nonlocal mixing is given by

$$\begin{aligned}\frac{\partial \bar{C}_i}{\partial t} &= \mathrm{M2u}\bar{C}_1 - \mathrm{M2d}_i\bar{C}_i + \mathrm{M2d}_{i+1}\bar{C_{i+1}}\frac{\Delta z_{i+1}}{\Delta z_i} \\ &+ \frac{1}{\Delta z_i}\left[\frac{K_{i+1/2}(\bar{C}_{i+1} - \bar{C}_i)}{\Delta z_{i+1/2}} + \frac{K_{i-1/2}(\bar{C}_i - \bar{C}_{i-1})}{\Delta z_{i-1/2}}\right].\end{aligned} \tag{2.30}$$

The total mixing is split between local and nonlocal components by a weighting factor f_{conv} such that

$$\mathrm{M2u} = \frac{f_{conv}K_h(z_{1+1/2})}{\Delta z_{1+1/2}(h - z_{1+1/2})} = f_{conv}\mathrm{Mu}, \tag{2.31}$$

and

$$K(z) = K_z(z)(1 - f_{conv}), \tag{2.32}$$

where the vertical eddy diffusivity (K_z) is defined by boundary layer scaling following Holtslag and Boville (1993) as

$$K_z = \kappa\frac{u_*}{\phi\left(\frac{z_s}{L}\right)}z(1 - z/h)^2, \tag{2.33}$$

here u_* is the friction velocity, h is the PBLH, L is the Monin-Obukov length scale, and ϕ are nondimensional profile functions given specifically for momentum and mass variables following Dyer (1974). For unstable conditions $z_s = \min(z, 0.1h)$, and for stable conditions $z_s = z$. In the Equation (2.30), M2u is the nonlocal convective mixing rate at the top of the lowest model level, M2d_i is the nonlocal downward mixing rate from the i level to $i-1$, Δz_i is the layer thickness, and f_{conv} is a stability function that controls the local versus nonlocal behavior. If $f_{conv} = 1$ the scheme reverts to nonlocal ACM1 scheme or if $f_{conv} = 0$ (stable and neutral conditions) the scheme reverts to local eddy diffusion. The stability function f_{conv} can be derived from the ratio of the nonlocal flux term to the total flux term that involves the

countergradient term. After some manipulations, then f_{conv} becomes

$$f_{conv} = \left[1 + \frac{\kappa^{-2/3}}{0.1a}\left(-\frac{h}{L}\right)^{-1/3}\right]^{-1}, \tag{2.34}$$

where a is set to 7.2. The f_{conv} should have a maximum value of about 0.5 for strongly convective conditions. The boundary layer scaling form of K_z in Equation (2.33) only applies within the PBL and alternate formulations for K_z are necessary independent from PBL and surface-based parameters. Then, expressions for eddy diffusivity are derived as functions of wind, shear, and local Richardson number as

$$K_z = K_{zo} + \left|\frac{\partial U}{\partial z}\right|\left(\frac{Ri}{Ric}\right)^2 l_s, \tag{2.35}$$

for stable conditions ($Ri > 0$), and

$$K_z = K_{zo} + \left[\left(\frac{\partial U}{\partial z}\right)^2 (1 - 0.25Ri)\right]^{0.5} l_s, \tag{2.36}$$

for unstable conditions, where K_{zo}=(0.05 $\mathrm{m}^2.\mathrm{s}^{-1}$) is the minimum K_z, and Ri_{cr} is the critical Richardson number. The length scale l_s is given as

$$l_s = \left(\frac{\kappa z \lambda}{\kappa z + \lambda}\right)^2, \tag{2.37}$$

where $\lambda = 80$ m. The maximum of two methods of calculation of K_z, both equations (2.33) and (2.35), is applied during unstable conditions within the PBL (PLEIM, 2007b). The PBLH (h in the original paper notation) is diagnosed as the height above the level of neutral buoyancy where Rib computed for the entrainment layer exceeds the Rib_{cr}. For stable conditions the method for diagnosis of PBLH is the same as in MRF and YSU schemes, as given by the Equation (2.20). For the unstable conditions is slightly different, where first the top of CBL (z_{mix}) is found as the height at which $\theta_v(z_{mix}) = \theta_s$. The θ_s is given similar to the Equation (2.21), although with $b = 8.5$. The bulk Richardson number is then defined for the entrainment layer above z_{mix} such that

$$Rib = \frac{g\left[\theta(h) - \theta_s)\right](h - z_{mix})}{\bar{\theta_v}\left[U(h) - U(z_{mix})\right]^2}. \tag{2.38}$$

Finally, the PBL top (i.e., PBLH) is defined as the height h where Rib, computed according to Equation (2.38), is equal to Ri_{cr} set to 0.25 for unstable and stable conditions (PLEIM, 2007a).

The QNSE-EDMF (SUKORIANSKY et al., 2005; PERGAUD et al., 2009) is a 1.5-order closure scheme with hybrid mixing approach that includes an EDMF term in his formulation. The mass-flux approaches were introduced in the cumulus convection context due to the narrow cloudy updraft's dominance over vertical transport evidenced through observational studies (SOARES et al., 2004). The EDMF approach combines local closure with a nonlocal mass-flux scheme, where the turbulent flux of a conservative variable C is written as

$$\frac{\partial \bar{C}}{\partial t} = \frac{\partial}{\partial z}\left[K_c\left(\frac{\partial \bar{C}}{\partial z}\right) - M\left(C_u - \bar{C}\right)\right], \tag{2.39}$$

where $M(= \rho a_u w_u)$ is the convective mass-flux, with a_u being updraft area fraction, w_u the vertical velocity of updraft, ρ is the air density, the C_u represents prognostic variables in plumes, and $\bar{C}$ represents prognostic variables for environment. The local mixing term, the first term in right-hand side in Equation (2.39), is treated using stability functions which are fraction-polynomial fits based on the results from the analytical QNSE theory (TASTULA et al., 2016). The original QNSE scheme (SUKORIANSKY et al., 2005) is an $e - \epsilon$ parameterization, where both TKE (e) and dissipation rate (ϵ) are obtained from additional prognostic equations and involves vertical mixing coefficients for them (K_e, K_ϵ), in contrast to $e - l$ parameterization schemes described in Section 2.2.1. The vertical mixing coefficients for both momentum (K_M) and mass (K_H) variables are defined as function of vertical eddy viscosity (ν_z) and diffusivity (κ_z) coefficients predicted by the spectral model as given, respectively, by

$$K_M = \alpha_M C_\mu \frac{K^2}{\epsilon}, K_H = \alpha_H C_\mu \frac{K^2}{\epsilon}, \tag{2.40}$$

where

$$\alpha_M = \frac{\nu_z}{\nu_n}, \alpha_H = \frac{\kappa_z}{\nu_n}, \tag{2.41}$$

are the nondimensional stability functions and $C_\mu \simeq 0.09$. The QNSE-EDMF scheme follows the updraught scheme from Pergaud et al. (2009) and both definitions of entrainment and detrainment are critical in the EDMF approach (see equations (13) and (14) on the reference). In the ARW model, the scheme consists of two subroutines: the first includes the local mixing and the second handles the EDMF approach. Both subroutines compute the atmospheric tendencies, which the mass-flux part is called first in the PBL driver and obtained tendencies from QNSE are added after the call. The local and nonlocal components are independent and only interact through the mean profiles (TASTULA et al., 2016). The PBLH is computed as the level where prognostic TKE reaches a sufficiently small value.

2.3 Previous findings using PBL schemes

Rafee et al. (2015) evaluated the impact of two ARW land cover classifications over the Manaus region for the 2014 dry season, where the YSU scheme was adopted. They obtained results for air temperature from both land classifications to surrounding Manaus areas that showed similar statistical parameters, and the main differences were obtained over the urban area. Bela et al. (2015) investigated Ozone production and transport over the Amazon basin during season transitions through WRF-Chem (WRF model coupled with chemistry) where the MYNN2.5 scheme was employed. Their results represent the lower PBLH pattern in the wet-to-dry than dry-to-wet transitions, and similar PBLH at forest and pasture sites. For the wet-to-dry season transition, the PBLH is underestimated. Anabor et al. (2016) evaluated BouLac and YSU schemes over the central Amazon basin in June 2014 using the ARW model. Results showed that both PBL schemes can depict general features of organized convective storms, although only the BouLac scheme reproduced the diurnal convective cycle and maintained convective activity lasting longer during the nighttime period.

Rafee et al. (2017) investigated urban pollution from different anthropogenic sources in Manaus region using the WRF-Chem model with YSU scheme. Simulated results (near-surface variables and pollutants) compared to the observed data over the forest and pasture sites showed an overall good agreement, therefore the model has proven difficulties in simulating the maximum temperature in the downtown Manaus. Medeiros et al. (2017) evaluated power plant fuel switching and air quality over

the Manaus region using the WRF-Chem with YSU scheme. The analysis showed that day-to-day differences arose largely because of cloudiness variability and other meteorological components of the simulation. Nascimento et al. (2021) investigated aerosol interactions over the central Amazon basin using the WRF-Chem model with the YSU scheme. The simulation has difficulty to represent the observed maximum temperature and underestimates the observed precipitation. Simulations underestimated the daytime PBLH estimated from ceilometer measurements and overestimated from lidar measured values, although the PBL growth rate was relatively well depicted during the morning. The PBLH was well depicted in some hours at night. Sátyro et al. (2021) studied the joint effect of rivers and urban areas on a squall line in the central Amazon using the ARW model. The MYJ scheme was adopted, where microphysics schemes were the evaluation focus. The obtained results indicated that semi-flatbed topography impacts the arrival of squall line and leads, for instance, to low sensible heat flux and consequently a low PBL vertical development.

Recently, Wang et al. (2020) investigated land-atmosphere coupling over the Amazon rainforest for March 2014 using the ARW model with a 50-km horizontal resolution, where the YSU scheme and the Revised MM5 SL scheme were employed. Twenty tunable parameters from both PBL and SL schemes were tested, where the most sensitive are von Kármán constant and profile shape exponent (both in Equation (2.18)). The predicted air temperature, vapor mixing ratio, and net radiation diurnal cycles captured the observations. The turbulent heat fluxes are overestimated during the daytime. The PBLH from both T3 and ZF2 GOAmazon2014/5 sites exhibited much lower values than the observed ones, mainly at night. Wang et al. (2021) quantified physical parameterization uncertainties from ARW model associated with land-atmosphere coupling over the Amazon region following Wang et al. (2020) setup. Six PBL schemes (ACM2, GBM, UW, MYNN2.5, MYNN3, and YSU) were evaluated. The obtained results showed that air temperature is the best-simulated variable, and both vapor mixing ratio and PBLH are underestimated. Turbulent heat fluxes and net radiation are overestimated. The predicted PBLH is very sensitive to PBL and surface processes, and much higher PBLH is produced using MYNN schemes compared to other PBL schemes. Multi-way ANOVA approach revealed that PBL scheme dominates the variance for PBLH and presented lower impact on rainfall and soil moisture variables. The nocturnal PBLH is underestimated while the diurnal PBLH is much better depicted, which indicates that the PBL scheme choice is particularly important for simulations of nighttime PBL over Amazon. They suggest the YSU scheme as the best choice for near-surface variables, and the UW scheme as the preferable choice for the PBLH prediction.

Several studies evaluated PBL schemes using the ARW model over different world regions to investigate near-surface variables, PBL structures, and meteorological phenomena (JIA; ZHANG, 2020). Hu et al. (2010) evaluated three PBL schemes (ACM2, MYJ, and YSU) over southeast Texas during the summer 2005 within the ARW model. The near-surface temperature is underestimated, while moisture is overestimated with YSU scheme. Both ACM2 and YSU schemes lead to a warm and dry PBL compared with MYJ scheme that presented the largest bias. Shin and Hong (2011) tested five PBL schemes (ACM2, BouLac, MYJ, QNSE, and YSU) for a single day under a clear sky and dry environment from CASES-99 experiment using the ARW model. The PBLH obtained from the five PBL schemes was presented, where they greatly diverge during the diurnal cycle with the QNSE scheme producing the deepest PBL and the BouLac scheme the shallowest PBL. Regarding PBL structures, all PBL schemes simulates a warmer and drier PBL than observed. The study concluded that YSU scheme is favorable under unstable conditions, while no PBL scheme satisfactorily simulates the SBL.

Hariprasad et al. (2014) tested seven PBL schemes (ACM2, BouLac, QNSE, MYJ, MYNN2.5, UW, and YSU) over tropical sites on the southeast coast of India using the ARW model. Near-surface and vertical temperature were better depicted using both YSU and MYNN2.5 schemes. Both ACM2 and YSU schemes exhibited a large dry bias during the nighttime. All PBL schemes well simulated the stable morning profiles, and large differences were found in daytime profiles. Shallow CBL was obtained with UW scheme, while ACM2 and QNSE schemes presented the deepest ones. The MYNN2.5, YSU, and BouLac schemes produced more realistic PBLH results when compared to radiosonde data. They concluded that no PBL scheme perfectly works for all variables and stability conditions. Cohen et al. (2015) reviewed PBL schemes and tested the sensitivity of five schemes (ACM2, MRF, MYJ, QNSE, and YSU) in simulating southeastern United States severe weather environments with the ARW model. The tested nonlocal schemes produce more accurate, less biased, and steeper 0−3-km lapse rates than local schemes. Both local and nonlocal schemes overestimate MLCAPE. They indicated that there is not a single approach to select the best PBL scheme.

Dzebre and Adaramola (2020) evaluated the sensitivity of eleven PBL schemes (ACM2, BouLac, MRF, MYJ, MYNN2.5, MYNN3, GBM, UW, TEMF, QNSE, and YSU) to surface winds modeling over southeastern Ghana within the ARW model. Based on prediction skill scores, the MYNN3 scheme was the best scheme producing the lowest errors. Under high-winds season both the GBM and UW

schemes presented reliable results. Both QNSE and MYJ schemes were considered the worst schemes for wind speed prediction. Gholami et al. (2021) evaluated the sensitivity of 10-m wind speed over Persian Gulf testing seven PBL schemes (ACM2, BouLac, MYJ, MYNN2.5, MYNN3, QNSE, and YSU) with the ARW model. The YSU scheme presented the best wind speed estimation even with the wind direction prediction presenting higher RMSE. Lange et al. (2021b) tested four PBL schemes (ACM2, MYJ, MYNN2.5, and YSU) in the sensitivity of simulated surface-level pollution concentrations over Highveld of South Africa. The obtained results showed that each scheme performed best results for different locations. They also found that different PBL schemes should be used for different pollutants modeling, for instance, nonlocal PBL schemes (e.g., YSU or ACM2) to Ozone and local PBL schemes (e.g., MYJ or MYNN2.5) to particulate matter pollution simulations.

Many studies over the Amazon investigated meteorological phenomena, mostly atmospheric chemistry and pollution, with few studies evaluating parameterization schemes mainly the PBL schemes. Both Wang et al. (2020) and Wang et al. (2021) studies revealed the performance of PBL schemes and their impacts on investigated variables, although with a much lower horizontal resolution ($\Delta = 50$ km) than that used in regional NWP ($\Delta < 10$ km) and only for the 2014 rainy season. Among studies over other world regions, most of them focused on a specific class of variables (e.g., surface variables, turbulent fluxes, PBL structure) to investigate an application or phenomena (e.g., wind energy, pollutants, weather forecast). Another issue is that PBLH measurements are not always available to evaluate the performance of the PBL schemes. Furthermore, the studies that focus purely on development and evaluation of PBL schemes generally preferred to simulate PBL profiles under well-controlled or simplified scenarios to isolate the contribution of PBL processes, avoiding real-world complexity (WANG et al., 2016; MARONEZE et al., 2021).

In this sense, this study intends to contribute to the evaluation of the performance of PBL schemes over the central Amazon basin. The purpose is to understand how different PBL schemes play a role and impact the predictability of meteorological variables, turbulent fluxes, and PBL structure. The knowledge improvement on Amazonian boundary layer modeling and filling the existing gap in evaluating PBL schemes over the central Amazon basin under convection-permitting resolution ($\Delta = 1$ km) is expected. This is achieved through developing forecasts for the rainy and dry seasons within the state-of-the-art ARW model by changing only the PBL scheme option. Then, GOAmazon2014/5 data sets are used to benchmark the forecasts, and the results from different PBL schemes are investigated and evaluated.

3 METHODS

3.1 Observational data

The observations from the GOAmazon2014/5 campaign (MARTIN et al., 2016) are used to benchmark the performance of numerical experiments evaluating eleven PBL schemes (indicated in Table 2.1). Figure 3.1 shows the study area and the research site. Atmospheric data were collected during 24 months at the research site named T3 (3.213° S, 60.598° W, 50 m) located north of Manacapuru city in Amazonas state, Brazil. T3 (Figure 3.1b) was a pasture site surrounded by native forest, which was situated near both the Negro and Solimões Rivers, and approximately 70 km downwind of Manaus city. The collected data sets and further details are available in the ARM GOAmazon2014/5 database (available online in `https://www.arm.gov/research/campaigns/amf2014goamazon`).

Figure 3.1 - Satellite imagery of the central Amazon basin in December 2014 (a), and an aerial view of U.S. Department of Energy (DOE) Atmospheric Radiation Measurement (ARM) Mobile Facility (AMF) (MATHER; VOYLES, 2013) deployed at T3 site in February 2014 (b).

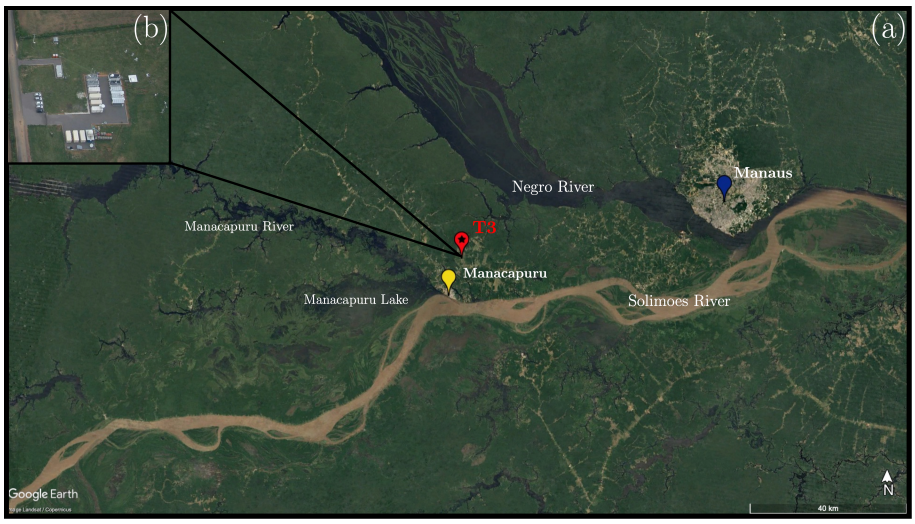

SOURCE: Author production.

Two 45-days IOPs were accomplished to represent the climax of both the 2014 rainy and dry seasons during the GOAmazon2014/5, respectively, from February 15 to March 31 (IOP1), and from September 1 to October 15 (IOP2). The present study considers the same 2014 periods for the 2015 year setting both IOP3 and IOP4,

which are featured by the occurrence of the El Niño–Southern Oscillation (ENSO) event of that year accordingly to Carneiro and Fisch (2020). The meteorological conditions and observational analysis of these IOPs can be found in the literature (CARNEIRO; FISCH, 2020; BISCARO et al., 2021).

The Meteorological Measurements Associated with the Aerosol Observing System (AOSMET) (KYROUAC; SPRINGSTON, 2014) provides the standard meteorological measurements such as 2-m air temperature (T_2), 2-m air relative humidity (RH_2), 10-m horizontal wind speed (U_{10}), and precipitation (PCP) as reference for the intercomparison. Turbulent fluxes such as sensible heat flux (H), latent heat flux (LE), and momentum flux (τ) were collected with the Eddy CORrelation Flux (ECOR) (SULLIVAN et al., 2014). The PBL structures were obtained through radiosonde soundings (KEELER et al., 2014) launched over the T3 site. The vertical profiles for potential temperature (θ), vapor mixing ratio (q), and horizontal wind speed (U) taken at 02:00, 08:00, 11:00, and 14:00 LT are compared with predicted profiles. The PBLH estimated from ceilometer measurements (MORRIS; BRIAN, 2014) are employed to benchmark all the predicted PBLH amongst the eleven PBL schemes. The ceilometer is considered the best instrument to capture the entire PBLH daily cycle over different seasons and provides a good comparison with conventional CBL height estimations (CARNEIRO; FISCH, 2020; ZHANG et al., 2021). The estimated PBLH from ECMWF Reanalysis v5 (ERA5) (HERSBACH et al., 2020) for the T3 site is also compared to predictions from PBL schemes in order to investigate the performance between the experiments and reanalysis data.

3.2 Advanced Research WRF dynamical core

The state-of-the-art Advanced Research WRF (ARW) dynamical core version 4.2.2 is adopted to perform the numerical experiments. The ARW consists of a subset of the WRF modeling system with the ARW dynamics solver (SKAMAROCK et al., 2019). A hybrid sigma-pressure vertical coordinate is applied to describe the governing equations in the ARW solver (PARK et al., 2013), where the prognostic variables are defined in function of the mass vertical coordinate. The non-hydrostatic fully compressible Euler equations are cast in flux form to ensure conservation properties (KLEMP et al., 2007). The governing equations in perturbation form are obtained using perturbation variables from a hydrostatically-balanced reference state and solved along with an equation of state. The third-order Runge-Kutta (RK3) time-split integration scheme is employed to advance the solution in time (WICKER; SKAMAROCK, 2002). The spatial discretization in the ARW solver is accomplished using

an Arakawa C grid staggering. The advection, scalars, and geopotential terms in model equations are discretized in space using a 6^{th} order accurate spatial discretization. Subgrid turbulent mixing is included in the ARW solver using the Smagorinsky first-order closure approach to compute the horizontal eddy viscosity (K_H) as

$$K_H = C_s^2 l^2 \left[0.25\left(D_{11} - D_{22}\right)^2 + \overline{D_{22}^2}^{xy}\right]^{1/2} \tag{3.1}$$

where D_{xy} is the deformation tensor, $l = (\Delta x \Delta y)^{1/2}$ is a length scale, and C_s is a constant value typically defined as 0.25. In addition, a PBL parameterization scheme (Section 2.2 describes the evaluated options) is employed to independently handle the subgrid-scale turbulent vertical mixing computing the vertical eddy viscosity (K_V) (SKAMAROCK et al., 2019). Beyond the PBL scheme option, a set of physical parameterization schemes to represent subgrid-scale processes must be chosen. This set comes down to microphysics, cumulus, radiation, land surface, and surface layer categories. The equations are closed with initial and lateral boundary conditions.

3.2.1 Model configuration and experimental setup

The model domain (Figure 3.2a) is set using a Mercator projection and consists of three one-way interacting nested grids with spacing of 9 km (d01), 3 km (d02), and 1 km (d03), respectively, centered on the location of the T3 site. The parent domain covers a great part of Amazonas and Pará states, with small areas of Roraima, Amapá, and Mato Grosso states, as well as both Colombian and Venezuelan countries. The d03 domain is located over the central Amazon basin. The vertical grid has 50 hybrid sigma-pressure levels (Figure 3.2b), where the first level is around 42 m height. The first 20 levels are placed below the first 2000 m height to ensure vertical grid resolution ($\Delta z \approx 90$ m), and the model top was set at 50 hPa. The time-step was set as six times the horizontal resolution ($\Delta t = 6\Delta$) being, respectively, 54 s (d01), 18 s (d02), and 6 s (d03).

To evaluate the performance of PBL schemes under different conditions the ARW version 4.2.2 simulations were conducted for 72-h to each GOAmazon2014/5 IOP. Table 3.1 summarizes the model integration periods (the complete day is indicated), which are referred accordingly to their respective IOP labels. The first 12-h are discarded (spin-up) from analysis to prevent dynamic instability (JANKOV et al., 2007). As all forecasts begin from 00:00 UTC, the local time (LT) for the domain is UTC - 4-h, and considering the spin-up time, all 60-h analysis periods range from 08:00 LT on the first day until 20:00 LT on the third day. An output temporal resolution

Figure 3.2 - The domain configuration and topography in (a), and vertical grid in (b).

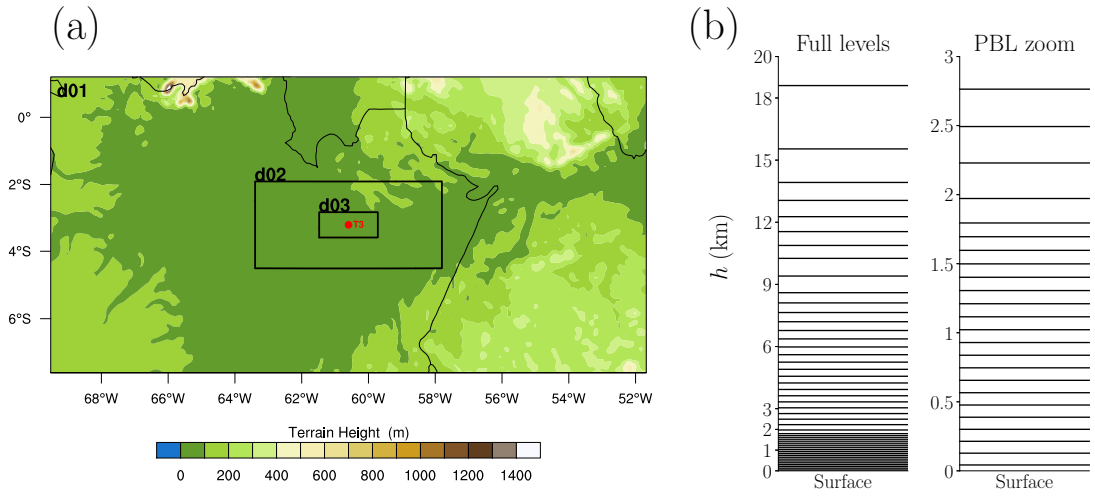

SOURCE: Author production.

Table 3.1 - Model integration periods.

Forecasting periods		
	IOP1	**IOP2**
Day	03 March 2014	01 October 2014
Forecast	UTC+0 02/Mar − UTC+0 05/Mar	UTC+0 30/Sept − UTC+0 03/Oct
	IOP3	**IOP4**
Day	03 March 2015	15 October 2015
Forecast	UTC+0 02/Mar − UTC+0 05/Mar	UTC+0 14/Oct − UTC+0 17/Oct

SOURCE: Author production.

of 1-h was chosen for comparison with the observations. WRF initial and boundary conditions are provided by the Global Forecast System (GFS) forecast data from National Centers for Environmental Prediction (NCEP), which are operational global analysis data available on $0.5° \times 0.5°$ forced every 3-hourly time interval. The GFS forecast data was used rather than the final analysis to investigate the predictability capabilities of the PBL schemes. The Moderate-resolution Imaging Spectroradiometer (MODIS) land use and soil category data is employed for land initialization and boundary conditions (default since ARW version 4.0), where the T3 site is classified as savanna and surrounded by evergreen broadleaf forest.

The physical parameterization schemes used here follow the INPE CPTEC-WRF

operational version options (CPT-WRF v1.1) (FERNANDEZ, 2020). The four-layer Unified Noah land-surface (LS) model (TEWARI et al., 2004) is used for the land surface processes, which depends on both the longwave and shortwave radiance computed by the Rapid Radiative Transfer Model for GCMs (RRTMG) (IACONO et al., 2008). The Eta-Ferrier microphysics scheme (ROGERS et al., 2001) is employed and the New Tiedke cumulus scheme (ZHANG; WANG, 2017) is only used on the parent domain (d01). Revised MM5 (JIMÉNEZ et al., 2012) surface layer (SL) scheme is adopted in order to compute surface fluxes. The YSU PBL scheme (HONG et al., 2006) option completes the control configuration. The MYJ, MYNN3, and QNSE PBL schemes are tied with their specific SL schemes in the ARW solver. It means that as all model runs are configured in the same way; therefore, variances in predicted meteorological and PBL parameters can be attributed to the both chosen PBL and SL schemes. All the rest of the evaluated PBL schemes (i.e., ACM2, BouLac, GBM, MRF, MYNN2.5, SH, UW, and YSU) share the same SL scheme option, so the simulated differences amongst those eight PBL schemes are not caused by the use of different SL calculations.

The ARW solver was compiled in the Santos Dumont supercomputer (SDumont) located at Laboratório Nacional de Computação Científica (LNCC) in Petrópolis, Rio de Janeiro state, Brazil. SDumont supercomputer has an installed processing capacity of 5.1 Petaflops.s^{-1} with an hybrid setup computational nodes (further details are available online in `https://sdumont.lncc.br/machine.php?pg=machine#`). A total of 288[1] hours from the GOAmazon2014/5 IOPs were predicted within the ARW solver taking the advantage of SDumont resources. The model runs are performed in parallel using one computational node (48 processors), with each run taking on average 150 minutes to finish representing a total of approximately 110 hours (wall-clock time) to run all cases. A total of $\approx$ 1.2 Tb of forecasting data were produced using SDumont.

3.3 Data analysis and performance evaluation

The predicted T_2, RH_2, U_{10}, PCP, H, LE, τ, and PBLH are extracted from d03 WRF output files with 1-h resolution on the T3 site location for each PBL scheme prediction through handmade codes written in Python language. The predicted vertical profiles (θ, q, and U) are compared with observations at 02:00 (SBL), 08:00 (SBL erosion), 11:00 (CBL development), and 14:00 LT (CBL) representing the PBL daily

[1]If consider all cases, a total of 3168 hours (= 4 (IOPs) $\times$ 72-h (forecast cycle) $\times$ 11 (evaluated PBL schemes)) were computed.

cycle. The PBLH spatial fields are studied to investigate how PBL schemes impact the PBLH distribution across the central Amazon basin. Unfortunately, no observational data is available for comparison. All experiments are labeled with their respective PBL scheme option. The intercomparison between PBL schemes predictions is made through time-series to assist the visual analysis. The turbulent fluxes in both IOP1 and IOP3 present missing gaps related to measurement failures, hence were not evaluated. The observed momentum flux (τ) is estimated from friction velocity (u_*) as $\tau = \overline{\rho}.u_*^2$, which presented measurement missing gaps and statistical metrics were not computed for this variable. The statistical analysis is carried out by comparison of the observed and simulated data from the PBL schemes in order to evaluate the predictive performance of each scheme. The statistical indexes are mean bias (MB), mean absolute error (MAE), mean absolute percentage error (MAPE), root-mean-squared-error (RMSE), Pearson's correlation coefficient (r), and index of agreement (IOA). Table 3.2 summarizes statistical index formulations. Almost all statistical indexes are computed over the 60-h period, except for the PBLH which diurnal variations are significant and the statistical indexes are separately computed to both daytime (06:00−18:00 LT) and nighttime (19:00−05:00 LT). Taylor diagrams are employed to assist the statistical indexes visualization and Taylor Skill Score is employed to quantify the performance (TAYLOR, 2001).

Table 3.2 - Statistical indexes to evaluate the performance of numerical experiments.

Indexes	**Equations***
Mean bias	$MB = \frac{1}{N}\sum_{k=1}^{N}(\mathrm{f}_k - \mathrm{o}_k) = \bar{\mathrm{f}} - \bar{\mathrm{o}}$
Mean absolute error	$MAE = \frac{1}{N}\sum_{k=1}^{N}\lvert\mathrm{f}_k - \mathrm{o}_k\rvert$
Mean absolute percentage error	$MAPE = \frac{1}{N}\sum_{k=1}^{N}\left\lvert\frac{\mathrm{f}_k - \mathrm{o}_k}{\mathrm{o}_k}\right\rvert \times 100\%$
Root-mean-square-error	$RMSE = \left[\frac{1}{N}\sum_{k=1}^{N}(\mathrm{f}_k - \mathrm{o}_k)^2\right]^{1/2}$
Pearson's correlation coefficient	$r = \frac{\sum_{k=1}^{N}(\mathrm{f}_k - \bar{\mathrm{f}})(\mathrm{o}_k - \bar{\mathrm{o}})}{\left[\sum_{k=1}^{N}(\mathrm{f}_k - \bar{\mathrm{f}})^2\right]^{1/2}\left[\sum_{k=1}^{N}(\mathrm{o}_k - \bar{\mathrm{o}})^2\right]^{1/2}}$
Index of agreement	$IOA = 1 - \frac{\frac{1}{N}\sum_{k=1}^{N}(\mathrm{o}_k - \mathrm{f}_k)^2}{\sum_{k=1}^{N}(\lvert\mathrm{f}_k - \bar{\mathrm{o}}\rvert + \lvert\mathrm{o}_k - \bar{\mathrm{o}}\rvert)^2}$

* f is forecasting, and o is observations.

SOURCE: Author production.

4 RESULTS

4.1 IOP1 (2014 rainy season)

4.1.1 Meteorological variables

Figure 4.1 shows the predicted meteorological variables from all the eleven intercomparison experiments and corresponding observations. All PBL schemes predicted a colder (≈ -2.5°C) and wetter ($\approx +10\%$) atmosphere than observations in the first two days, while the predictions are closer to observations during the third day. The MRF (UW) scheme produced the driest (wettest) conditions across the period. The differences at maximum T_2 (13:00 LT) on March 2 are around 5.0 °C colder. The noticed differences are probably related to the prediction of a non-observed rain during the morning.

Figure 4.1 - Time series of predicted 2-m air temperature (a), 2-m relative humidity (b), 10-m horizontal wind speed (c), and precipitation (d) for IOP1.

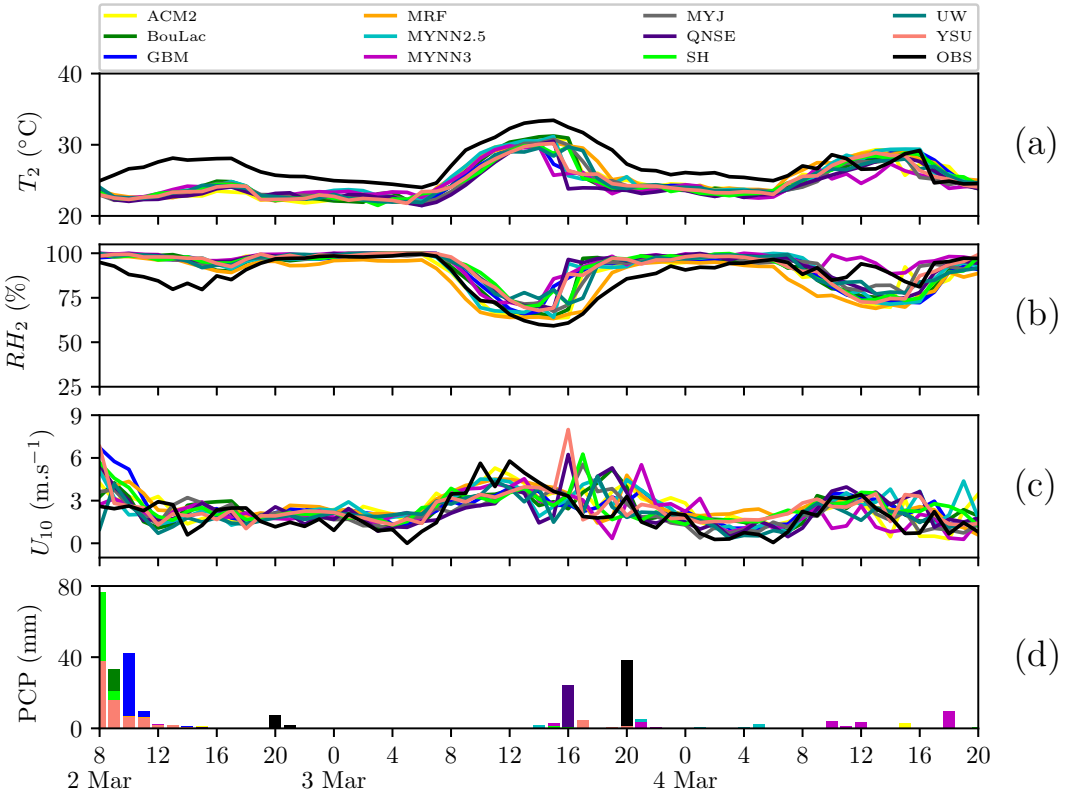

SOURCE: Author production.

For instance, the SH scheme predicted 76 mm of rainfall at 08:00 LT. On the other hand, the observations indicate PCP (= 7 mm) only few hours later (at 20:00 LT). All PBL schemes predicted U_{10} that lies on the observations, although no PBL scheme depicted the abrupt increase in the U_{10} following the convection initiation in the morning on March 3. The MRF scheme showed the highest U_{10} (average of 2.2 m.s^{-1}) during nighttime periods. During the daytime, all PBL schemes reproduced the typical drying pattern, for instance, the MYNN2.5 scheme showed a good agreement during the morning on March 3. No PBL scheme reproduced the observed rainfall amount of 38.5 mm at 20:00 LT on March 3. The QNSE scheme anticipates it by predicting 24 mm at 16:00 LT. At this time, both QNSE (= 6.0 m.s^{-1}) and YSU (= 8.0 m.s^{-1}) schemes produced a U_{10} peak, which were not observed. No rainfall was observed on March 4, although MYNN2.5, MYNN3, YSU, and ACM2 schemes predicted moderate rain (lesser than 10 mm). The MYNN3 scheme is the only PBL scheme that presented both colder (≈ -1.7°C) and wetter ($\approx +4\%$) conditions compared to observations on March 4.

Table 4.1 presents the statistical indexes computed for meteorological variables over the 60-h analysis period. The best indexes are highlighted in bold. The average observed T_2 is 27 °C, and all evaluated PBL schemes underestimated this value. The MRF scheme showed better statistical indexes (MB = -2.0 °C, MAE = 2.3 °C, RMSE = 2.6 °C, IOA = 0.75). The MYJ scheme presented the best correlation coefficient (r = 0.82). The QNSE scheme showed the worst indexes with the highest error (MB = -2.9 °C, MAE = 3.0 °C, RMSE = 3.4 °C), and both the lowest r (= 0.82) and IOA (= 0.63). The average observed RH_2 for the period was 88 %. Only the MRF scheme underestimates (MB = -2 %) the observation and presented the best IOA (= 0.84). The MYJ scheme produced the lower error (MAE = 6 %, RMSE = 8 %). Despite the MYNN3 scheme showing the higher MAE (= 7 %), it performed the best correlation coefficient (r = 0.78). The GBM scheme presented the highest RMSE (= 10 %) with the lowest correlation coefficient (r = 0.58). The average observed U_{10} is 2.0 m.s^{-1}. All PBL schemes overestimated this wind speed for U_{10}. The UW scheme presented almost zero MB (= 0.03 m.s^{-1}) with lowest error (MAE = 0.8 m.s^{-1}, RMSE = 1.1 m.s^{-1}). The MRF scheme had the best correlation coefficient (r = 0.73) and the ACM2 scheme presents the best IOA (= 0.77). Statistical indexes for PCP revealed that both MYJ (MB = -0.3 mm) and UW (MB = -0.05 mm) schemes underestimated the observed PCP. The MRF scheme presented zero MB, although not showing a good temporal agreement with the observed PCP. The UW scheme showed the lowest error (MAE = 1.0 mm, RMSE = 5.1 mm).

Table 4.1 - Statistical indexes for IOP1 meteorological variables computed over the 60-h analysis period.

Variable	**Statistical index**	**PBL scheme**										
		ACM2	BouLac	GBM	MRF	MYNN2.5	MYNN3	MYJ	QNSE	SH	UW	YSU
T_2	AVG	24.9	24.9	24.7	25.2	25.0	24.5	24.7	24.3	24.7	24.7	24.7
	MB	-2.2	-2.2	-2.4	**-2.0**	-2.1	-2.7	-2.5	-2.9	-2.4	-2.4	-2.5
	MAE	2.6	2.5	2.8	**2.3**	2.4	2.7	2.6	3.0	2.7	2.6	2.7
	RMSE	2.9	2.8	3.1	**2.6**	2.8	3.1	2.8	3.4	3.0	2.9	3.0
	r	0.73	0.79	0.68	0.76	0.72	0.76	**0.82**	0.67	0.71	0.78	0.74
	IOA	0.72	**0.75**	0.66	**0.75**	0.73	0.65	0.72	0.63	0.68	0.70	0.68
RH_2	AVG	90	91	91	86	91	95	92	93	92	92	92
	MB	2	3	3	**-2**	3	7	5	5	4	4	4
	MAE	**6**	7	8	7	7	7	**6**	8	8	7	7
	RMSE	9	9	10	9	10	10	**8**	10	10	9	10
	r	0.70	0.67	0.58	0.72	0.64	**0.78**	0.77	0.61	0.60	0.72	0.63
	IOA	0.83	0.81	0.74	**0.84**	0.79	0.75	0.82	0.74	0.75	0.79	0.76
U_{10}	AVG	2.5	2.4	2.5	2.7	2.5	2.2	2.2	2.3	2.5	2.0	2.5
	MB	0.5	0.4	0.5	0.7	0.5	0.2	0.1	0.3	0.5	**0.03**	0.4
	MAE	1.0	0.9	1.0	0.9	1.1	0.9	**0.8**	1.0	1.0	**0.8**	1.0
	RMSE	**1.1**	**1.1**	1.2	**1.1**	1.3	**1.1**	**1.1**	1.3	1.3	**1.1**	1.3
	r	0.66	0.57	0.55	**0.73**	0.52	0.56	0.57	0.45	0.49	0.56	0.49
	IOA	**0.77**	0.70	0.69	0.76	0.69	0.74	0.73	0.66	0.64	0.72	0.67
PCP	AVG	1.2	1.4	1.2	0.8	1.9	1.5	0.5	0.9	1.9	0.3	1.3
	MB	0.4	0.6	0.4	**0.0**	1.1	0.7	-0.3	0.2	1.1	-0.5	0.5
	MAE	2.0	2.2	2.0	1.6	2.7	2.3	1.3	1.7	2.6	**1.0**	2.0
	RMSE	6.8	8.1	7.7	6.0	10.4	7.9	5.3	6.2	11.4	**5.1**	7.3

* AVG is the average.

SOURCE: Author production.

4.1.2 PBL diurnal cycle and structure

Figure 4.2 shows the PBLH time series obtained from all tested PBL schemes, the PBLH from ECMWF Reanalysis v5 (ERA5) (hereafter PBLH_{ERA5}), and observed data estimated from ceilometer measurements (hereafter PBLH_{OBS}). The observed PBL heights evolved from 371 m at 08:00 LT to 1233 m at 13:00 LT on March 2. All PBL schemes and PBLH_{ERA5} underestimated the daytime PBLH_{OBS} by a value of around 640 m. The MYJ scheme presents the deepest PBLH (= 604 m) at the time of maximum PBLH_{OBS}. The higher growth rate was 408 m.h^{-1}, observed between 09:00 and 10:00 LT. The QNSE (GBM) scheme presents the deepest (shallowest) layer on the first day compared to other PBL schemes. For instance, the GBM scheme presented an average PBLH of 95 m. After its maximum, the PBLH_{OBS} decreased until 02:00 LT in the early morning on March 3.

Figure 4.2 - IOP1 planetary boundary layer height.

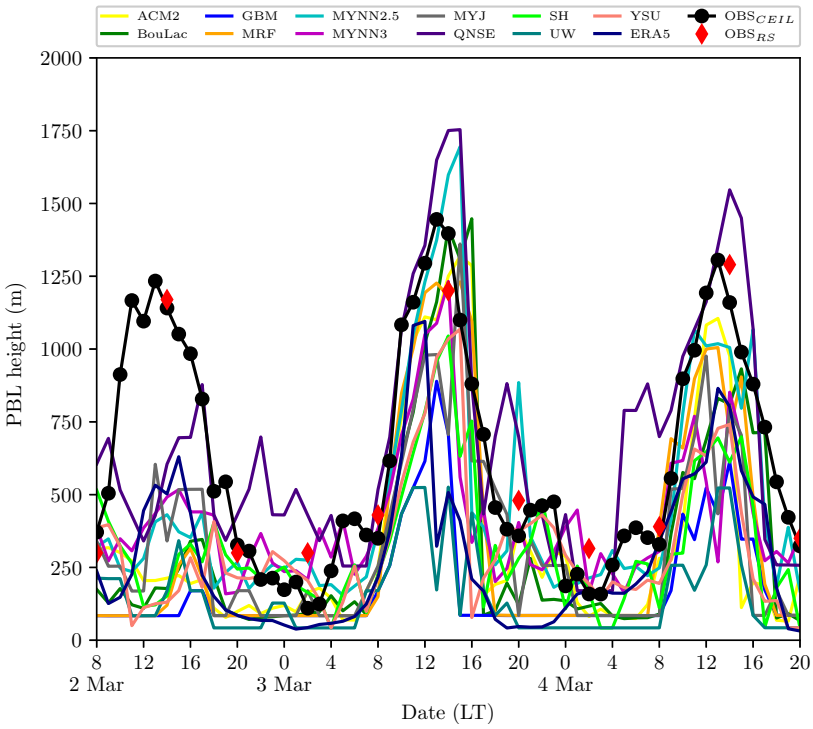

SOURCE: Author production.

Figure 4.3 shows θ, q, and U predicted for all PBL schemes and corresponding radiosonde soundings on March 2. The comparisons with forecasting on March 2 are

at 08:00, 11:00, and 14:00 LT. PBL schemes depicted a colder (-1.4 K) and wetter (+2.5 g.kg^{-1}) boundary layer than the observed based on vertical profiles of θ and q at 08:00 LT. A low-level jet (LLJ) is seen near 390 m height in the observed U profile with values around 11 m.s^{-1}. Predicted U profiles diverge greatly amongst them, with the SH scheme predicting the higher U (= 15 m.s^{-1} near 1200 m height).

Figure 4.3 - Vertical profiles of potential temperature (θ) in (a), vapor mixing ratio (q) in (b), and horizontal wind speed (U) in (c) on March 2, 2014. The time of radiosonde soundings are indicated in y-axis label.

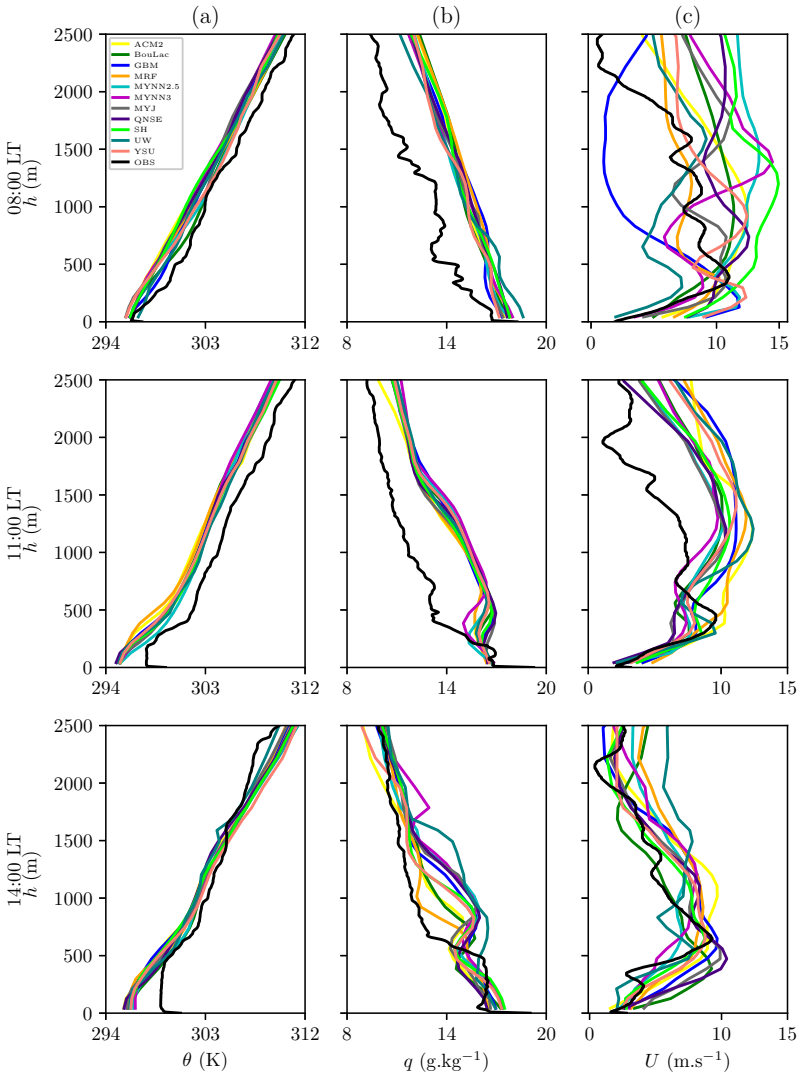

SOURCE: Author production.

After the erosion of nocturnal PBL, the aforementioned differences were maintained

whereas all PBL schemes present colder (-2.0 K) and wetter (+2.4 g.kg^{-1}) conditions than the observation at 11:00 LT. The observed LLJ maintained the same height as at 08:00 LT. The ACM2, UW, and MRF schemes produced higher U ($\approx$ 12 m.s^{-1}) compared to other schemes. The observed θ profile at 14:00 LT is weakly unstable in the lower part and weakly stable in the upper part. All PBL schemes predicted a colder ($\approx$ -0.6 K) and wetter ($\approx$ +1.1 g.kg^{-1}) daytime PBL. Both YSU and ACM2 schemes predicted a drier (around -1.5 g.kg^{-1}) condition above the PBL top. During the CBL stage, most of the PBL schemes overestimated (around +3 m.s^{-1}) the observed U. The UW scheme showed lower U ($\approx$ 2 m.s^{-1}) near-surface and higher ($\approx$ 8 m.s^{-1}) above 1500 m height.

The PBLH$_{OBS}$ presented an average height of 209 m between 00:00 and 06:00 LT on March 3. The QNSE (UW) scheme presented the deepest (shallowest) PBLH during the nighttime. A slight decrease in PBLH$_{OBS}$ is seen during the SBL erosion (between 06:00 and 08:00 LT). Both MRF and SH schemes depicted this decrease presenting a shallow PBL. After the complete SBL erosion, the PBL grows at a high rate (= 468 m.h^{-1}) between 09:00 and 10:00 LT. Only the QNSE scheme was able to follow this fast growth. From 10:00 to 13:00 LT, the PBLH$_{OBS}$ still deepens achieving its maximum height of 1445 m. No PBL scheme depicted this peak in terms of time consistency and depth. The QNSE and MYNN2.5 schemes overestimated (PBLH $>$ 1650 m) the observed peak and also during the transition from late afternoon to nighttime. The UW scheme presented the lowest PBLH (= 172 m) at 13:00 LT. Following the observed maximum depth, the PBLH$_{OBS}$ decreased continuously until 20:00 LT. The PBLH$_{OBS}$ slightly increased until 23:00 LT when a sudden and very intense reduction occurred from 475 m to 186 m at the midnight. The SH scheme anticipates this observed sudden drop. The PBLH$_{ERA5}$ underestimated the observations across the period, presenting a shallower layer (around -200 m) in both the early morning and nighttime.

Figure 4.4 shows θ, q, and U profiles and corresponding soundings at 02:00, 11:00, and 14:00 LT on March 3. A better agreement is seen amongst predicted and observed profiles when compared to the first day of simulation. During the SBL stage at 02:00 LT, most PBL schemes produced colder (-1.5 K) and wetter (+0.5 g.kg^{-1}) conditions near-surface, with nonlocal schemes (e.g., MRF, ACM2, YSU) showing the driest ones. The YSU scheme showed a good agreement with the observed θ profile until $\approx$ 1500 m where all PBL schemes presented warmer (+1.2 K) and drier (-0.5 g.kg^{-1}) conditions. PBL schemes are unable to reproduce the observed U profile shape that presents an LLJ (= 8.9 m.s^{-1}) near 300 m height, although the

MYNN2.5 scheme predicted the observed LLJ with good agreement. In the CBL development stage at 11:00 LT, most of the PBL schemes presented a colder (-1.3 K) and wetter (+1.1 g.kg^{-1}) bias.

Figure 4.4 - Vertical profiles of potential temperature (θ) in (a), vapor mixing ratio (q) in (b), and horizontal wind speed (U) in (c) on March 3, 2014. The radiosonde soundings time are indicated in y-axis label.

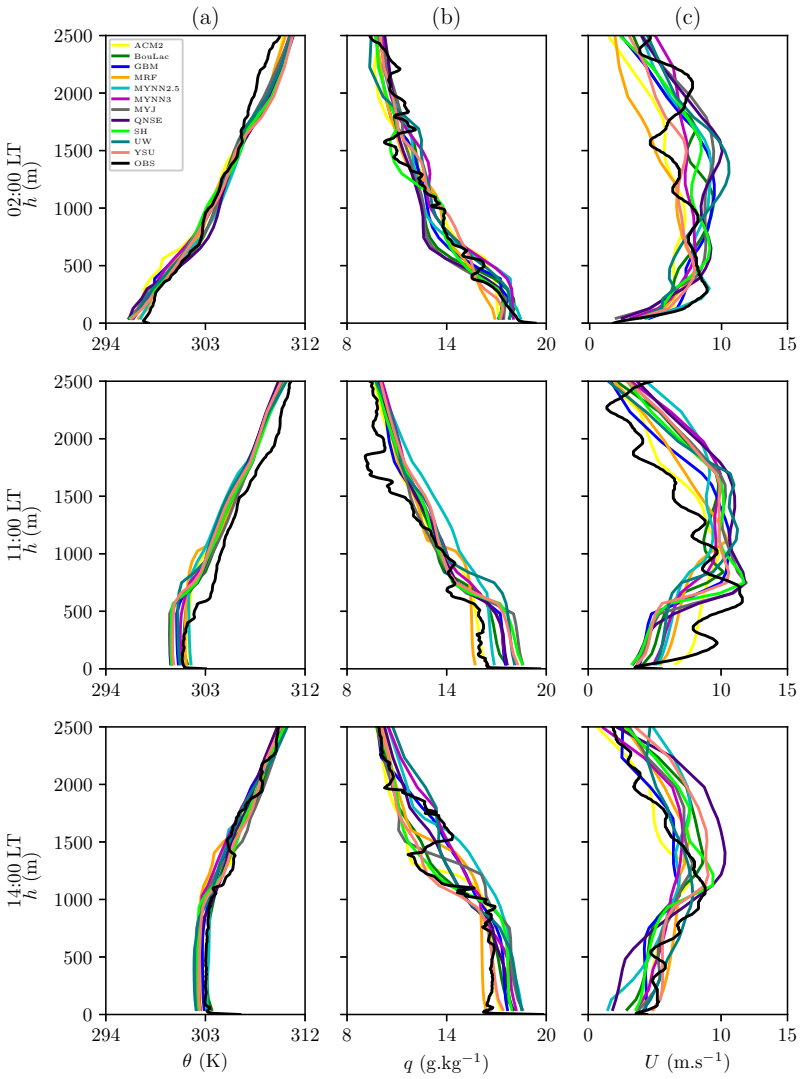

SOURCE: Author production.

Both MYNN2.5 and ACM2 schemes are 0.3 K warmer in the first 300 m height. Only the MRF scheme is 0.5 g.kg^{-1} drier below 600 m height, while the ACM2 scheme agrees within the observation. A well-mixed U profile is observed, whereas most PBL

schemes showed a log-wind behavior until ≈ 500 m height. In the well-mixed PBL at 14:00 LT, a quite unstable θ profile is observed within the CBL. Both BouLac and MYNN2.5 schemes showed a good agreement with observation and the rest of the PBL schemes predicted 0.5 K colder and 1.5 g.kg^{-1} wetter conditions within CBL. The PBLH$_{OBS}$ was 1396 m at this time. The MYJ, YSU, and SH schemes are 1.3 K warmer than the observation above the PBL top. The q profile obtained using the YSU scheme shows a fairly good agreement within PBL. No PBL scheme reproduced the inversion seen in the q profile near 1300 m height. The observed U profile reached 8.8 m.s^{-1} near the PBL top. UW (+0.5 m.s^{-1}) and YSU (+0.8 m.s^{-1}) schemes presented an overestimation of the observed U profile in comparison to other PBL schemes.

On March 4, the PBLH$_{OBS}$ increased 200 m between 00:00 (= 186 m) and 06:00 LT (= 386 m). During this period, most of the PBL schemes underestimated the observations. The QNSE (UW) schemes presented the deepest (shallowest) PBLH. After the sunrise, the PBLH$_{OBS}$ slightly decreased during the SBL erosion stage. In the early morning, the daytime PBL onset grows at a high rate (= 341 m.h^{-1}) between 09:00 and 10:00 LT. This is a lower growth rate during the CBL development stage compared to the previous days. The MYNN2.5 scheme depicted relatively well the PBL growth rate until 11:00 LT. The maximum PBLH$_{OBS}$ was 1305 m at 13:00 LT. The QNSE scheme showed good agreement with observations between 10:00 and 13:00 LT, although delayed (in 1-h) and overestimated (PBLH = 1546 m) the maximum PBLH$_{OBS}$. The MYNN3 scheme predicted the shallowest PBLH (= 268 m) at 13:00 LT. As the afternoon progresses into night, the PBLH$_{OBS}$ decays linearly and no PBL scheme depicts the shape of observation. The PBLH$_{ERA5}$ underestimates (≈ -300 m) the observations on March 4.

Figure 4.5 shows predicted θ, q, and U vertical profiles and corresponding soundings at 02:00, 11:00, and 14:00 LT on March 4. The MYNN3, QNSE, SH, and ACM2 schemes produced a 1.0 K colder condition than the observed below the first 500 m height at 02:00 LT. Almost all PBL schemes predicted a 1.0 K warmer conditions up to 500 m height. All PBL schemes presented a 0.7 g.kg^{-1} drier conditions and underestimated (-2.0 m.s^{-1}) the observed U profile. The QNSE scheme produced a 0.7 K colder near-surface atmosphere at 11:00 LT. All PBL schemes predicted a 2.0 K warmer PBL than the observed above 1000 m height. Both MYNN2.5 and MYNN3 schemes presented 1.4 g.kg^{-1} wetter conditions below the first 1000 m height. The observed U profile is underestimated by all PBL schemes at 11:00 LT. The UW scheme showed the highest wind speed (U = 12 m.s^{-1}) near 750 m

height. All PBL schemes produced a 2.8 K warmer conditions than the observation near-surface at 14:00 LT, and both MYJ and MYNN2.5 schemes presented a 1.0 g.kg^{-1} wetter environment. All PBL schemes produced 0.5 K colder and 2.1 g.kg^{-1} wetter conditions in the middle of the PBL. Above the PBL top, most of the PBL schemes produced 1.1 K warmer and 0.5 g.kg^{-1} drier conditions. All PBL schemes underestimated (-3.8 m.s^{-1}) the observed U profile.

Figure 4.5 - Vertical profiles of potential temperature (θ) in (a), vapor mixing ratio (q) in (b), and horizontal wind speed (U) in (c) on March 4, 2014. The radiosonde soundings time are indicated in y-axis label.

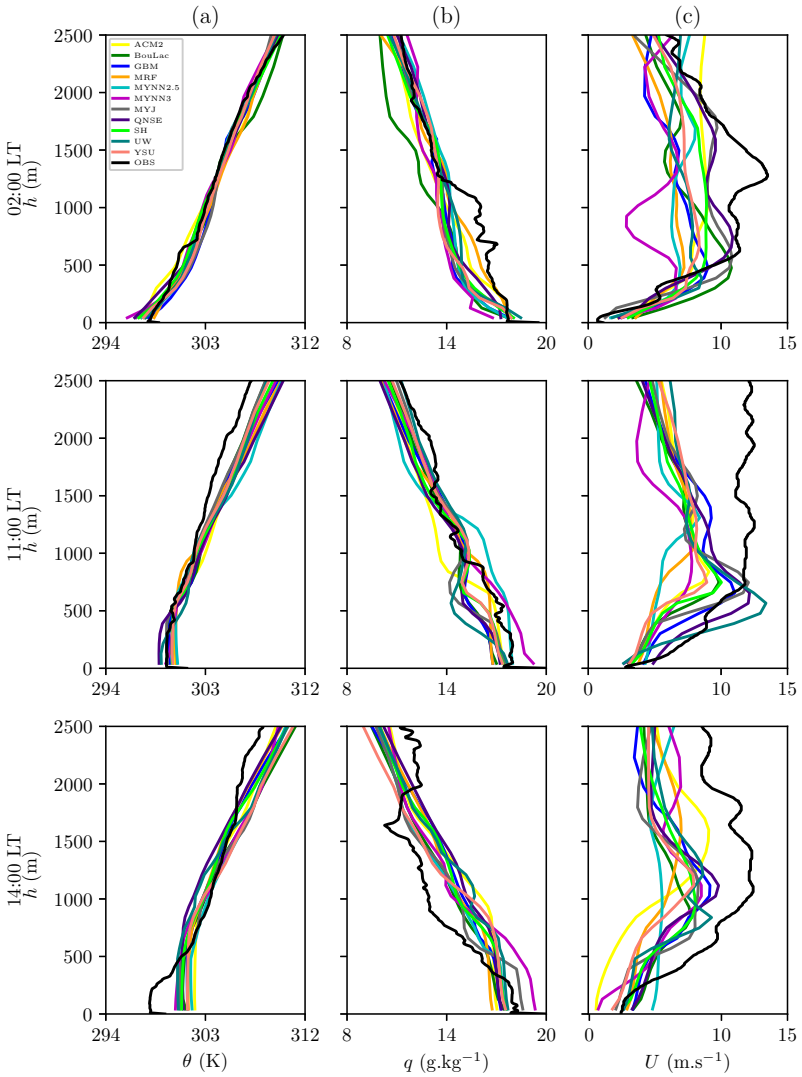

SOURCE: Author production.

Figure 4.6 shows the MAPE heatmap for PBLH at each hour on March 3 representing a complete day. The QNSE scheme exhibited MAPE higher than 150% during the early morning. The BouLac scheme had the lowest MAPE (= 16 %) at 02:00 LT. The MYNN3 scheme showed 0 % MAPE at 05:00 LT, while other PBL schemes showed MAPE values above 37 %. The $PBLH_{ERA5}$ data presented MAPE near 75 % at the same period. Some PBL schemes exhibited lower MAPE during the daytime including 1 % MAPE, such as the QNSE scheme at 10:00 LT and 0 % MAPE at 16:00 LT. The MYNN2.5 scheme had the lowest MAPE (= 4 %) at the time of maximum $PBLH_{OBS}$ (13:00 LT). The YSU scheme showed the lowest MAPE values after sunset, with 2 % at 19:00 LT. Both GBM and MRF schemes showed higher MAPE values during both the early morning (> 23 %) and early night (> 70 %). The ERA5 presented higher MAPE values (around 85 %) during the nighttime.

Figure 4.6 - MAPE heatmap for predicted PBLH on March 3, 2014. MAPE for ERA5 data is also presented.

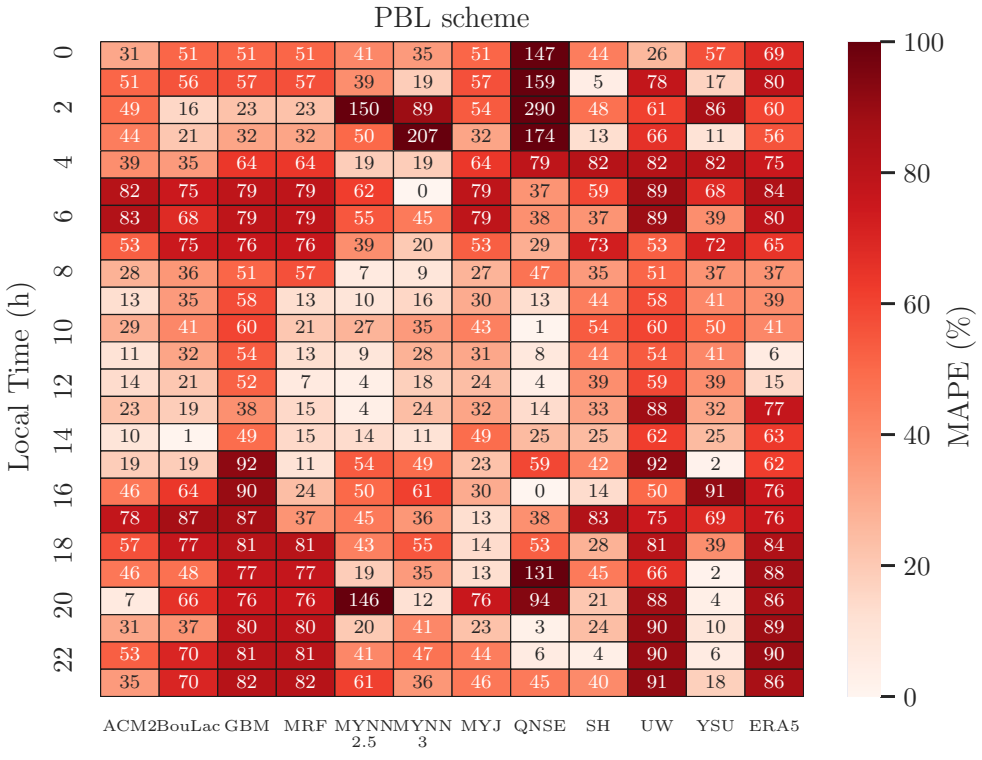

SOURCE: Author production.

The performance of PBL schemes under different stability regimes is separately evaluated for the daytime (06:00 − 18:00 LT) and nighttime (19:00 − 05:00 LT). Table 4.2 summarizes these statistical indexes for both periods. During the daytime, the average $PBLH_{OBS}$ is 873 m and all PBL schemes underestimated (in ≈ -500 m) presenting an average correlation coefficient of 0.6 and an average IOA of 0.61. The QNSE scheme produced the best statistical indexes (MB = -10 m, MAE = 279 m, RMSE = 355 m, IOA = 0.76) when compared to other PBL schemes. The MYNN2.5 scheme had the best correlation coefficient (r = 0.67) during the daytime. During the nighttime, the error indexes are smaller than daytime ones, which is expected considering the pronounced difference in PBLH between the daytime (deeper PBLH) and nighttime (shallower PBLH). The average $PBLH_{OBS}$ is 302 m. The MYNN3 scheme showed the best MB (= -24 m), despite presenting the worst correlation coefficient (r = -0.17). The SH scheme presented the best statistical indexes with the lowest error and best performance indicators (MB = -98 m, MAE = 115 m, RMSE = 143 m, r = 0.56, IOA = 0.64). The SH scheme also presented lower MAPE in the nighttime as 01:00 LT (5 %) and 22:00 LT (4 %) on March 3. All PBL schemes showed an average correlation coefficient of 0.16, with some showing negative values as MYNN3 (r = -0.17) and UW (r = -0.14) schemes. All PBL schemes presented an average IOA of 0.46. The PBLH from ERA5 not showed a better performance than the evaluated PBL schemes.

Table 4.2 - Statistical indexes for IOP1 PBL height in the daytime and nighttime.

	Average		**MB**		**MAE**		**RMSE**		**r**		**IOA**	
PBL scheme	Day	Night	Day	Night	Day	Night	Day	Night	Day	Night	Day	Night
ACM2	494	149	-3780	-153	416	172	507	206	0.61	0.14	0.64	0.46
BouLac	495	112	-379	-191	425	191	508	222	0.60	0.3	0.65	0.46
GBM	250	85	-624	-218	624	218	675	249	0.63	0.17	0.49	0.43
MRF	505	85	-369	-218	399	218	503	249	0.60	0.16	0.65	0.43
MYNN2.5	623	265	-251	-38	313	127	403	171	**0.67**	0.15	0.74	0.44
MYNN3	515	279	-359	**-24**	364	129	444	158	0.63	-0.17	0.64	0.33
MYJ	485	138	-389	-165	408	179	482	209	0.61	0.30	0.62	0.50
QNSE	864	422	**-10**	120	**279**	209	**355**	252	0.59	0.12	**0.76**	0.37
SH	415	205	-459	-98	467	**115**	539	**143**	0.56	**0.56**	0.56	**0.64**
UW	224	52	-650	-251	650	251	710	281	0.50	-0.14	0.46	0.40
YSU	393	229	-481	-74	482	114	566	154	0.54	0.29	0.54	0.56
ERA5	429	86	-445	-217	446	219	513	256	0.65	-0.14	0.60	0.41

SOURCE: Author production.

Figure 4.7 shows Taylor diagrams for PBLH during the IOP1 period in the daytime (a) and nighttime (b). PBL schemes presenting negative correlation coefficient values

(or much higher CRMSE) are not shown. A good forecast parameterization model should have a low centered-RMSE, a high correlation coefficient, and a standard deviation (σ) similar to the observation (TAYLOR, 2001). The SH scheme fulfills these requirements compared to other PBL schemes during the nighttime, which are dispersed and diverge greatly amongst them. This behavior was not observed during the daytime because all PBL schemes presented a similar and positive correlation amongst them. The QNSE, MRF, ACM2, and BouLac schemes had higher centered-RMSE and a standard deviation above the observation during the daytime. Despite the MYNN2.5 scheme presenting the best correlation coefficient, the MYJ scheme showed closer to the observed standard deviation. The PBLH from ERA5 data is closer to the MYNN3 scheme performance.

Figure 4.7 - Taylor diagram for IOP1 PBL height in the daytime (a) and nighttime (b). Polar contours in grey are centered-root-mean-squared-error.

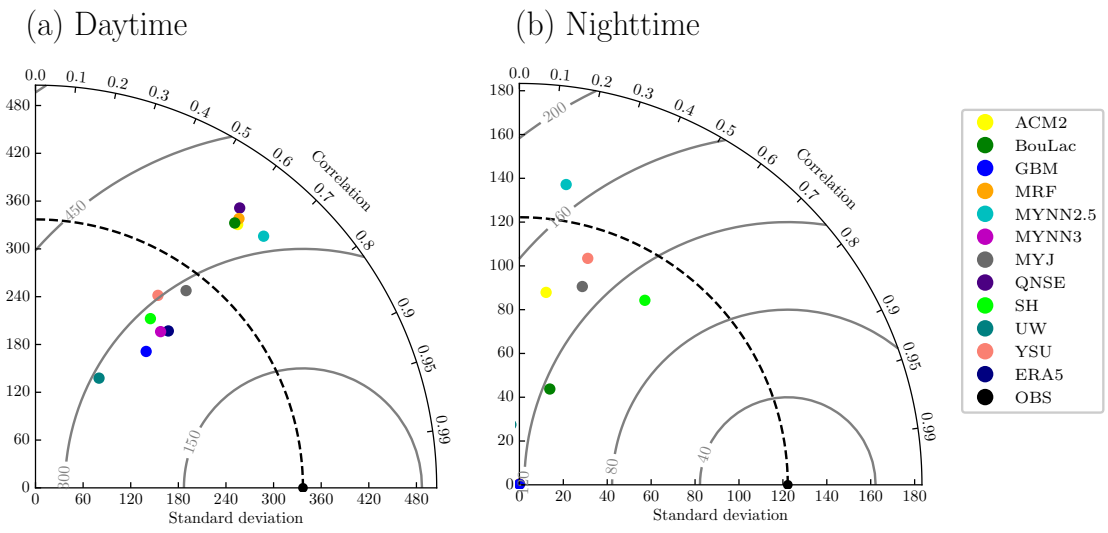

SOURCE: Author production.

Figure 4.8 shows the Taylor Skill Score (TSS) in a bar chart for both periods. The TSS is often employed to quantify the difference between model simulations and observation being an accuracy indicator (WANG et al., 2021), which reveals that most of the PBL schemes can better depict the PBLH during the daytime compared to nighttime. The MYJ (UW) scheme presented the best (worst) TSS equal to 0.80 (0.44) during the daytime, while the SH (GBM/MRF $\approx$ 0) scheme presented the

best (worst) performance at night with TSS equal to 0.75.

Figure 4.8 - Taylor Skill score bar chart for IOP1 PBL height in the daytime (a) and nighttime (b).

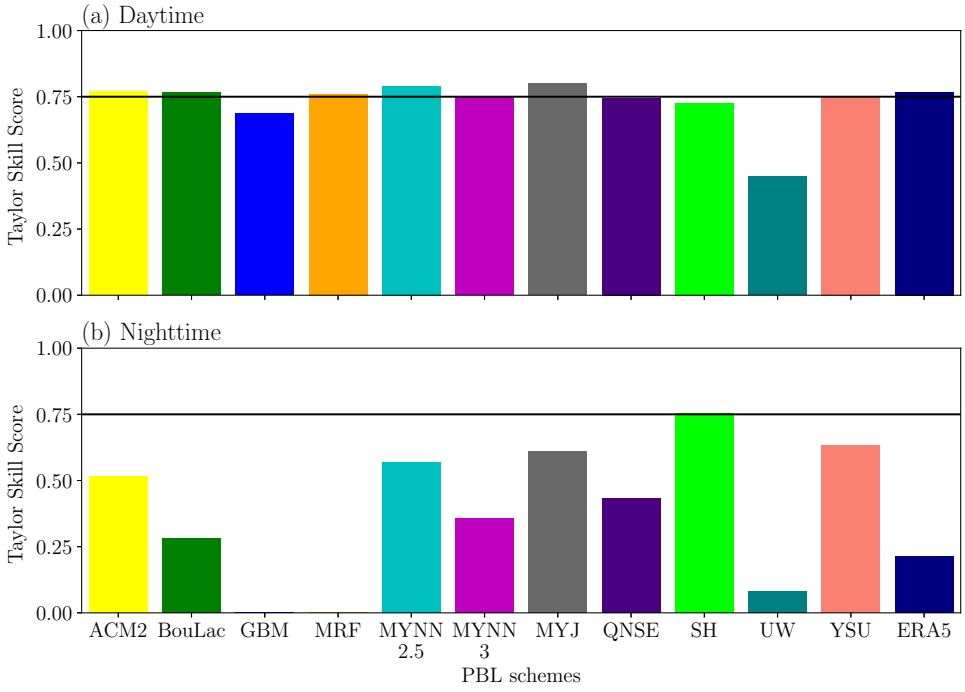

SOURCE: Author production.

The PBLH spatial fields are investigated to understand how PBL schemes depict the PBLH distribution across the central Amazon basin since there are only observations over the T3 site. Spatial variability for PBLH predicted amongst PBL schemes on March 3 is investigated at 02:00 LT representing the nighttime PBL (SBL) and at 14:00 LT representing the daytime PBL (CBL). The predicted PBLH from PBL schemes over T3, Manaus (3.10° S, 60.00° W), Negro River (3.09° S, 60.15° W), and Manacapuru Lake (3.30° S, 60.78° W) are compared to investigate differences between land and river locations. Figure 4.9 and Figure 4.10 show the PBLH contours for the 1-km horizontal resolution inner domain (d03) at 02:00 and 14:00 LT on March 3, respectively. A general view reveals that some PBL schemes are influenced by the rivers and lakes present in the Amazon basin. For instance, the MRF scheme (Figure 4.9d) produced a PBLH distribution that depicts the basin hydrography.

Moreover, the PBLH spatial fields showed higher PBLH over rivers and lakes than overland locations during the nighttime as the MRF scheme which produced lower PBLH ($\approx$ 84 m) in both T3 site and Manaus, while produced higher PBLH over Negro River (PBLH = 232 m) and Manacapuru Lake (PBLH = 329 m). The GBM scheme (Figure 4.9c) produced a PBLH distribution that was less river-influenced. The QNSE scheme (Figure 4.9h) produced the highest PBLH in both land and river locations (PBLH > 400 m).

Figure 4.9 - Spatial field contoured with PBLH over the inner domain (d03) at 02:00 LT on March 3, 2014. PBL schemes are indicated in the panels.

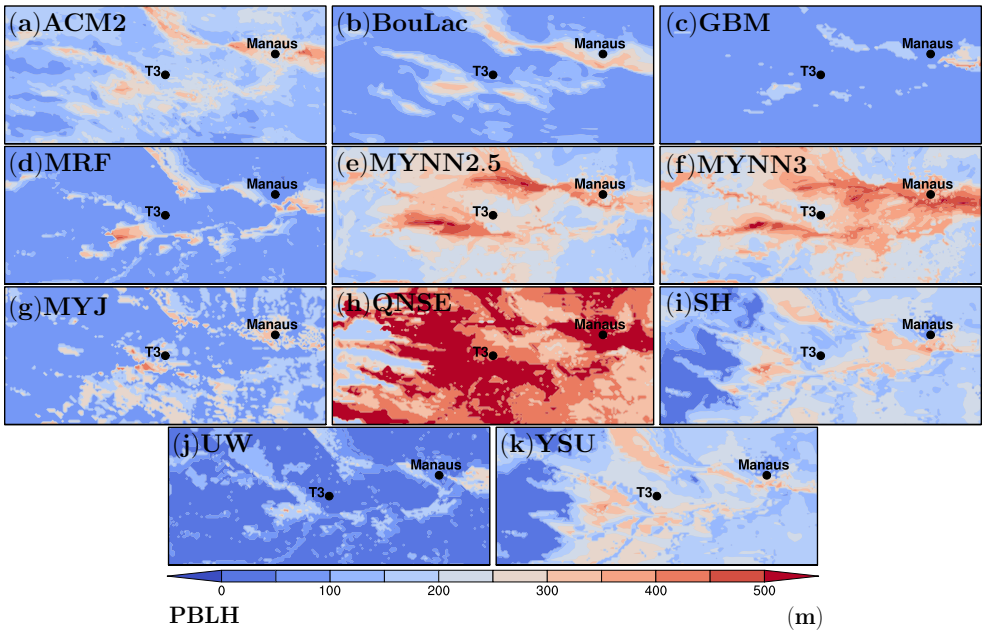

SOURCE: Author production.

In contrast with the nighttime PBLH (Figure 4.9), the daytime PBLH (Figure 4.10) spatial fields revealed an opposite behavior where all PBL schemes produced higher PBLH overland (e.g., PBLH_{ACM2} = 1612 m at Manaus) and lower PBLH over rivers (e.g., PBLH_{ACM2} = 126 m at Negro River). This happens due to the heating of the surface during the daytime. The QNSE scheme presented the highest PBLH overland (e.g, PBLH_{Manaus} = 2365 m). The ACM2 (Figure 4.10a) and MRF (Figure 4.10d) schemes notably depicted the basin hydrography in their predicted PBLH distribution across the domain (see Figure 3.1a for comparison). Both MYNN2.5 (Figure 4.10e) and MYNN3 (Figure 4.10f) schemes do not show this behavior. The

GBM (Figure 4.10c) and UW (Figure 4.10j) schemes predicted lower PBLH across the domain. Some 'hotspots' (i.e., localized higher PBLH) are seen in the PBLH distribution produced with the GBM scheme, which also shows streaks (interleaved regions of higher and lower PBLH) on the left side of the domain. These streak patterns are related to the TKE-based method of PBLH diagnosing (highly dependent on vertical motions) and the 1-km grid size resolution leading to the high variability in the diagnosed PBLHs (HEGARTY et al., 2017). The PBLH spatial fields from ERA5 data are not used for comparison due to their low resolution ($\Delta = 30$ km).

Figure 4.10 - Spatial field contoured with PBLH over the inner domain (d03) at 14:00 LT on March 3, 2014. PBL schemes are indicated in the panels.

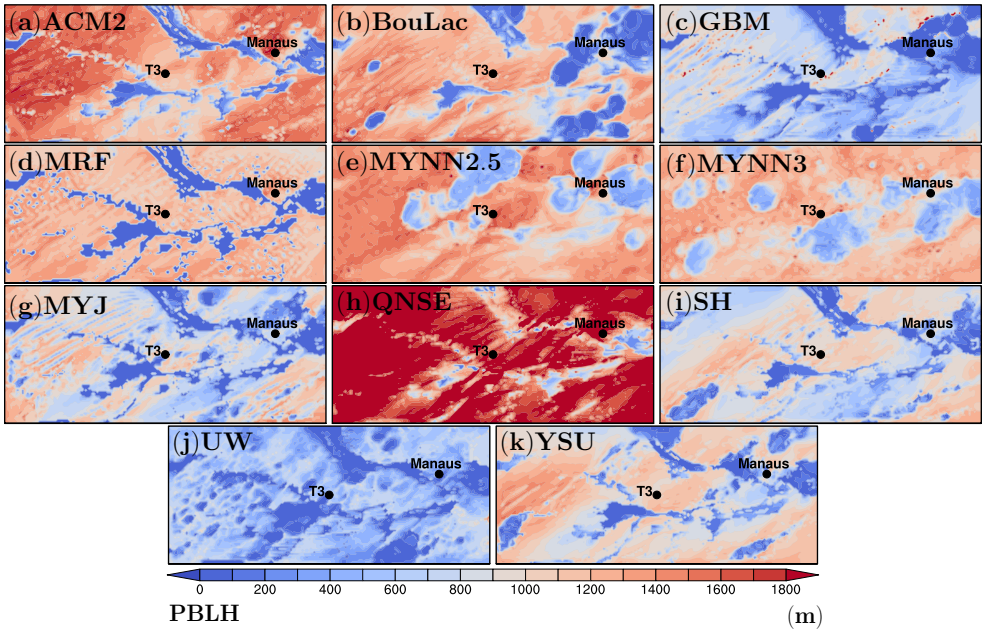

SOURCE: Author production.

4.1.3 IOP1 synthesis

The performance assessment of surface meteorological variables revealed that all PBL schemes underestimated the T_2 and almost all overestimated RH_2 (except the MRF scheme). The MRF scheme performed the best T_2 prediction. In contrast to the T_2 analysis, the best statistical indicators for RH_2 are spread amongst the evaluated PBL schemes, however, the MYJ scheme can be also considered the best choice for the prediction of this variable. All PBL schemes overestimated the 10-m wind speed

and based on lower errors and the average of both correlation coefficient and IOA amongst tested PBL schemes, the UW scheme performed the best U_{10} forecasting. The UW scheme produced a lower error and is indicated to forecast precipitation.

In the case of PBL diurnal cycle depiction through the prediction of PBLH and vertical structures, a better agreement is seen amongst predictions and observations from the second day of simulation. The differences are more pronounced in the thermodynamic vertical structures at nighttime (02:00 LT) and during the CBL development stage (11:00 LT), while the daytime CBL (14:00 LT) presents a better agreement with observations (as seen in the last row of Figure 4.4ab). The vertical profiles of wind speed (U) are worst represented compared to thermodynamic structures. Nonlocal PBL schemes, for instance, both MRF and ACM2 schemes tend to produce warmer and drier conditions in general, probably associated with their nonlocal transport. All PBL schemes showed difficulties to depict the shape of observed U profiles and sometimes present great divergence amongst them (as seen in the first row of Figure 4.3c).

The predicted PBLHs from the eleven PBL schemes are compared and evaluated to the observed PBLH estimated from the ceilometer measurements. All PBL schemes underestimated the observed PBLH during the first day of the simulation and are unable to depict the diurnal shape pattern. Based on the statistical analysis, two PBL schemes can be considered to perform daytime PBL simulations with good quality, which are the QNSE and MYJ schemes. Both GBM and UW schemes should be avoided. In the nighttime case, the SH scheme is by far the best performance compared to other PBL schemes. The UW scheme presented the worst performance during the nighttime. PBLH estimated from ERA5 data produced a relatively good (poor) performance during the daytime (nighttime). MAPE heatmap for March 3 (Figure 4.6) revealed what period of the day the observed PBLH is better depicted by PBL schemes. In general, both early morning and night periods are lesser well-depicted compared to the daytime.

The PBLH spatial fields revealed that during the SBL regime, some PBL schemes produce higher PBL over water bodies and lower over the land. In contrast, the opposite occurs during the daytime CBL (higher PBLH over the land and lower PBLH over water bodies). Besides, nonlocal PBL schemes (e.g., ACM2, MRF, and YSU) depict the hydrography basin in their PBLH distribution revealing how the presence of lakes and rivers impact the PBLH prediction. Hybrid PBL scheme based on TKE prognostic equation that include a EDMF term to nonlocal transport modeling, i.e.

the QNSE scheme, presented higher PBLH in both periods and produced a PBLH distribution less river-influenced compared to first-order nonlocal schemes.

The daily precipitation spatial field was investigated for the 72-h period in order to understand the rainfall distribution predicted through different PBL schemes. The MERGE product (ROZANTE et al., 2010) (precipitation observation plus estimative from satellite) is employed to compare with forecasts. Figure 4.11 reveals that all PBL schemes produced precipitation predominantly on the east part of the central Amazon basin with volumes reaching 120 mm. On the other hand, the MERGE data revealed a more homogeneous distribution across the whole domain with a maximum volume of around 80 mm. Both UW and GBM schemes were not able to predict the accumulated precipitation over the T3 site, while, for instance, the MYNN2.5, SH, and BouLac schemes produced a higher amount ($>$ 40 mm) than the MERGE data.

Figure 4.11 - Accumulated daily precipitation at 12:00 UTC on March 2, 2014. PBL schemes are indicated in the panels.

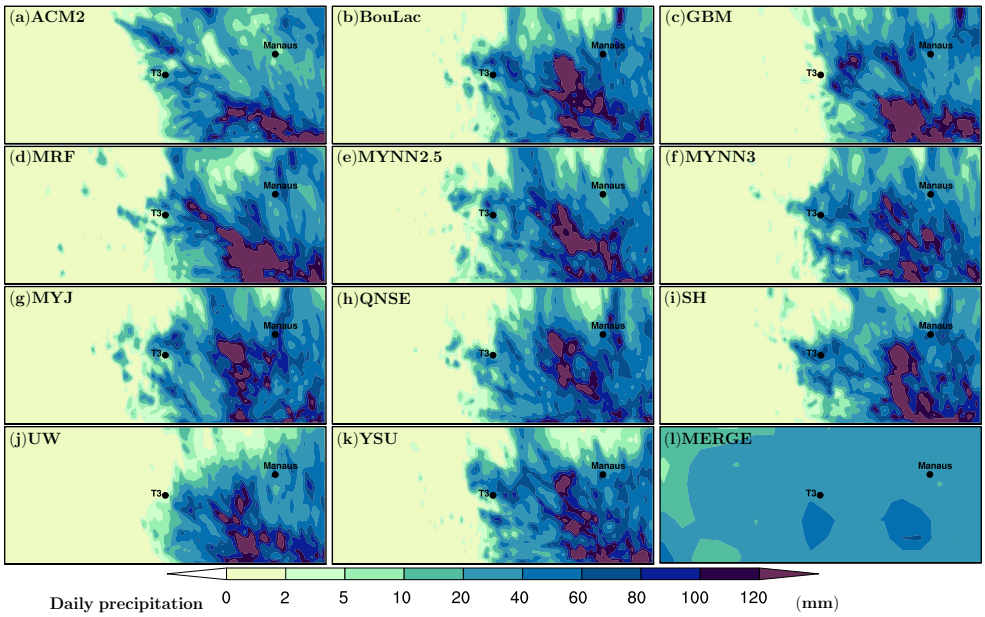

SOURCE: Author production.

In the case of the second-day comparison shown in Figure 4.12, almost all PBL schemes produced rainfall across the central Amazon basin including higher precipitation volumes (120 mm) positioned on the east side of the domain. Among PBL

schemes, the SH scheme predicted the highest volume over the T3 site. However, the MERGE data indicate a general and unique accumulated precipitation across the domain of around 2 mm, which indicates that PBL schemes predicted spurious amounts of rain during the period between March 2 and 3.

Figure 4.12 - Accumulated daily precipitation at 12:00 UTC on March 3, 2014. PBL schemes are indicated in the panels.

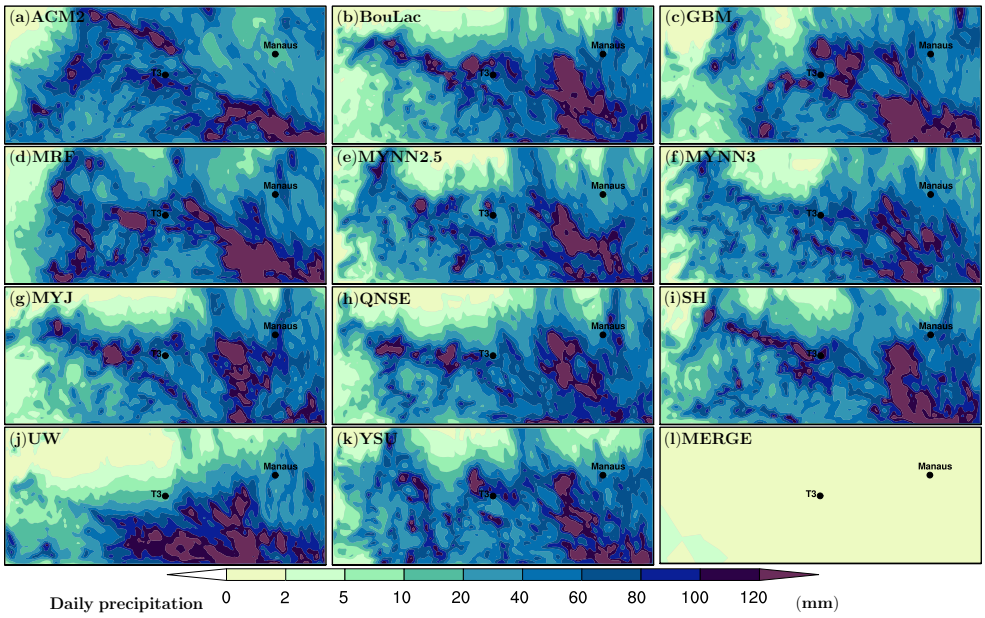

SOURCE: Author production.

For the case of the third day shown in Figure 4.13, the MERGE data indicates accumulated precipitation around 2 mm near Manaus, and 5 mm near the T3 site, while the higher volumes of rain are located on the west side of the domain. As in the previous days, almost all PBL schemes produced higher precipitation volumes on the east side of the domain. In comparison with MERGE data, all predictions forecasted higher volumes of precipitation than the observations. All model configurations were unable to depict reality in terms of daily accumulated precipitation. It brought significant differences not only to precipitation spatial fields but certainly impacted also other variables. This can been seen through the time-series of surface variables where all PBL schemes predicted colder and moister conditions than the observed, for instance, over the T3 site.

Figure 4.13 - Accumulated daily precipitation at 12:00 UTC on March 4, 2014. PBL schemes are indicated in the panels.

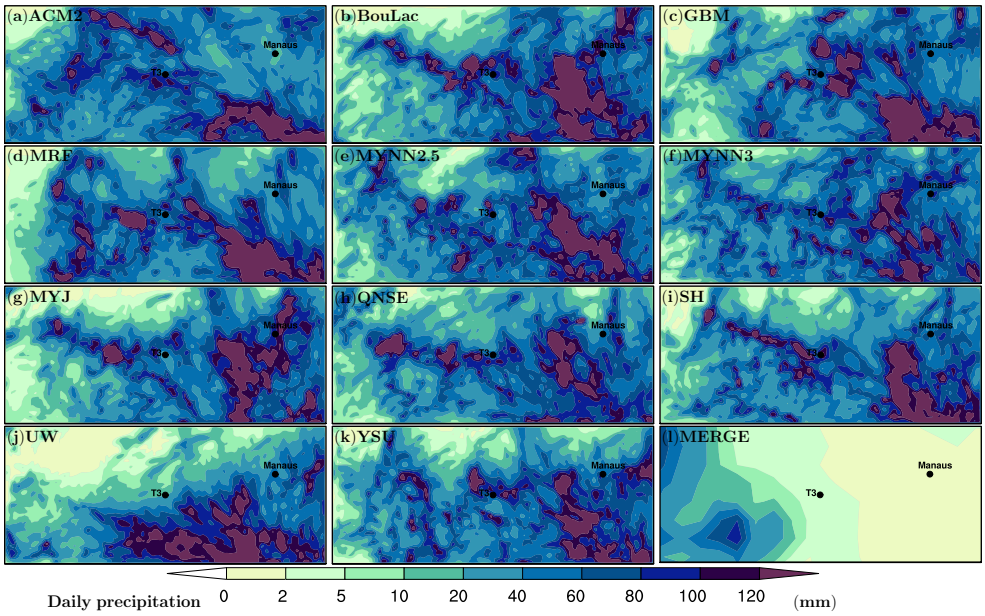

SOURCE: Author production.

4.2 IOP2 (2014 dry season)

4.2.1 Meteorological variables

Figure 4.14 shows the predicted meteorological variables from the eleven intercomparison experiments and corresponding observations. Both T_2 and RH_2 daily cycles show good agreement with the observed shape in the two first days. The observations on the third day showed that both warming and drying began two hours after sunrise (08:00 LT), which provoked lower temperatures (around -5.0 °C) and a wetter (around +20%) environment in contrast to the previous days. However, all PBL schemes initiate the diurnal warming and drying from the sunrise leading to higher temperatures and low humidity on October 2.

Figure 4.14 - Time series of predicted 2-m air temperature (a), 2-m relative humidity (b), 10-m horizontal wind speed (c), and precipitation (d) for IOP2.

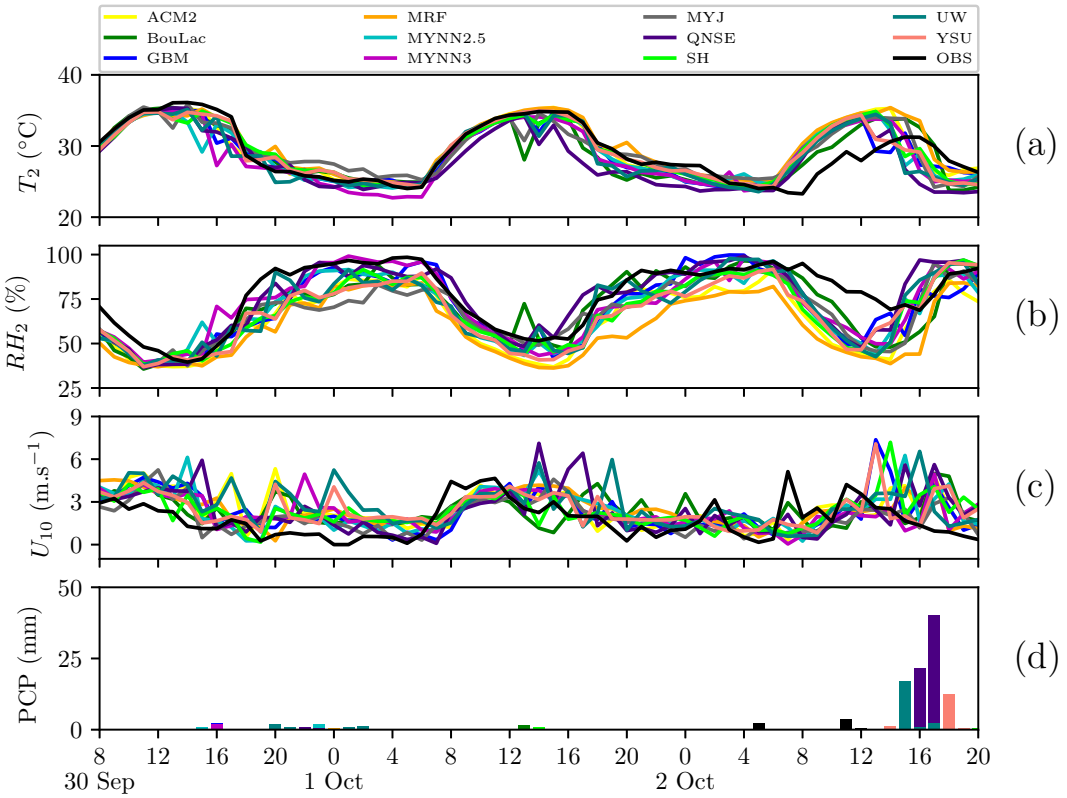

SOURCE: Author production.

Almost all PBL schemes well depicted the heating rates during the morning on the first two days, with nonlocal schemes closer to observations than local schemes. The MYJ (MYNN3) scheme predicted temperatures 1.4 °C warmer (1.5 °C colder) at night. The nighttime cooling is well depicted, with the latter two mentioned PBL schemes producing significant differences. Nonlocal schemes predicted the driest condition (e.g., MRF scheme around 15% drier), while local schemes are closer to observations (e.g., MYNN3 scheme around 5% drier). The spikes viewed in the MYNN2.5, MYNN3, QNSE, and UW schemes time series (mainly in the U_{10} time series, see Figure 4.11d) are probably related to the predicted rainfall amounts (non-observed) in the first and third days.

All PBL schemes overestimated the observed U_{10} during the 60-h period. No PBL scheme depicts the abrupt wind speed increase in the first two hours after sunrise on October 1 and 2. The PBL schemes, with either nonlocal or local mixing, tend to overestimate the U_{10} during the afternoon. Both the local BouLac and nonlocal SH schemes predicted a lower rainfall amount (less than 2 mm) between 13:00 and 14:00 LT on October 1, which perhaps explains the sudden cooling and moistening seen in their respective time series. Two rainfall episodes are observed on October 2, the first at 05:00 LT (PCP = 2.3 mm) and the second at 11:00 LT (PCP = 3.6 mm). No PBL scheme predicted this observed PCP, but the YSU, UW, and QNSE schemes predicted a non-observed PCP few hours later. The QNSE scheme produces the coldest (-3.8 °C) and wettest (+ 8%) conditions during the afternoon, which probably is associated with rainfall episodes. For instance, the QNSE scheme predicted rainfall of 40 mm at 17:00 LT when no PCP was observed. All PBL schemes overestimated the observed U_{10} from noon until the rest of the day. The YSU, UW, and QNSE schemes produced higher U_{10} during rainfall.

Table 4.3 presents the statistical indexes computed for meteorological variables over the 60-h analysis period. The average observed T_2 is $\approx$ 29.0 °C. Statistical indexes revealed that five local PBL schemes (BouLac, GBM, MYNN2.5, MYNN3, and UW) and one hybrid scheme (QNSE) underestimated the observed T_2, on the other hand, four nonlocal schemes (ACM2, MRF, SH, and YSU) and one local scheme (MYJ) overestimates. The YSU scheme presented the best statistical indexes for T_2 (MB = 0.1 °C, MAE = 1.2 °C, RMSE = 2.0 °C, r = 0.86, IOA = 0.93). The QNSE scheme showed the higher errors (MB = -1.1 °C, MAE = 2.3 °C, RMSE = 2.9 °C) and both lower correlation coefficient (r = 0.76) and IOA (= 0.85). The average observed RH_2 is 77 % and all PBL schemes underestimated it, with the QNSE scheme presenting the lowest MB (= -2 %). The MYNN3 scheme showed better statistical indexes

(MAE = 8 %, RMSE = 10 %, IOA = 0.91). Nonlocal schemes produced higher error, such as MRF scheme (MB = -17 %, MAE = 17 %, RMSE = 20 %). The average observed U_{10} is 1.7 m.s^{-1}. All PBL schemes overestimated the wind speed. The MYJ scheme presents the best statistical indexes (MB = 0.2 m.s^{-1}, MAE = 1.0 m.s^{-1}, RMSE = 1.3 m.s^{-1}, r = 0.42, IOA = 0.64). The UW scheme presented higher MB (= 1.0 m.s^{-1}) and error (MAE = 1.6 m.s^{-1}, RMSE = 2.0 m.s^{-1}). The average PCP is 0.1 mm. Despite the BouLac, MYJ, MYNN2.5, and MYNN3 schemes presented zero MB the ACM2 scheme showed lowest error (MAE = 0.1 mm, RMSE = 0.6 mm). The QNSE scheme presented the highest errors (MAE = 1.2, RMSE = 5.9 mm).

Table 4.3 - Statistical indexes for IOP2 near-surface variables computed over the 60-h analysis period.

Variable	**Statistical index**	**PBL scheme**										
		ACM2	BouLac	GBM	MRF	MYNN2.5	MYNN3	MYJ	QNSE	SH	UW	YSU
T_2	AVG	29.6	28.9	29.0	30.1	29.1	28.6	29.5	28	29.4	28.8	29.3
	MB	0.4	-0.2	-0.1	0.9	-0.1	-0.5	0.3	-1.1	0.2	-0.4	**0.1**
	MAE	1.4	1.5	1.4	1.4	1.7	1.9	1.8	2.3	1.5	1.6	**1.2**
	RMSE	2.3	2.1	2.1	2.3	2.4	2.5	2.3	2.9	2.2	2.4	**2.0**
	r	0.83	**0.86**	0.85	0.85	0.80	0.81	0.81	0.76	0.84	0.82	**0.86**
	IOA	0.91	0.92	0.92	0.91	0.89	0.89	0.89	0.85	0.91	0.9	**0.93**
RH_2	AVG	63	70	70	58	69	71	67	74	67	69	66
	MB	-13	-6	-6	-17	-7	-5	-9	**-2**	-9	-7	-10
	MAE	13	**8**	9	17	9	**8**	10	**8**	10	10	11
	RMSE	16	11	11	20	12	**10**	13	11	13	13	13
	r	**0.88**	0.87	0.87	0.86	0.86	0.86	0.82	0.83	0.84	0.82	**0.88**
	IOA	0.82	0.90	0.90	0.75	0.88	**0.91**	0.84	0.90	0.85	0.86	0.86
U_{10}	AVG	2.5	2.3	2.3	2.4	2.4	2.3	1.9	2.4	2.3	2.7	2.4
	MB	0.7	0.6	0.5	0.7	0.6	0.5	**0.2**	0.6	0.6	1.0	0.7
	MAE	1.3	1.2	1.2	1.2	1.2	1.2	**1.0**	1.4	1.2	1.6	1.3
	RMSE	1.7	1.5	1.6	1.5	1.6	1.6	**1.3**	1.8	1.5	2.0	1.6
	r	0.29	0.28	0.37	0.40	0.39	0.26	**0.42**	0.28	0.32	0.13	0.33
	IOA	0.53	0.53	0.58	0.60	0.58	0.53	**0.64**	0.50	0.56	0.43	0.55
PCP	AVG	0.0	0.1	0.0	0.0	0.1	0.1	0.1	1.1	0.2	0.4	0.2
	MB	-0.1	**0.0**	-0.1	-0.1	**0.0**	**0.0**	**0.0**	1.0	0.1	0.3	0.1
	MAE	**0.1**	0.2	**0.1**	**0.1**	0.2	0.2	0.2	1.2	0.3	0.6	0.3
	RMSE	**0.6**	0.7	**0.6**	**0.6**	**0.6**	1.0	1.1	5.9	1.4	2.3	1.7

* AVG is the average.

SOURCE: Author production.

4.2.2 Turbulent fluxes

Figure 4.15 shows the predicted turbulent fluxes from the eleven intercomparison experiments and corresponding observations. The turbulent heat fluxes time series (Figure 4.15ab) showed that the available net radiation (daytime conditions) is predominantly converted in LE. The average H is 30.0 W.m^{-2} with maximum values close to 120.0 W.m^{-2}, on the other hand, the average LE is 94.0 W.m^{-2} with maximum values around 300.0 W.m^{-2}. Daytime H reveals that all PBL schemes overestimated ($>$ 150 %) the observation, while in general a better agreement is seen amongst predictions and observations during the night.

Figure 4.15 - Time series of predicted sensible heat flux (a), latent heat flux (b), Bowen Ratio (c), and momentum flux (d) for IOP2.

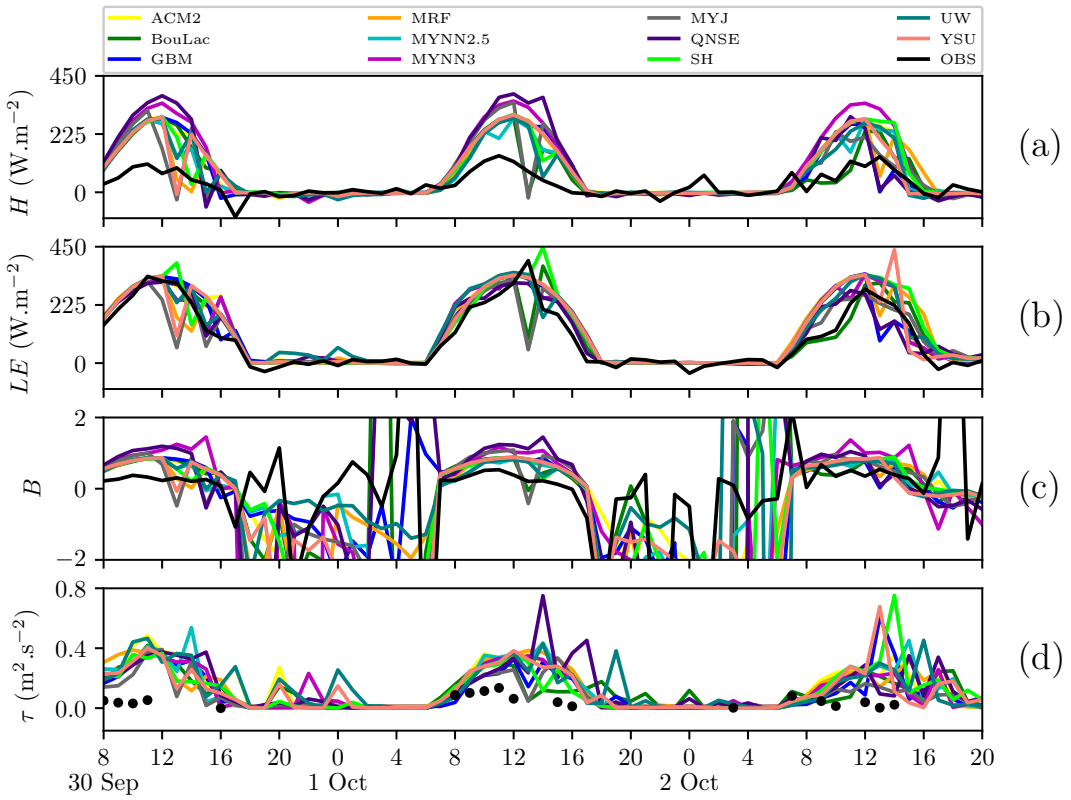

SOURCE: Author production.

Both QNSE and MYNN3 (YSU and MYJ) schemes showed higher (lower) H dur-

ing the daytime. In the case of LE, all PBL schemes showed a better agreement during the daytime than H. The first two days are better depicted, despite the BouLac scheme showing good agreement between the sunrise and noon on October 2. The Bowen ratio ($B = H/LE$) is estimated and revealed great divergence amongst predictions, with all PBL schemes showing similar behavior to the observations at night. The momentum flux (τ) is estimated from friction velocity (u_*) measurements that presented missing gaps in this studied period. Despite the gaps (predominantly in the nighttime), the visual comparison revealed that all PBL schemes overestimated ($+0.1-0.3$ m^2.s^{-2}) the τ during the daytime. Note that, the surface layer (SL) scheme calculates the surface exchange coefficients (using data from the land surface model) to compute the surface turbulent fluxes (SHIN; HONG, 2011). Although the PBL scheme is responsible to spread out the turbulent fluxes in the PBL, these fluxes come from the SL scheme formulation. The MYJ, MYNN3, and QNSE schemes make use of their specific SL scheme. The YSU, MYJ, and BouLac schemes showed abrupt reductions in both H and LE near noon on the first and second days, which is consistent with observations that showed reductions after the maximum values. For instance, the maximum observed LE was 396.0 W.m^{-2} at 13:00 LT and measurement indicates 207 W.m^{-2} at the next hour on October 1.

Table 4.4 presents the statistical indexes computed for turbulent heat fluxes over the 60-h analysis period. All PBL schemes overestimated H, where the forecast performed using the BouLac scheme showed better statistical indexes (MB = 35.1 W.m^{-2}, MAE = 50.9 W.m^{-2}, RMSE = 74.9 W.m^{-2}, IOA = 0.73). The ACM2, MYNN3, and SH schemes presented the highest correlation coefficient (r = 0.85). Both MYNN3 and QNSE schemes presented higher error (MAE $>$ 80 W.m^{-2}, RMSE $>$ 119.4 W.m^{-2}) compared to other PBL schemes. In the case of LE, all PBL schemes overestimated with the MYJ scheme presenting lowest MB (= 6.7 W.m^{-2}). The QNSE scheme presented lower error (MAE = 31 W.m^{-2}, RMSE = 43.9 W.m^{-2}), and the best IOA (= 0.96). The UW scheme showed the best correlation coefficient (r = 0.95). The performance index indicates that BouLac (QNSE) scheme is the best choice for H (LE) prediction. Based on performance indicators (r and IOA), the evaluated PBL schemes better depicted the LE when compared to H. The average coefficient correlation for the H is 0.79 and the average IOA is 0.67. For LE, the average correlation coefficient is 0.91 and the average IOA is 0.94. Statistical analyses were not performed for τ due to the presence of data gaps as already explained.

Table 4.4 - Statistical indexes for IOP2 turbulent fluxes computed over the 60-h analysis period.

Variable	**Statistical index**	**PBL scheme**										
		ACM2	BouLac	GBM	MRF	MYNN2.5	MYNN3	MYJ	QNSE	SH	UW	YSU
H	AVG	81.6	65.3	73.6	74.2	70.5	98.9	68.8	85.8	78.7	68.7	76.0
	MB	51.4	**35.1**	43.4	44.0	40.3	68.6	38.6	55.6	48.5	38.5	45.8
	MAE	62.7	**50.9**	59.6	60.6	52.0	80.7	60.5	80.1	59.2	54.1	61.4
	RMSE	90.8	**74.9**	88.7	87.1	78.1	119.4	90.1	120.1	87.1	79.5	89.0
	r	**0.85**	0.79	0.76	0.77	0.82	**0.85**	0.71	0.73	**0.85**	0.83	0.78
	IOA	0.69	**0.73**	0.67	0.67	0.72	0.61	0.65	0.58	0.70	0.72	0.68
LE	AVG	124.4	109.3	114.9	123.2	119	119	100.5	105.9	127.5	123	118.9
	MB	30.5	15.5	21.0	29.3	25.2	25.2	**6.7**	12.1	33.6	29.1	25.1
	MAE	38.9	33.4	35.8	45.1	36.1	36.1	37.1	**31.0**	43	39.4	42.5
	RMSE	55.8	56.6	53.1	63.2	52.6	52.6	66.1	**43.9**	63.8	50.6	64.4
	r	0.94	0.90	0.93	0.90	0.93	0.93	0.84	0.94	0.93	**0.95**	0.90
	IOA	0.95	0.94	0.95	0.93	0.95	0.95	0.91	**0.96**	0.94	**0.96**	0.93

* AVG is the average.

SOURCE: Author production.

4.2.3 PBL diurnal cycle and structure

Figure 4.16 presents obtained results for PBLH predictions and corresponding observations. The observed PBL heights evolved from 207 m at 08:00 LT until their maximum of 2516 m at 13:00 LT on September 30. The higher growth rate (= 849 m.h^{-1}) occurred between 10:00 and 11:00 LT. The GBM scheme presented the lowest PBLH (= 172 m) at 08:00 LT, while the QNSE scheme presented the highest PBLH (= 706 m). Visually, the QNSE scheme presented the deepest layer during the daytime along the period. The BouLac scheme presented the best agreement (PBLH = 2489 m) at the time of maximum PBLH$_{OBS}$, while the QNSE scheme showed the highest PBLH (= 3207 m), and the UW scheme predicted the lowest PBLH (= 622 m). The PBLH from ERA5 data overestimates (≈ 300 m) the observations in the morning and underestimates the rest of the day. Almost all PBL schemes underestimated (-300−1700 m) the observations during the afternoon, except the QNSE scheme.

Figure 4.16 - IOP2 planetary boundary layer height.

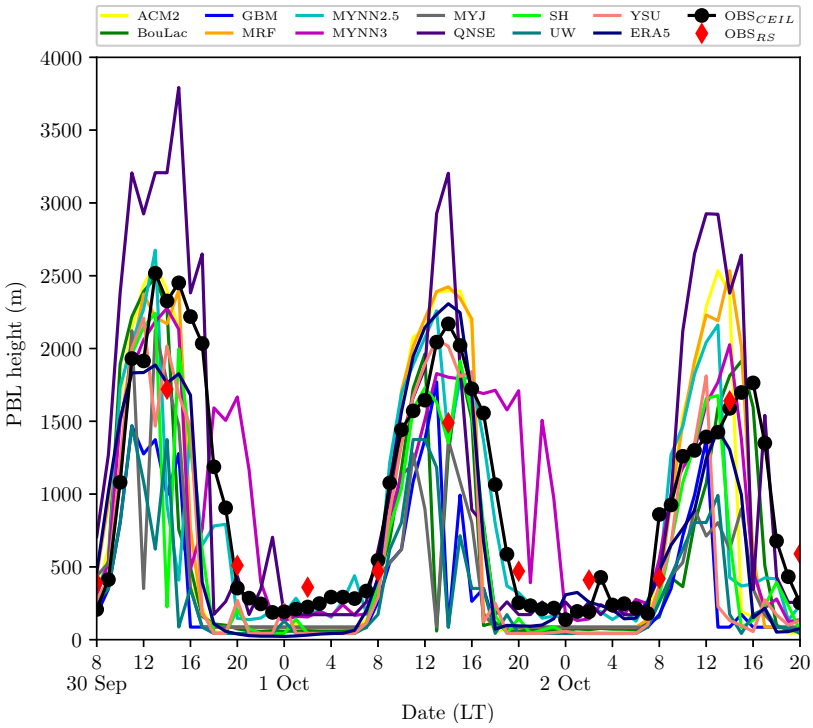

SOURCE: Author production.

The $PBLH_{OBS}$ presented a slight increase one hour after the peak when reached 2451 m at 15:00 LT. The MRF scheme showed this observed behavior with a better agreement (PBLH = 2402 m) compared to other PBL schemes. The $PBLH_{OBS}$ continuously decreased after the maximum to 187 m at 23:00 LT. Most of the PBL schemes underestimated the observations at night. The MYNN3 scheme produced the deepest layer (an average of 509 m) between the sunset on September 30 and the sunrise on October 1. The UW scheme produced the shallowest layer (an average of 50 m) amongst the evaluated PBL schemes during the same period. The ERA5 estimated the shallower nocturnal PBL (an average of 36 m) compared to all PBL schemes.

Figure 4.17 shows θ, q, and U vertical profiles predicted for all PBL schemes and corresponding radiosonde soundings on September 30. The comparisons with forecasting are at 08:00, 11:00, and 14:00 LT. No radiosonde sounding for θ is available at 08:00 LT. The evaluated PBL schemes do not produce great differences among them, except the MRF scheme that had an opposite behavior between 250 and 750 m height. In the case of the q profile, all PBL schemes produced a 1.4 $g.kg^{-1}$ drier environment below 1500 m height, while producing a 1.2 $g.kg^{-1}$ wetter condition between 1750 m and 2250 m. All PBL schemes overestimated ($\approx$ +2.0 $m.s^{-1}$) the observed U profile in the first 2500 m height, despite underestimates (-0.4−1.4 $m.s^{-1}$) above the 2000 m height. An LLJ was observed with 9.4 $m.s^{-1}$ near 300 m height, which all PBL schemes do not depict. All PBL schemes showed a warmer (+1.2 K) and drier (+1.8 $g.kg^{-1}$) bias below the first 1000 m height at 11:00 LT. A good agreement between the predicted θ profiles and the observations is seen from this height. All PBL schemes overestimated (+1.8 $m.s^{-1}$) the observed U profile below the first 1750 m height. A vigorously well-mixed layer is seen across 14:00 LT profiles. Both SH and YSU schemes present good agreement with the observed θ sounding within the PBL, while both local MYNN2.5 and MYNN3 schemes differ showing a colder (-0.4−0.7 K) bias. In general, all PBL schemes lie within the observed θ profile with the latter two referred PBL schemes showing the major differences. Although the YSU scheme well depicted the θ profile, it showed a wetter (+0.6 $g.kg^{-1}$) bias in the q profile. Both MRF and ACM2 schemes showed very good agreement with the observed q profile, while the other PBL schemes produced a wetter PBL (around +1.0 $g.kg^{-1}$). The MYNN2.5 presented the wettest (+0.8 $g.kg^{-1}$) condition in general. Most of the PBL schemes overestimated (+1.5 $m.s^{-1}$) the observed U profile. The local MYNN2.5 scheme produced the highest U ($\approx$ 10.0 $m.s^{-1}$) near-surface and the lowest ($\approx$ 4.0 $m.s^{-1}$) above 2000 m height.

Figure 4.17 - Vertical profiles of potential temperature (θ) in (a), vapor mixing ratio (q) in (b), and horizontal wind speed (U) in (c) on September 30, 2014. The radiosonde soundings time are indicated in y-axis label.

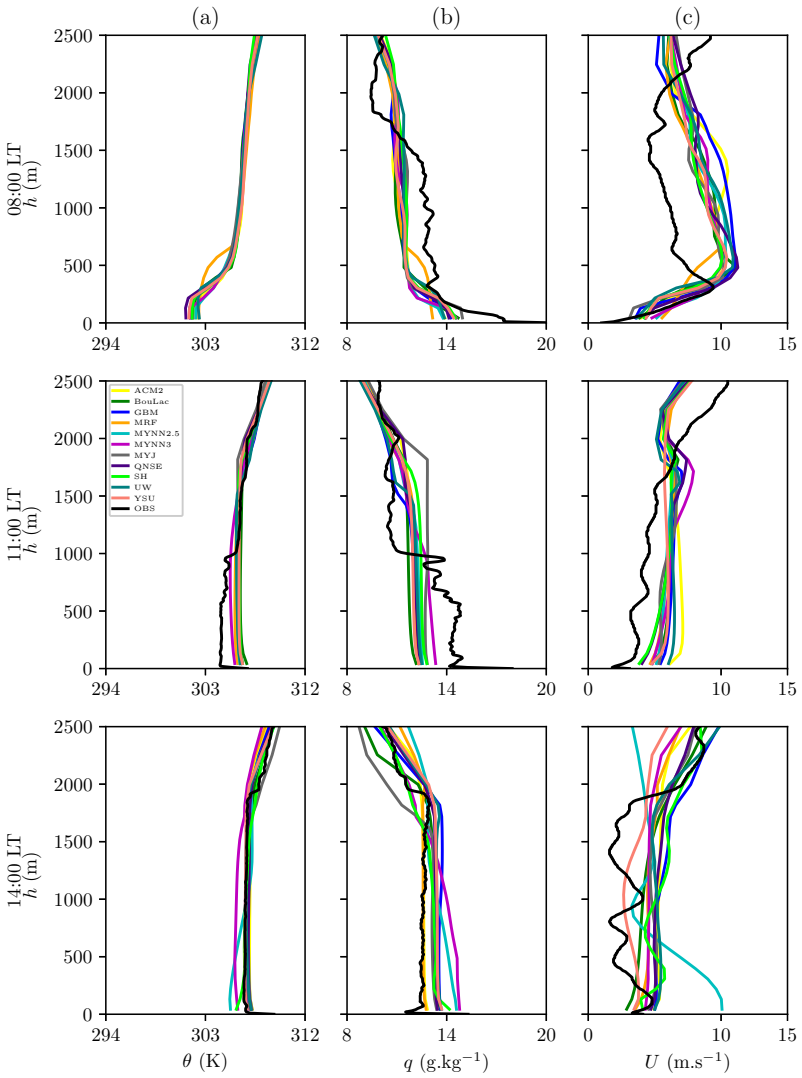

SOURCE: Author production.

During the early morning on October 1, the nocturnal PBLH_{OBS} presents an average of 248 m. The MYNN2.5, MYNN3, and QNSE schemes are closer to observation with the MYNN2.5 scheme presenting the best agreement (an average of 241 m). The UW scheme predicted the lowest nocturnal PBLH with an average of 54 m. The PBLH from ERA5 is shallower (an average of 38 m) than the predicted amongst most of the PBL schemes. From the sunrise, the PBLH_{OBS} (= 282 m at 06:00 LT) began to increase, which deepens more vigorously from 07:00 LT. The highest

growth rate is 531 m.h^{-1} between 08:00 and 09:00 LT. The PBLH$_{OBS}$ increases at moderated rates ($\approx$ 100 m.h^{-1}) between 10:00 and 12:00 LT. The PBLH$_{ERA5}$ showed great agreement during the PBL development, despite overestimates the observations from 11:00 LT. The maximum PBLH$_{OBS}$ is 2169 m at 14:00 LT and PBLH$_{ERA5}$ is 2308 m at this time. No PBL scheme depicted the observed peak with consistency in time and depth. Both ACM2 (PBLH = 2395 m) and MRF (PBLH = 2423 m) schemes overestimated the observed peak, and the QNSE scheme (PBLH = 3203 m) produced a higher overestimation. Both GBM and UW schemes reached a PBLH of only $\approx$ 86 m producing the shallower PBLH during the daytime. After the observed peak, PBLH$_{OBS}$ decreased until midnight reaching 137 m. Most of the PBL schemes underestimated the observations at night when the MYNN2.5 scheme presented a good agreement.

Figure 4.18 shows θ, q, and U vertical profiles at 02:00, 11:00, and 14:00 LT on October 1. During the nocturnal SBL stage at 02:00 LT, the observed θ increases 7 K in the first 500 m height. Most of the PBL schemes showed a colder (-0.6 K) bias near-surface, with the MYNN3 scheme producing the major difference (-2.0 K). Whilst, all PBL schemes produced 1.7 K warmer condition above 1500 m height. Almost all PBL schemes produced a wetter (+0.5−1.0 g.kg^{-1}) condition below the first 1000 m height, which the MYNN3 scheme predicted the wettest condition. Nonlocal schemes (e.g., ACM2, MRF, YSU) are closer to the observed q profile. All PBL schemes underestimated (-3.0 m.s^{-1}) the U profile in the first 1250 m and overestimated (+0.6−1.7 m.s^{-1}) above this height. An upper LLJ is observed with the jet core at 860 m height reaching 9.1 m.s^{-1}. During the CBL development stage at 11:00 LT, all nonlocal schemes produced a more vigorous well-mixed shape which is not seen in the observed θ profile. The QNSE scheme relatively depicted the observed θ profile shape showing a better agreement than other PBL schemes, which presented 1.0 K warmer conditions below 1000 m and above the 2000 m height. Nonlocal schemes (e.g., MRF, ACM2, YSU) produced the warmest (+ 1.0−2.0 K) conditions near-surface and local schemes (e.g., MYNN3, MYJ, UW) above 1000 m height. The MYNN3 scheme presented the warmest (+1.0−2.0 K) above 1400 m height. Both MRF and ACM2 schemes produced the driest (-0.8−1.2 g.kg^{-1}) conditions below 1000 m height. Above this height, the MYNN3 scheme produced the driest (-2.0 g.kg^{-1}) condition. The observed U profile presents an upper LLJ with 9.6 m.s^{-1} near 650 m height. All PBL schemes underestimated (-1.7 m.s^{-1}) the observed U profile and no PBL scheme predicts the LLJ. During the well-developed CBL at 14:00 LT, the MYJ scheme showed good agreement with the observed θ profile. All PBL schemes presented warmer (+6.0 K on average) conditions in the

first 2500 m height. Only the MYJ scheme produced a wetter (+1.0 g.kg^{-1}) condition inside the PBL whereas most of the PBL schemes are around 0.7−1.0 g.kg^{-1} drier. Both nonlocal MRF and ACM2 schemes produced warmer and drier conditions near-surface in contrast to colder and wetter conditions above the PBL top. The QNSE (MYJ) scheme produced a higher U ($\approx$ 10.0 m.s^{-1}) near-surface (above PBL top). Most of the PBL schemes overestimated (+0.2−1.2 m.s^{-1}) the observed U profile within the PBL.

Figure 4.18 - Vertical profiles of potential temperature (θ) in (a), vapor mixing ratio (q) in (b), and horizontal wind speed (U) in (c) on October 1, 2014. The radiosonde soundings time are indicated in y-axis label.

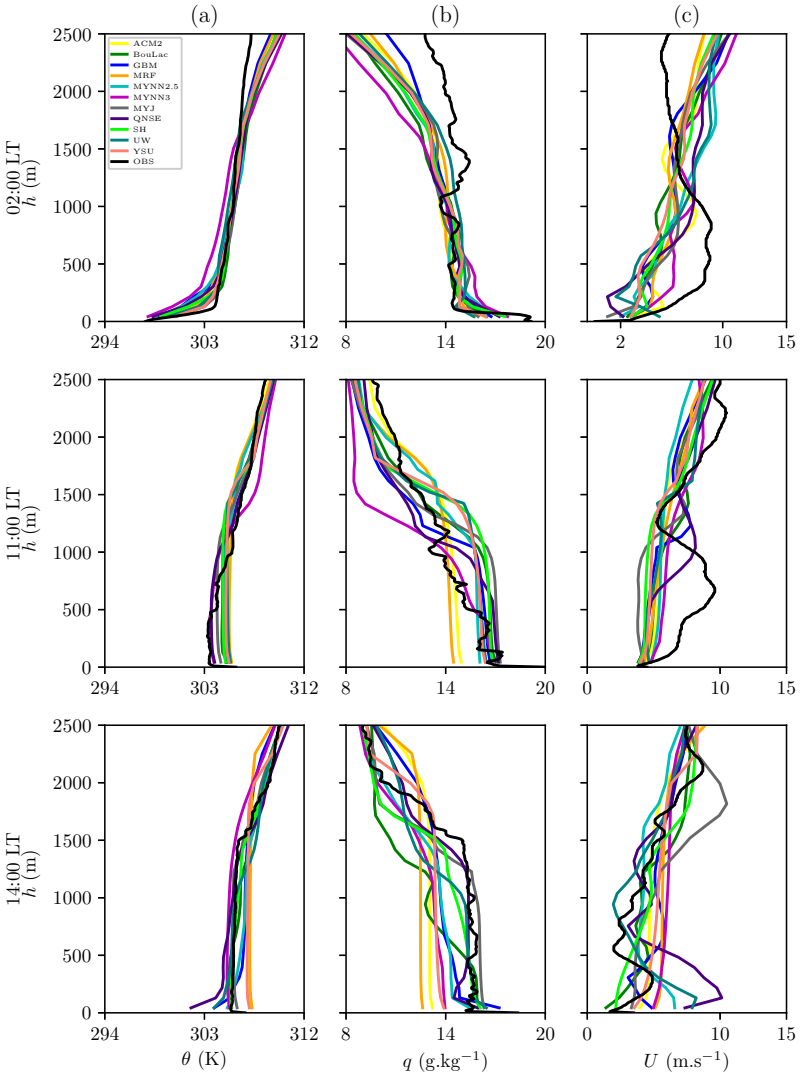

SOURCE: Author production.

During the early morning on October 2, the average $PBLH_{OBS}$ is 237 m. The PBLH from ERA5 data presented the best agreement with an average PBLH of 232 m. An increase in $PBLH_{OBS}$ was seen between 02:00 and 03:00 LT which no PBL scheme captured. A slight reduction from 04:00 ($PBLH_{OBS}$ = 238 m) to 07:00 LT ($PBLH_{OBS}$ = 180 m) is observed. This reduction is followed by an increase with a growth rate of 680 m.h^{-1}. The $PBLH_{OBS}$ is 860 m at 08:00 LT. After such growth, the observed PBL grows at low rates until 16:00 LT when reached its maximum of 1764 m. After the observed peak, the $PBLH_{OBS}$ decreased in the following hours. All PBL schemes do not depict the PBLH shape on the third day compared with the two previous days. The evaluated PBL schemes anticipate the maximum $PBLH_{OBS}$ in 4−5 hours in contrast to the previous days. The GBM, UW, and MYJ schemes visually underestimated the daytime $PBLH_{OBS}$, while the rest of the PBL schemes were overestimated. Most of the PBL schemes produced a deeper PBL between the late morning and early afternoon, while produced a shallower PBL in the afternoon, for instance, both the MYNN2.5 and MYNN3 schemes. The PBLH from ERA5 data underestimates ($\approx$ 465 m) the daytime $PBLH_{OBS}$. The QNSE (GBM) scheme produced the deepest (shallowest with an average of 337 m) with an average PBLH of 1523 m between sunrise and sunset.

Figure 4.19 shows θ, q, and U vertical profiles at 02:00, 11:00, and 14:00 LT on October 2. Both nonlocal ACM2 and MRF schemes produced 0.7 K warmer and 1.8−2.0 g.kg^{-1} drier conditions near-surface in contrast to above 1500 m height where predicted 0.8−1.0 K colder and 0.4−0.8 g.kg^{-1} wetter conditions at 02:00 LT. On the other hand, local schemes (e.g., MYNN3 and GBM) showed the opposite behavior presenting 0.3 K colder and predicted a 0.5 g.kg^{-1} wetter q profile near-surface. Above the 1500 m height, local schemes showed slightly colder (-0.2 K) and drier (-0.5−1.0 g.kg^{-1}) conditions. The BouLac scheme presents the driest (around -1.6 g.kg^{-1}) condition. Almost all PBL schemes overestimated the observed U profile near-surface and above 2000 m height. The MRF scheme presented higher U ($\approx$ 5.0 m.s^{-1}) near-surface and the BouLac scheme ($\approx$ 10.0 m.s^{-1}) in the upper portion. All PBL schemes diverge from the observed θ profile with a 1.3 K warmer bias during the CBL stage at 11:00 LT. The major difference is near-surface, where PBL schemes produced conditions around 4.0 K warmer. Nonlocal schemes (e.g., MRF, YSU, ACM2, SH) produced both warmer (+5.0 K) and drier (-2.0−3.0 g.kg^{-1}) conditions near-surface. Despite the local MYNN3 scheme showing good agreement with the observed q profile below the first 500 m height, this PBL scheme produced the driest (around -3 g.kg^{-1}) condition above 1250 m height. The MYNN2.5 scheme produced the wetter (+1.5 g.kg^{-1}) condition in the middle of PBL. No PBL scheme depicts

the observed U profile, most of them underestimate (-1.0−2.0 m.s^{-1}) near-surface and overestimate (-1.5−3.0 m.s^{-1}) above ≈ 1250 m height.

Figure 4.19 - Vertical profiles of potential temperature (θ) in (a), vapor mixing ratio (q) in (b), and horizontal wind speed (U) in (c) on October 2, 2014. The radiosonde soundings time are indicated in y-axis label.

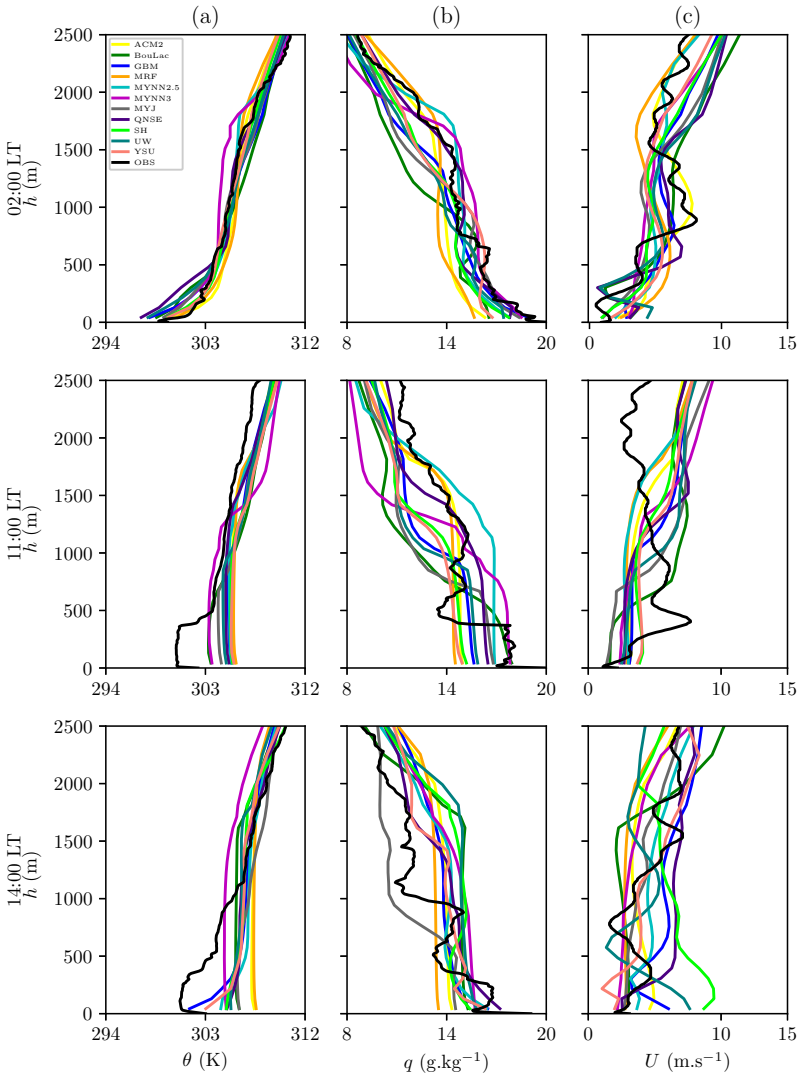

SOURCE: Author production.

Figure 4.20 shows the MAPE heatmap for PBLH at each hour on October 1. The ACM2, BouLac, GBM, MRF, MYJ, SH, UW, and YSU schemes presented in majority MAPE above 60% during the early morning, as well as at night. The PBLH from ERA5 data presented the same behavior. The MYNN2.5, MYNN3, and QNSE

schemes presented MAPE values lower than 50 % at the same period. Despite the MYNN3 scheme showing MAPE between 0 and 16% during the afternoon, the scheme produced MAPE above 300% in the nighttime. The SH scheme presented no error (MAPE = 0%) compared to observation at 11:00 LT. The YSU scheme at 13:00 LT, the MYNN3 scheme at 16:00 LT, and PBLH from ERA5 at 09:00 LT also showed 0% MAPE. The lowest MAPE (= 7%) during the time of maximum $PBLH_{OBS}$ (14:00 LT) is obtained with the YSU scheme. The MYNN2.5 scheme showed relatively lower MAPE across the entire day (mainly during the nighttime) compared to other PBL schemes. The YSU scheme showed lower MAPE values in the afternoon. The PBLH from ERA5 showed an average MAPE of 16% between 07:00 and 16:00 LT, while the MYNN2.5 scheme had an average of 24% at the same period.

Figure 4.20 - MAPE heatmap for predicted PBLH on October 1, 2014. MAPE for ERA5 data is also presented.

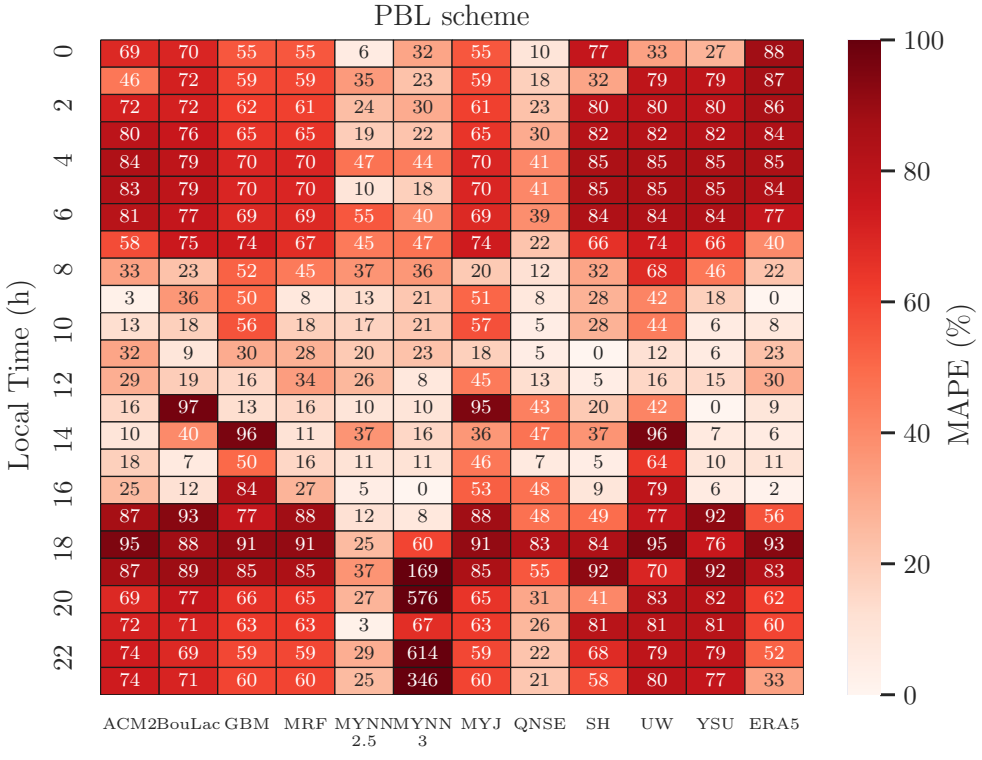

SOURCE: Author production.

Table 4.5 shows statistical indexes for PBLH during the daytime and nighttime. The average $PBLH_{OBS}$ is 1425 m during the daytime, and only the QNSE scheme overestimated (MB = 350 m) the $PBLH_{OBS}$. The MRF scheme presented the lowest MB (= -96 m). The MYNN3 scheme showed lower error (MAE = 362 m, RMSE = 534 m). The QNSE scheme showed the best correlation coefficient (r = 0.74) and the MYNN3 scheme the best IOA (= 0.83). All PBL schemes presented an average correlation coefficient of 0.57 and an average IOA of 0.68. During the nighttime, the average $PBLH_{OBS}$ is 291 m and only the MYNN3 scheme overestimates (MB = 242 m) the observations. Some PBL schemes presenting values close to zero as the QNSE (r = 0.02), ACM2 (r = 0.05), and YSU (r = -0.01) schemes. The MYNN2.5 scheme showed the best statistical indexes (MAE = 93 m, RMSE = 120 m, r = 0.76, IOA = 0.83). The IOA obtained with the MYNN2.5 scheme is practically twice as much compared to other PBL schemes. All PBL schemes presented an average correlation coefficient of 0.33 and an average IOA of 0.41. The PBLH from ERA5 data no outperforms PBL schemes in both periods.

Table 4.5 - Statistical indexes for IOP2 PBL height on daytime and nighttime.

	Average		**MB**		**MAE**		**RMSE**		**r**		**IOA**	
PBL scheme	Day	Night	Day	Night	Day	Night	Day	Night	Day	Night	Day	Night
ACM2	1277	63	-149	-228	603	227	802	276	0.59	0.05	0.73	0.37
BouLac	1002	66	-424	-225	588	225	808	270	0.56	0.65	0.70	0.38
GBM	565	86	-861	-205	861	205	1049	256	0.47	0.56	0.53	0.38
MRF	1330	86	**-96**	-205	556	205	717	256	0.63	0.43	0.76	0.38
MYNN2.5	1202	227	-224	-64	539	**93**	723	**120**	0.50	**0.76**	0.71	**0.83**
MYNN3	1242	533	-183	242	**362**	349	**534**	571	0.70	0.48	**0.83**	0.39
MYJ	678	86	-748	-205	779	205	936	256	0.56	0.34	0.60	0.38
QNSE	1776	236	350	**-55**	692	129	842	197	**0.74**	0.02	0.76	0.29
SH	963	69	-462	-222	522	222	746	272	0.61	0.10	0.71	0.38
UW	525	53	-900	-238	903	238	1101	280	0.34	0.30	0.50	0.37
YSU	965	66	-460	-225	549	229	778	279	0.62	-0.01	0.70	0.36
ERA5	1124	105	-302	-186	470	214	626	267	0.68	-0.19	0.78	0.30

SOURCE: Author production.

Figure 4.21 shows Taylor diagrams for PBLH during IOP2 in the daytime (a) and nighttime (b). During the daytime, both ACM2 and QNSE schemes values are not shown due to their higher standard deviation (> 900 m) compared to other evaluated PBL schemes. In addition, the daytime Taylor diagram reveals how the predicted PBLH using different PBL schemes are dispersed from each other. The MYNN3 scheme showed the best performance with a standard deviation closest to reference and the lowest CRMSE compared to other PBL schemes. The UW, GBM, and

MYJ presented a lower standard deviation than the reference. During the nighttime, the Taylor diagram agrees with computed metrical statistics indicating that the MYNN2.5 scheme is by far the best performance. The rest of the PBL schemes are closer to standard deviation with values lower than 20 m.

Figure 4.21 - Taylor diagram for IOP2 PBL height on the daytime (a) and nighttime (b). Polar contours in grey are centered-root-mean-squared-error.

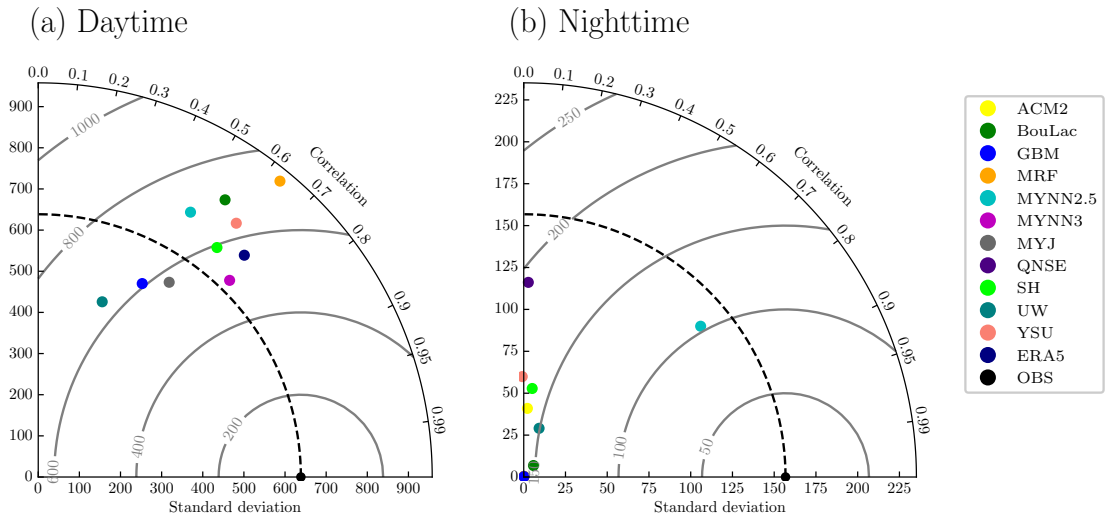

SOURCE: Author production.

Figure 4.22 shows the Taylor Skill Scores (TSS) in a bar chart for both periods. The Taylor Skill Scores revealed that the MYJ, SH, YSU, and MYNN3 schemes can be used to depict the daytime PBL with relatively similar performance. The MYNN3 scheme presents the best performance (TSS = 0.85) during the daytime, which confirms the computed metrics (see Table 4.5). The UW scheme presents the worst performance (TSS = 0.60) compared to other evaluated PBL schemes, and PBLH estimated from ERA5 data is between the best performance PBL schemes. The nighttime Taylor Skill Scores (Figure 4.22b) corroborates with the conclusion from Table 4.5, which the MYNN2.5 scheme (TSS = 0.87) is by far the best performance. The MYJ, BouLac, GBM, and MRF schemes produced TSS closer to zero in contrast with the daytime when showed a relatively good performance. The MYNN3 scheme presents a TSS equal to 0.19. The PBLH estimated from ERA5 data (TSS = 0.30) outperforms most of the PBL schemes (except both MYNN2.5 and QNSE).

Figure 4.22 - Taylor Skill score bar chart for IOP2 PBL height in the daytime (a) and nighttime (b).

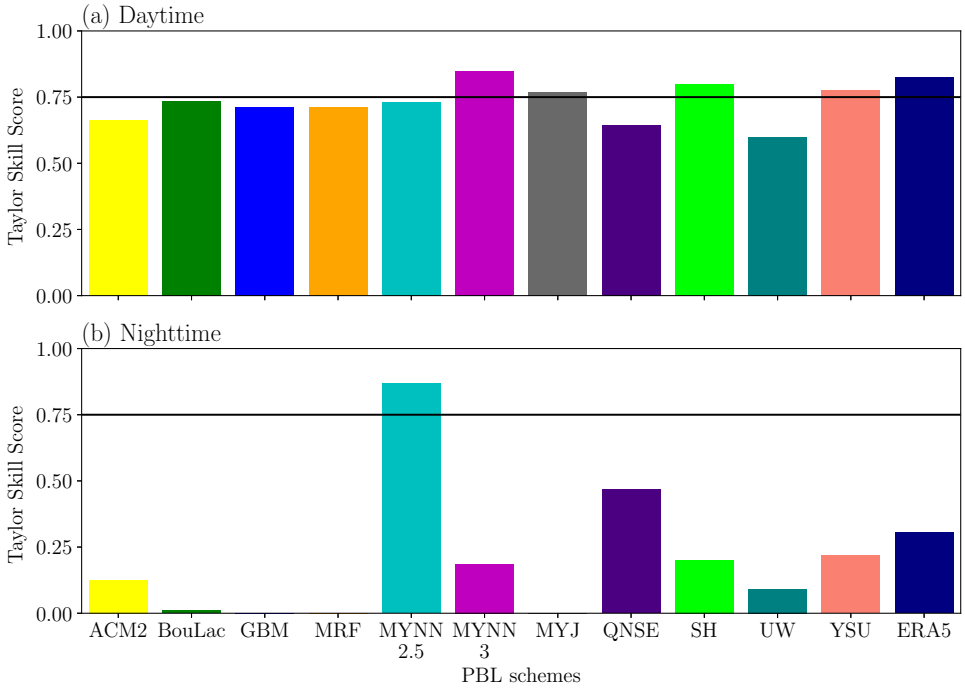

SOURCE: Author production.

Figure 4.23 shows PBLH contours for the inner domain (d03) at 02:00 LT on October 1. Some PBL schemes do not reproduce the basin hydrography in the PBLH distribution. For instance, the GBM scheme (Figure 4.23c) and MYJ scheme (Figure 4.23g) showed a homogeneous PBLH distribution across the basin, on the other hand, the UW scheme (Figure 4.23j) depicts the basin hydrography in his predicted PBLH contours. Most of the PBL schemes produced higher PBLH over rivers and lakes and lower PBLH overland as also seen in the IOP1. Most of the PBL schemes produced higher PBLH over Manaus city. The average predicted PBLH among PBL schemes is 91 m for the T3 site, 144 m for Manaus, 110 m for Negro River, and 116 m for Manacapuru Lake. The hybrid QNSE scheme (Figure 4.23h) and both local MYNN2.5 (Figure 4.23e) and MYNN3 (Figure 4.23f) schemes produced the deepest nocturnal PBL (around 150 m deeper) compared to other PBL schemes. Amongst nonlocal schemes, both MRF and ACM2 schemes presented a PBLH distribution less river-influenced compared to nonlocal YSU and SH schemes.

Figure 4.23 - Spatial field contoured with PBLH over the inner domain (d03) at 02:00 LT on October 1, 2014. PBL schemes are indicated in the panels.

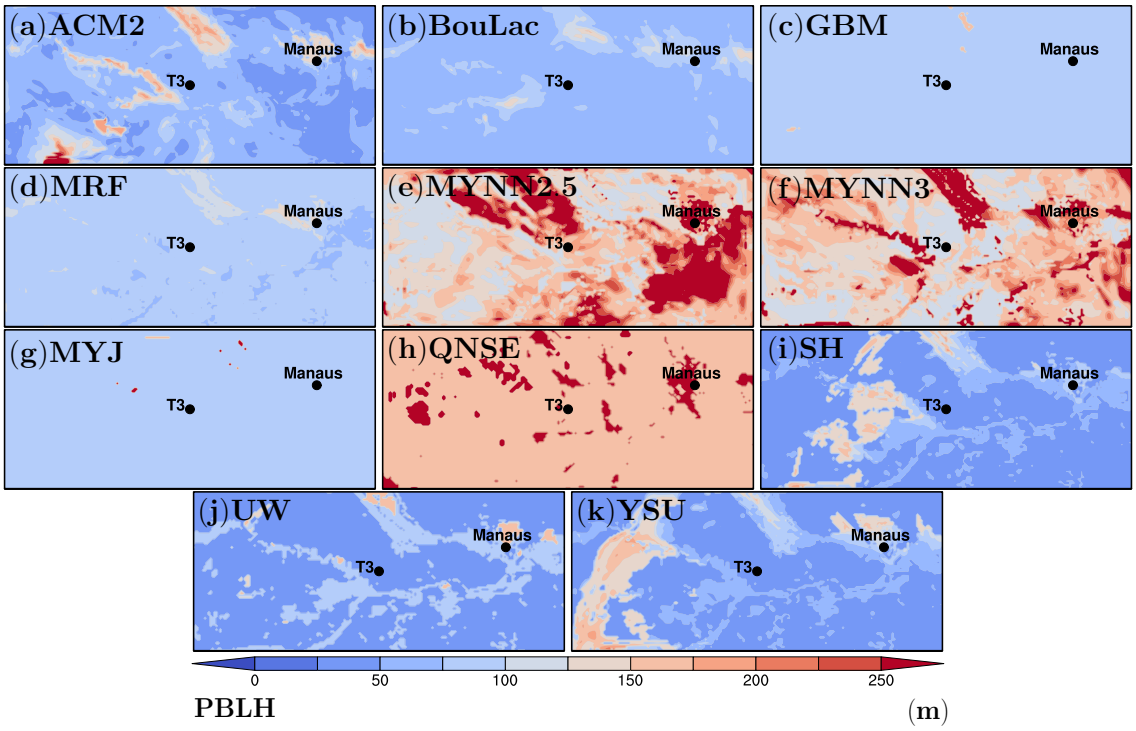

SOURCE: Author production.

Figure 4.24 shows PBLH contours for the inner domain (d03) at 14:00 LT on October 1. Nonlocal schemes (e.g., ACM2, MRF, YSU) reproduced the basin hydrography in his predicted PBLH distribution. The MRF scheme (Figure 4.24d) notably shows the basin hydrography in the predicted PBLH distribution. The MYNN3 scheme (Figure 4.24f) predicted a homogeneous deeper PBLH distribution, while the GBM scheme (Figure 4.24c) produced a shallower PBLH distribution without a defined pattern (i.e., the basin hydrography) and presented streaks. The QNSE scheme produced the deepest PBLH overland locations (e.g., $\text{PBLH}_{Manaus} = 2925$ m). The BouLac (Figure 4.24b), SH (Figure 4.24i), and UW (Figure 4.24j) schemes showed circular patterns of lower PBLH across the domain. The average predicted PBLH amongst PBL schemes is 1581 m for the T3 site, 1797 m for Manaus, 485 m for Negro River, and 390 m over Manacapuru Lake. Both MYJ (Figure 4.24g) and UW schemes presented a streak pattern in the left side of the domain with interleaved regions of higher and lower PBLH.

Figure 4.24 - Spatial field contoured with PBLH over the inner domain (d03) at 14:00 LT on October 1, 2014. PBL schemes are indicated in the panels.

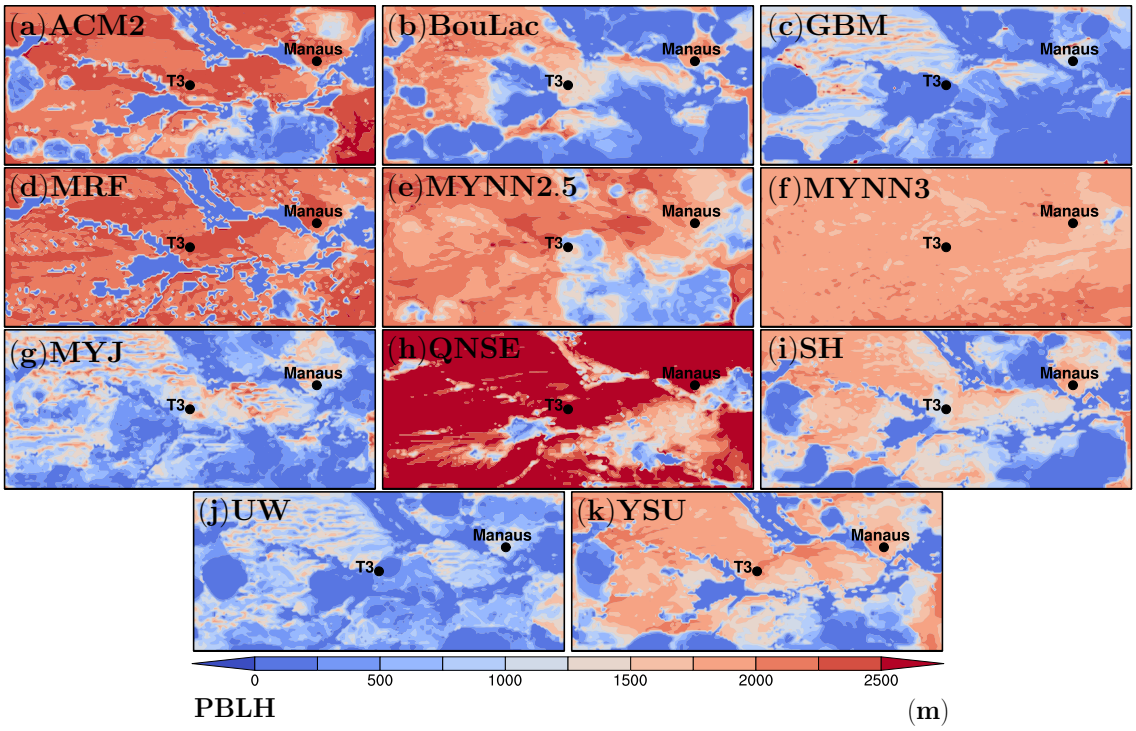

SOURCE: Author production.

4.2.4 IOP2 synthesis

The statistical analysis of surface meteorological variables revealed the YSU scheme as the best option for T_2 prediction. However, all PBL schemes showed higher performance indicators amongst them (e.g., higher correlation coefficient and IOA). The MYNN3 scheme is indicated to RH_2, which produced a lower error and the best IOA. The near-surface wind speed is better depicted through the forecast using the MYJ scheme. The ACM2 scheme is indicated to precipitation forecast compared to other evaluated PBL schemes.

The turbulent fluxes were studied in this period due to data availability. All PBL schemes better depicted the latent heat fluxes than sensible heat fluxes. The BouLac scheme showed the best performance for H, while the QNSE scheme is indicated for LE prediction. The Bowen ratio (B) was estimated from predicted and observed turbulent heat fluxes and showed great divergence amongst them. The statistical

analysis is not performed for momentum flux due to missing gaps in the observations, however, all PBL schemes visually overestimated ($+0.1-0.3$ $m^2.s^{-2}$) the τ during the daytime.

In the case of the PBL diurnal cycle, the PBL vertical structure is better depicted during the daytime mainly the well-developed CBL (14:00 LT). This is seen even in the first forecast day (see the last row of Figure 4.18ab). Nonlocal schemes tend to produce $1.0-4.0$ K warmer and $0.7-1.0$ $g.kg^{-1}$ drier conditions during the daytime, which is certainly related to their nonlocal transport. In the SBL stage, these PBL schemes produce $1.0-2.0$ K warmer and $0.8-1.2$ $g.kg^{-1}$ drier conditions near-surface while producing $0.8-1.0$ K colder and $0.4-0.8$ $g.kg^{-1}$ wetter in the upper portion (see the first row of Figure 4.19ab). In opposition, local schemes predict around 1.0 K colder and 1.0 $g.kg^{-1}$ wetter conditions (e.g., see the last row of Figure 4.17ab) in comparison with nonlocal schemes during the daytime. The wind speed vertical profiles are lesser depicted than thermodynamic structures, as also seen in the IOP1.

The QNSE scheme predicted a deeper PBLH along the forecasting period. As already discussed, the first two days are better predicted than the third day. Almost all PBL schemes underestimated the observed PBL during the daytime and nighttime, except the QNSE scheme (overestimation). The MAPE heatmap (Figure 4.20) shows that evaluated PBL schemes predict the daytime PBLH with less error than at night. The statistical indexes (see Table 4.5) revealed the MYNN3 scheme as the best option for the PBLH forecasting during the daytime. Both the Taylor diagram (Figure 4.21a) and the Taylor Skill Score chart (Figure 4.22a) confirm this. During the nighttime case, the best performance (by far) is achieved by the forecast using the MYNN2.5 scheme. Based on the Taylor Skill Score (Figure 4.21ab) interpretation, the MYNN2.5 scheme may be indicated to simulate both daytime and nighttime periods for the 2014 dry season.

The PBLH spatial fields during the nighttime (Figure 4.23) revealed that local schemes are less river-influenced than nonlocal schemes, except the UW scheme that showed a river-influenced PBLH distribution. The MYNN2.5, MYNN3, and QNSE schemes produced a higher PBLH across the domain. During the daytime case (Figure 4.24), local schemes showed shallower PBL (at least 150 m) than non-local schemes. The hybrid QNSE scheme produced the deepest PBL in both overland and water body locations.

4.3 IOP3 (2015 rainy season)

4.3.1 Meteorological variables

Figure 4.25 shows predicted surface meteorological variables from all the eleven intercomparison experiments and corresponding observations. The observed time series show the typical daily cycle pattern. The evaluated PBL schemes relatively well depicted the morning heating rates and underestimated the afternoon cooling with a better agreement near sunrise. The major differences are seen during the afternoon. All PBL schemes produced colder (1.2−2.0 °C) and wetter (+2−10%) conditions compared to the observations on March 2. The MRF (QNSE) scheme presented slightly warmer (colder) and drier (wetter) conditions during both the daytime and nighttime.

Figure 4.25 - Time series of predicted 2-m air temperature (a), 2-m relative humidity (b), 10-m horizontal wind speed (c), and precipitation (d) for IOP3.

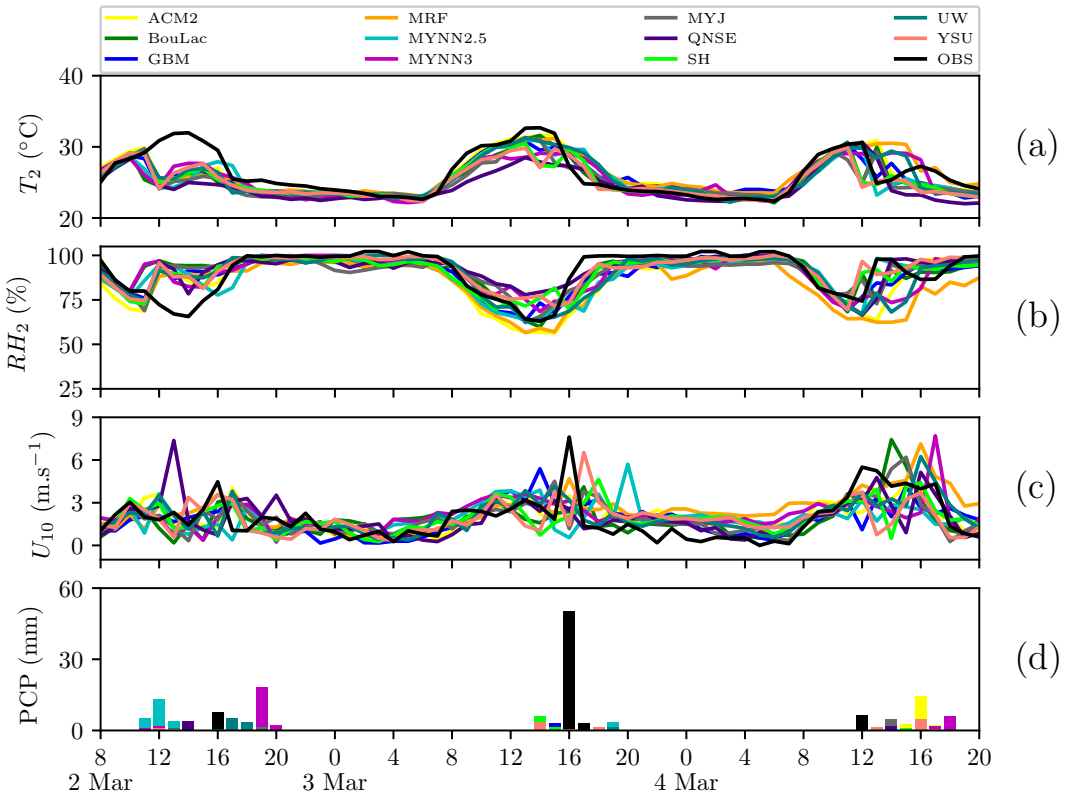

SOURCE: Author production.

A rainfall occurred between 16:00 and 17:00 LT (accumulated PCP of 9 mm) on March 2. The MYNN2.5 scheme overestimates the observed rain predicting rainfall of 23 mm between 11:00 and 14:00 LT. The UW scheme predicted rainfall between 16:00 and 19:00 LT (accumulated PCP of 10 mm), which may be interpreted as a distributed representation of the observed rain. The predicted U_{10} from all experiments lies within the observed variations during the daytime, while overestimates (+1.0-2.0 m.s^{-1}) at night. No PBL scheme can predict the abrupt increase in observed U_{10} during rainfall episodes along the period, for instance, during rainfall (PCP = 50 mm) at 16:00 LT on March 3 when the observed U_{10} was 7.6 m.s^{-1}. The MRF scheme predicted the closest value ($\approx$ 4.5 m.s^{-1}) at this time.

After this rainfall episode, the observed U_{10} decreases while all PBL schemes overestimate. The near-surface atmosphere becomes 7 °C colder and 33% moister between 15:00 and 17:00 LT, in which PBL schemes produce warmer (+0.5−2.0 °C) and drier (-10%) conditions probably related to non-prediction of the observed rainfall. The ACM2 scheme produced conditions 10−25% drier than the observations at the same period. After this rainfall episode, all PBL schemes presented warmer (+1.0−1.5 °C) and drier (-6−8%) conditions in the transition from the late afternoon on March 3 to sunrise on the next day (March 4). All PBL schemes predicted overestimated the observed U_{10} (+1.0−1.5 m.s^{-1}) at the same period. The MRF scheme produced warmer, drier, and higher wind speed conditions. No PBL scheme depicts the observed increase of U_{10} during the morning on March 4, even the PBL schemes that overestimated the wind speed at night. A rainfall with total precipitation of 8 mm occurred between 12:00 and 13:00 LT on March 4. No PBL scheme predicted this precipitation, although some PBL schemes delayed the observed rainfall as the nonlocal ACM2 scheme at 16:00 LT (PCP = 14 mm) and the local MYNN3 scheme between 17:00 and 18:00 LT (PCP = 8 mm).

Table 4.6 presents the statistical indexes computed for meteorological variables over the 60-h period. The average observed T_2 is 26.2 °C, which is underestimated by all PBL schemes. The MRF scheme practically shows a null MB (= -0.03 °C). The ACM2 scheme presents the best indexes (MAE = 1.3 °C, RMSE = 1.9 °C, IOA = 0.88), and the YSU scheme showed the best correlation coefficient (r = 0.81). The QNSE scheme presents the worst indexes (MB = -1.7 °C, MAE = 1.9 °C, RMSE = 2.7 °C, r = 0.71, IOA = 0.76). The average observed RH_2 is 90 %. The ACM2, GBM, MRF, MYNN2.5, and UW schemes underestimated the observed RH_2. The MRF scheme presented the highest MB (= -7 %) and BouLac scheme the lowest MB (= 0.3 %). The GBM scheme performed the best statistical indexes (MB = -1

%, MAE = 5 %, RMSE = 8 %, r = 0.77, IOA = 0.86). Whilst, the MRF scheme showed the highest error (MAE = 9 %, RMSE = 12 %). The average observed U_{10} is 1.8 m.s^{-1}. Both BouLac and GBM schemes underestimated the U_{10}. The UW scheme showed lowest error (MAE = 0.9 m.s^{-1}, RMSE = 1.3 m.s^{-1}) and the best correlation coefficient (r = 0.57). The YSU scheme presents the lowest MB (= 0.03 m.s^{-1}) and the MRF scheme showed the best IOA (= 0.76). The average observed PCP is 1.1 mm and all PBL schemes underestimated the observations. The ACM2 scheme showed the lowest MB (= -0.08 mm), BouLac scheme the lowest MAE (= 1.2 mm), and the YSU scheme the lowest RMSE (= 6.5 mm).

Table 4.6 - Statistical indexes for IOP3 near-surface variables computed over the 60-h analysis period.

Variable	**Statistical index**	**PBL scheme**										
		ACM2	BouLac	GBM	MRF	MYNN2.5	MYNN3	MYJ	QNSE	SH	UW	YSU
T_2	AVG	25.9	25.2	25.6	26.2	25.5	25.5	25.2	24.6	25.2	25.6	25.1
	MB	-0.3	-1.0	-0.6	**-0.03**	-0.7	-0.7	-1.1	-1.7	-1.0	-0.6	-1.1
	MAE	**1.3**	1.5	1.4	1.4	1.4	1.6	1.6	1.9	1.4	1.5	1.4
	RMSE	**1.9**	2.2	2.0	2.2	2.1	2.1	2.4	2.7	2.2	2.1	2.1
	r	0.79	0.77	0.79	0.73	0.78	0.77	0.73	0.71	0.79	0.78	**0.81**
	IOA	**0.88**	0.84	0.86	0.84	0.86	0.85	0.81	0.76	0.84	0.87	0.84
RH_2	AVG	86	90	89	83	88	90	90	91	90	89	91
	MB	-4	**0.3**	-1	-7	-2	0.9	0.8	0.8	0.7	-2	0.7
	MAE	7	6	**5**	9	6	6	6	6	6	**5**	**5**
	RMSE	10	9	**8**	12	9	9	9	**8**	**8**	9	**8**
	r	0.73	0.67	**0.77**	0.65	0.72	0.70	0.66	0.72	0.74	0.71	0.76
	IOA	0.82	0.81	**0.86**	0.74	0.84	0.83	0.78	0.81	0.83	0.83	0.85
U_{10}	AVG	2.0	1.8	1.8	2.4	2.0	2.1	1.9	1.9	2.0	2.0	1.9
	MB	0.1	-0.04	-0.05	0.6	0.1	0.2	0.1	0.05	0.1	0.1	**0.03**
	MAE	1.0	1.0	1.0	1.0	1.2	1.1	**0.9**	**0.9**	1.0	**0.9**	1.1
	RMSE	**1.3**	1.4	1.4	**1.3**	1.7	1.4	1.4	1.4	1.4	**1.3**	1.6
	r	0.50	0.52	0.46	0.63	0.14	0.47	0.49	0.48	0.44	**0.57**	0.25
	IOA	0.67	0.69	0.65	**0.76**	0.40	0.63	0.68	0.68	0.63	0.73	0.51
PCP	AVG	0.4	0.1	0.1	0.0	0.5	0.5	0.1	0.1	0.2	0.2	0.3
	MB	**-0.08**	-1.1	-1.0	-1.2	-0.7	-0.6	-1.0	-1.0	-0.9	-0.9	-0.9
	MAE	1.5	**1.2**	1.3	**1.2**	1.6	1.7	1.3	1.3	1.4	1.3	1.3
	RMSE	6.8	6.6	6.6	6.6	6.9	7.0	6.6	6.6	6.6	6.6	**6.5**

* AVG is the average.

SOURCE: Author production.

4.3.2 PBL diurnal cycle and structure

Figure 4.26 presents obtained results for PBLH predictions and corresponding observations. The observed PBL heights evolved from 245 m at 08:00 LT to 1226 m at 14:00 LT on March 2. The PBL growth occurred almost linearly with an average growth rate equal to 160 m.h^{-1}. All PBL schemes do not show consistency in time and depth and most of them overestimate (underestimate) the observations during the morning (afternoon). The PBLH from ERA5 showed a really good agreement with PBLH$_{OBS}$ between 13:00 and 17:00 LT (daytime PBL), with a slight overestimation (PBLH$_{ERA5}$ = 1264 m) at the time of maximum PBLH$_{OBS}$. Most of the PBL schemes anticipate their maximum PBLH and produced a shallower PBL during the afternoon. After the observed peak, the PBLH$_{OBS}$ decreased to 119 m at midnight. The average PBLH$_{OBS}$ is 215 m between sunset and midnight. The MYNN2.5 (PBLH = 263 m), MYNN3 (PBLH = 358 m), and QNSE (PBLH = 572 m) schemes overestimate the average PBLH$_{OBS}$ at this referred period. The PBLH estimated from ERA5 data presents a shallower PBL with an average PBLH of 52 m.

Figure 4.26 - IOP3 planetary boundary layer height.

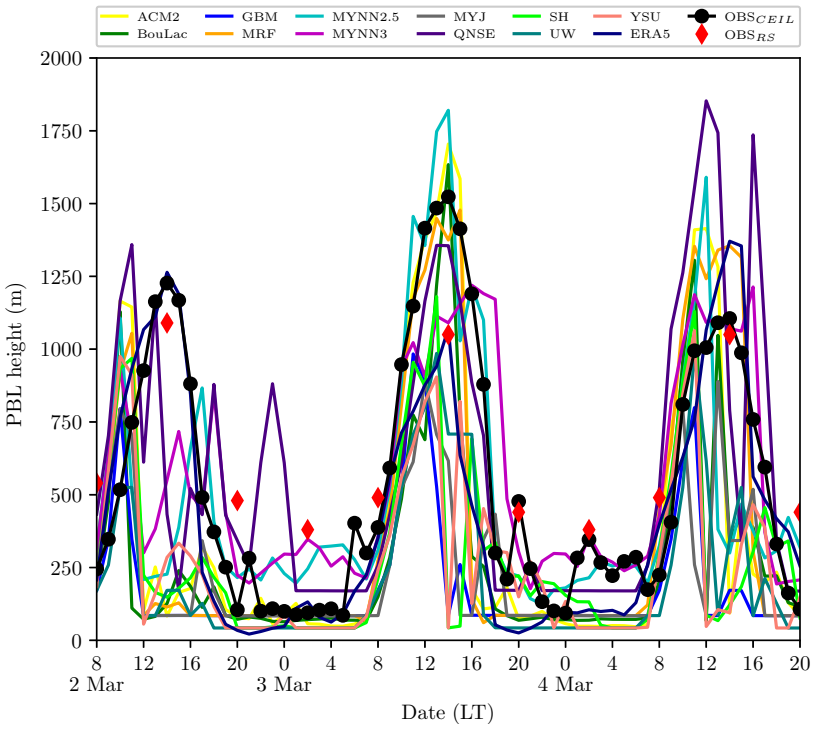

SOURCE: Author production.

Figure 4.27 shows θ, q, and U vertical profiles at 08:00 and 14:00 LT on March 2. No radiosonde soundings are available for the CBL development stage (11:00 LT) in both IOP3 and IOP4. The predicted θ profiles are closer to each other and lie within observations above 750 m height. All PBL schemes present warmer (+1.0−2.0 °C) and wetter (+0.6−1.8 g.kg^{-1}) conditions near-surface. Above 2000 m height all PBL schemes produced a slightly drier (-0.5 g.kg^{-1}) condition.

Figure 4.27 - Vertical profiles of potential temperature (θ) in (a), vapor mixing ratio (q) in (b), and horizontal wind speed (U) in (c) on March 2, 2015. The radiosonde soundings time are indicated in y-axis label.

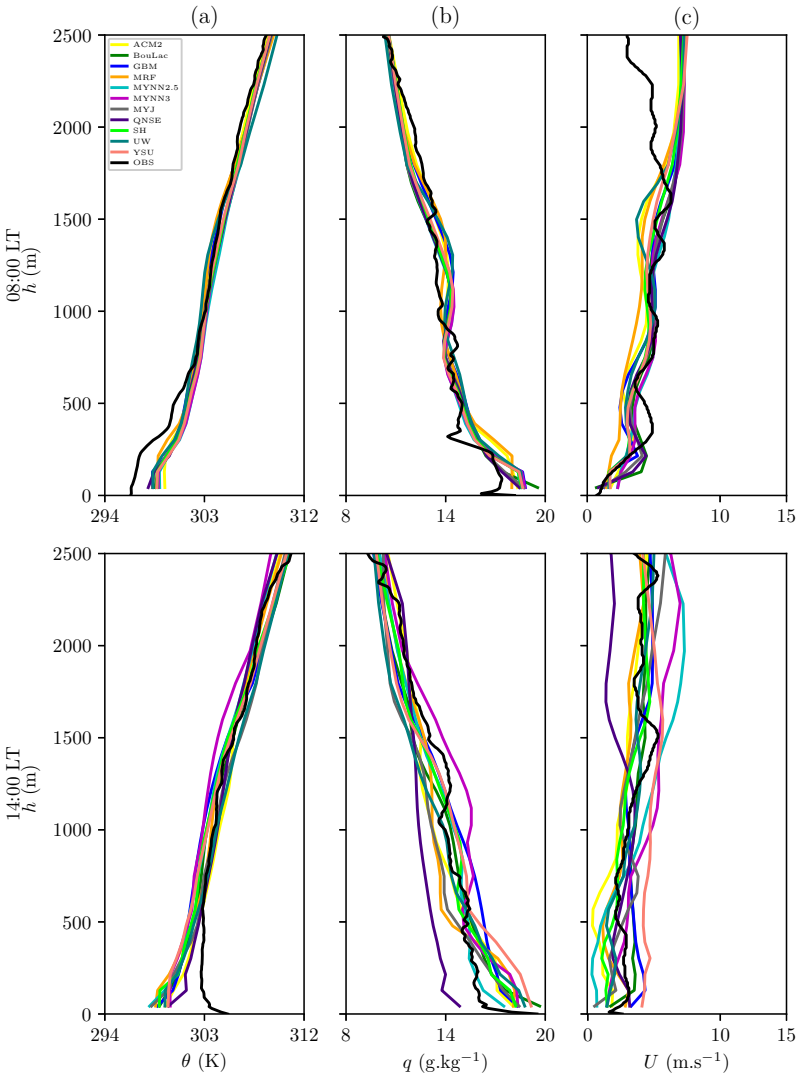

SOURCE: Author production.

All PBL schemes predicted U profiles that lie within the observed in the first 1750 m height. Above this height, all present an overestimation (+2.0−4.0 m.s^{-1}). All PBL schemes produced a colder (-1.4−2.5 °C) condition below the first 500 m height at 14:00 LT. The MRF scheme showed good agreement above this height, while the MYNN3 scheme produced the coldest (around -1.8 °C) condition. The QNSE scheme produced the driest (-1.8 g.kg^{-1}) condition near-surface and the wettest (+0.4 g.kg^{-1}) above the 2000 m height, on the other hand, the YSU scheme showed the opposite behavior. The YSU scheme overestimates (+1.2 m.s^{-1}) the observations in the first 2500 m height. The MYNN2.5 scheme produced the lowest U (= 0.3 m.s^{-1}) near-surface and the highest U (= 7 m.s^{-1}) above the PBL top. The QNSE scheme is closer to the observations near-surface and underestimates (-2.5 m.s^{-1}) above 1500 m height.

During the early morning on March 3, the PBLH$_{OBS}$ remained constant overnight with an average PBLH of 98 m (between 00:00 and 05:00 LT). The GBM, MRF, and MYJ schemes presented an average PBLH of 84 m. The average of PBLH$_{ERA5}$ is 87 m. Visually, the MYNN2.5 (PBLH = 274 m), MYNN3 (PBLH = 300 m), and QNSE (PBLH = 243 m) schemes overestimated the observations on average. The UW, SH, and YSU schemes produced the shallowest PBL with an average PBLH of 45 m. The evolution of the daytime PBL is better depicted using both nonlocal ACM2 and MRF schemes, as well as local MYNN2.5 and MYNN3 schemes between 08:00 and 10:00 LT. The maximum growth rate of 355 m.h^{-1} was observed between 09:00 and 10:00 LT. Divergences are seen amongst PBLH predictions from 10:00 LT. The maximum PBLH$_{OBS}$ is 1523 m at 14:00 LT, while the BouLac (PBLH = 1634 m), ACM2 (PBLH = 1704 m), and MYNN2.5 (PBLH = 1820 m) schemes overestimated it. The PBLH from ERA5 (= 1071 m) showed a really good agreement with the PBLH estimated from radiosonde sounding (PBLH$_{RS}$ = 1050 m). The GBM, YSU, UW, SH, and MYNN3 schemes underestimated (average PBLH = -52−665 m) the average PBLH$_{OBS}$ during the daytime. Most PBL schemes do not depict the complete PBL decaying in the afternoon and underestimate (average PBLH = -12−143 m) at night. The MYNN3 scheme overestimates (average PBLH = 429 m) at this time.

Figure 4.28 shows θ, q, and U vertical profiles at 02:00 and 14:00 LT on March 3. Almost all PBL schemes predicted θ profiles that are in general slightly colder (-1.0 K) than the observation at 02:00 LT. The UW scheme produced the coldest (-1.3 K) condition. The most significant differences are above the 2000 m height where all PBL schemes produced a colder (-0.8−1.2 K) condition, and in the first 1500 m height where the QNSE scheme showed a warmer (+0.6 K) bias. The predicted

Figure 4.28 - Vertical profiles of potential temperature (θ) in (a), vapor mixing ratio (q) in (b), and horizontal wind speed (U) in (c) on March 3, 2015. The radiosonde soundings time are indicated in y-axis label.

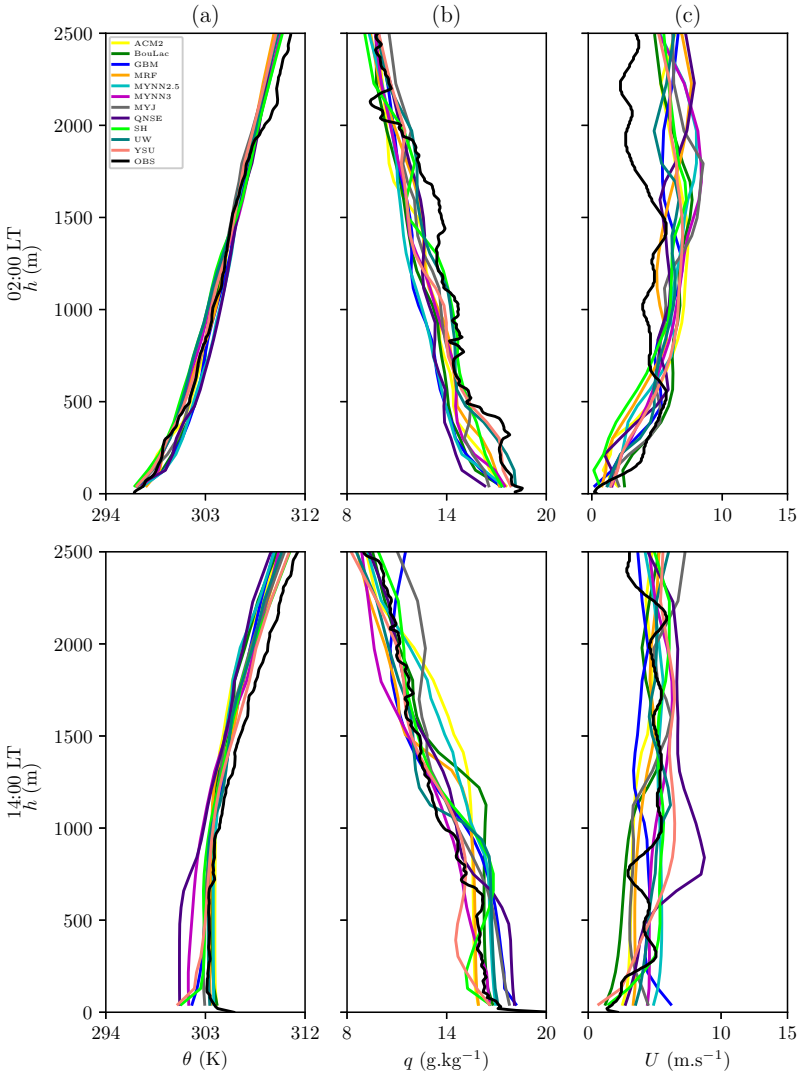

SOURCE: Author production.

q profiles revealed that all PBL schemes produced a drier (-0.5−1.0 g.kg^{-1}) environment in the first 2500 m height. The MYNN3 scheme produced the driest (-1.0 g.kg^{-1}) condition, while the UW scheme showed the wettest (+0.3 g.kg^{-1}) bias. All PBL schemes overestimated (+0.7−2.0 m.s^{-1}) the observed U profile, in which the BouLac (MRF) scheme produced the higher (lower) overestimation. All PBL schemes predicted a colder (-1.3−2.8 K) condition at 14:00 LT. Most of the PBL schemes showed nearly-neutral conditions, while the observed θ profile was unstable.

The QNSE scheme produced 3 K warmer and 1.3 g.kg^{-1} wetter conditions below 750 m height. The YSU scheme produced a drier (around -1.0 g.kg^{-1}) bias near-surface, however showed good agreement from $\approx$ 700 m height. The predicted U profiles among PBL schemes lies within the observations. The QNSE scheme overestimates (+1.6 m.s^{-1}) the observation, while the BouLac scheme underestimates (-1.0 m.s^{-1}) mainly in the first 1250 m height.

The average PBLH$_{OBS}$ was 247 m during the early morning on March 4 when the MYNN3 scheme depicted very well with an average PBLH of 283 m. The MYNN2.5 scheme also presented a good agreement, while other PBL schemes underestimated the observations. A decrease occurred in the PBLH$_{OBS}$ after sunrise, which is seen in the MYNN2.5 scheme prediction. The daytime PBL began to increase at 07:00 LT, where the YSU scheme presented a relatively good agreement until 11:00 LT. The maximum growth rate was 300 m.h^{-1} between 09:00 and 10:00 LT. The MRF, MYNN3, and QNSE schemes overestimated (average PBLH = -160−398 m) the PBLH$_{OBS}$ during the morning, and no PBL scheme depicted the maximum PBLH$_{OBS}$ (= 1105 m) at 14:00 LT. The GBM, UW, YSU, MYJ, SH, and MYNN2.5 schemes presented shallower PBL (PBLH = 110−530 m) during the afternoon. The QNSE scheme overestimated the observations with a PBLH of 1852 m at the noon, despite predicting only 790 m at the time of maximum PBLH$_{OBS}$. After the observed peak, PBLH$_{OBS}$ continuously decreased to 107 m at 20:00 LT. Both QNSE (+385 m) and MYNN3 (+34 m) schemes overestimated the observation during the afternoon. The PBLH estimated from ERA5 data overestimates (PBLH = 1370 m) the maximum PBLH$_{OBS}$. No PBL scheme showed a smooth PBLH shape, in which most of them presented double peaks or spikes (subsequently higher and lower PBLH). For instance, the GBM scheme showed a peak near 10:00 LT and produced shallower PBLH in the following hours.

Figure 4.29 presents θ, q, and U vertical profiles at 02:00 and 14:00 LT on March 4. All PBL schemes produced a slightly warmer (+0.5−1.0 K) bias below 500 m height and colder (-2.0−2.5 K) bias above the 2000 m height. In general, almost all PBL schemes produced a colder (-0.3−1.3 K) condition compared to observations while the MYNN3 scheme was 1.4 K colder. All PBL schemes produced wetter (+0.2−1.3 g.kg^{-1}) conditions in the first 2500 m height compared to observations. The MYNN3 scheme shows wetter (+1.5 g.kg^{-1}) conditions between the surface and 1300 m height, while the MYJ scheme produced a drier (-0.5 g.kg^{-1}) bias. All PBL schemes underestimate (-2.5−4.0 m.s^{-1}) the observed U profile, mainly in the first 1500 m height. The maximum observed U was 11.3 m.s^{-1} near 1200 m. A weakly

unstable θ profile is observed at 14:00 LT. The MYJ scheme depicts very well the observation in general, even being 1.5 K colder.

Figure 4.29 - Vertical profiles of potential temperature (θ) in (a), vapor mixing ratio (q) in (b), and horizontal wind speed (U) in (c) on March 4, 2015. The radiosonde soundings time are indicated in y-axis label.

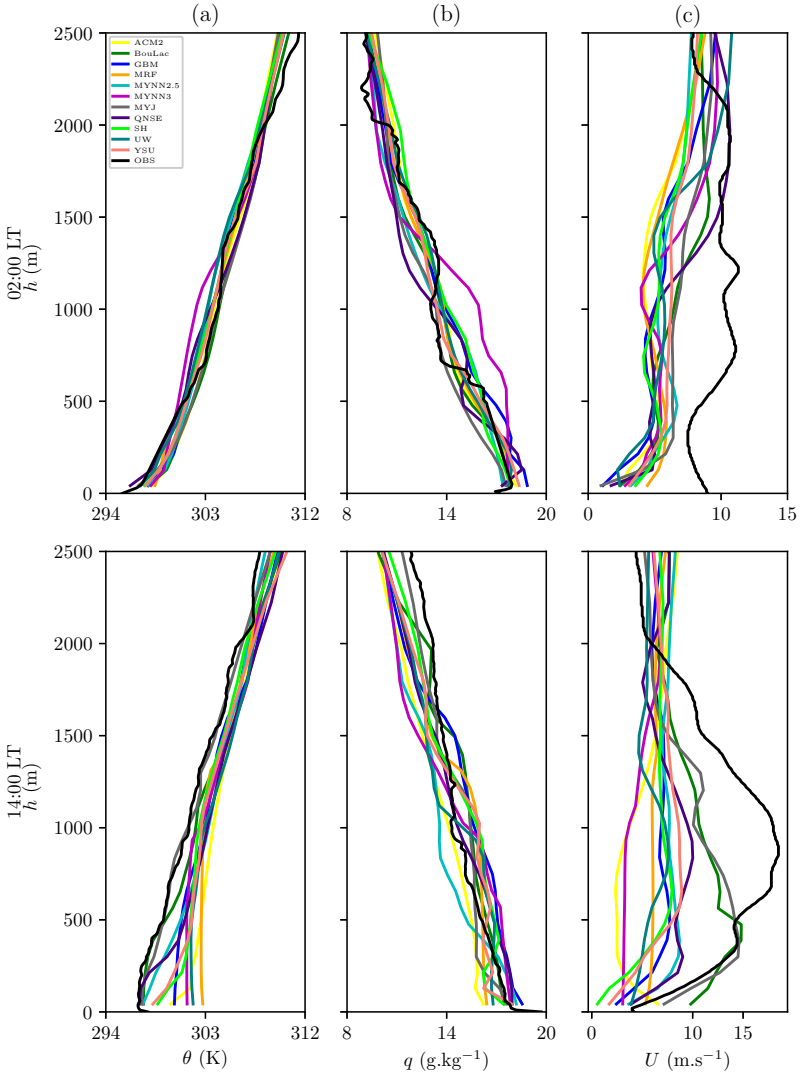

SOURCE: Author production.

The MYNN2.5 scheme presented a slightly colder (-0.3 K) bias. All other PBL schemes produced around 0.2−1.2 K warmer conditions and diverge in the stability definition amongst them. The ACM2 scheme presented the warmest (+1.2 K) bias. Both ACM2 and MYNN2.5 schemes were produced in general 0.6−0.7 g.kg^{-1} drier

conditions. The GBM scheme produced the wettest (+0.7 g.kg^{-1}) conditions. In the case of vertical wind speed structure, all PBL schemes underestimate (-1.1−6.7 m.s^{-1}) the observations. The predicted U profiles with both ACM2 and MYNN3 schemes showed a higher underestimation and greatly diverge from the other PBL schemes. Both MYJ and BouLac schemes showed good agreement in the first 500 m height. An upper LLJ is observed with the higher U of 18.5 m.s^{-1} near 860 m height.

Figure 4.30 shows the MAPE heatmap for PBLH at each hour on March 3 representing a complete day. The MAPE heatmap reveals that the GBM, MRF, and MYJ schemes presented the lowest error percentage (average MAPE of 11%) during the early morning. Both MYNN2.5 and MYNN3 schemes showed MAPE values above 150%.

Figure 4.30 - MAPE heatmap for predicted PBLH on March 3, 2015. MAPE for ERA5 data is also presented.

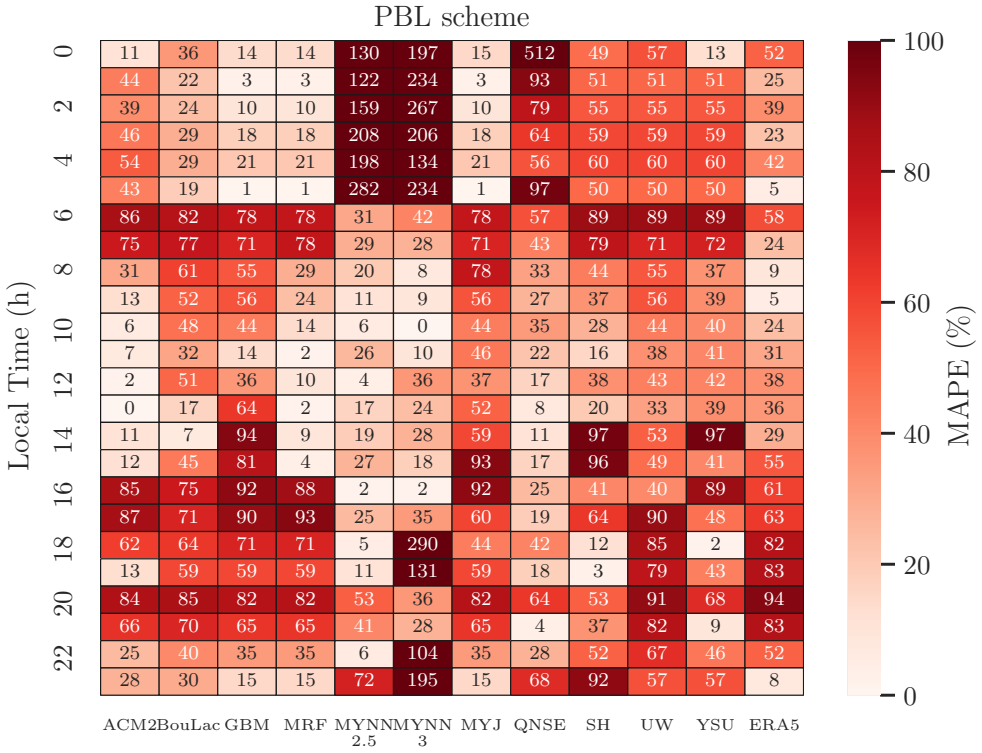

SOURCE: Author production.

The SH, UW, and YSU schemes presented MAPE around 55% at the same time. All PBL schemes showed high MAPE (up to 80%) near sunrise. During the transition from the morning to afternoon, both MYNN2.5 and MYNN3 schemes showed lower MAPE compared to other PBL schemes, with the MYNN3 scheme presenting 0% MAPE at 10:00 LT. The ACM2 scheme showed lower MAPE (< 15%) between 08:00 LT and 15:00 LT, and 0% MAPE at 13:00 LT. Higher MAPE arises during the transition from the late afternoon to nighttime. The MYNN2.5 scheme presented the lowest MAPE (on average 31%) during the nighttime, while the MYNN3 scheme presented the highest values. The PBLH from ERA5 presents higher MAPE values (an average of 130%).

Table 4.7 shows statistical indexes for PBLH during the daytime and nighttime. The average $PBLH_{OBS}$ was 803 m during the daytime and only the QNSE scheme overestimates (MB = 40 m) the observations. The MYNN3 scheme presented the lowest error (MB = -30 m, MAE = 271 m, RMSE = 356 m). The UW scheme showed the highest correlation coefficient (r = 0.62) compared to other PBL schemes, while the MYNN2.5 scheme presented the best IOA (= 0.76). The evaluated PBL schemes presented an average correlation coefficient of 0.42 and an average IOA of 0.62.

Table 4.7 - Statistical indexes for IOP3 PBL height in the daytime and nighttime.

	Average		**MB**		**MAE**		**RMSE**		**r**		**IOA**	
PBL scheme	Day	Night	Day	Night	Day	Night	Day	Night	Day	Night	Day	Night
ACM2	611	77	-193	-116	382	122	510	167	0.52	-0.2	0.71	0.44
BouLac	440	77	-364	-117	444	118	546	161	0.49	-0.12	0.63	0.46
GBM	260	85	-545	-109	560	109	689	153	0.23	0.21	0.48	0.47
MRF	616	85	-189	-109	373	109	490	153	0.56	**0.30**	0.72	0.47
MYNN2.5	695	246	-109	**53**	314	113	422	**139**	0.58	-0.08	**0.76**	0.34
MYNN3	774	280	**-30**	87	**271**	132	**356**	153	0.55	0.03	0.75	0.41
MYJ	349	85	-455	-109	498	**109**	625	153	0.21	0.06	0.49	0.47
QNSE	844	255	40	61	378	158	463	238	0.47	-0.26	0.68	0.10
SH	410	102	-394	-92	471	123	621	153	0.15	0.18	0.50	**0.50**
UW	342	42	-462	-151	463	151	559	186	**0.62**	0.12	0.60	0.45
YSU	393	80	-411	-113	478	133	604	169	0.23	0.07	0.51	0.46
ERA5	695	96	-110	-98	229	131	302	167	0.73	-0.07	0.84	0.42

SOURCE: Author production.

The PBLH from ERA5 presented both lower MAE (= 229 m) and RMSE (= 302 m), moreover showed a better correlation coefficient (r = 0.73) and IOA (= 0.84). During the nighttime, the average $PBLH_{OBS}$ was 193 m. The MYNN2.5 (MB = 53 m), MYNN3 (MB = 87 m), and QNSE (MB = 61 m) schemes overestimated the

$PBLH_{OBS}$. The MYNN2.5 scheme showed lower error (MB = 53 m, RMSE = 139 m). The GBM, MRF, and MYJ schemes presented the lowest MAE (= 109 m). The MRF scheme presented the best correlation coefficient (r = 0.30) and the SH scheme the best IOA (= 0.5). The best statistical indexes are spread among the evaluated PBL schemes, although the MRF scheme may be considered as the best performance based on these statistical metrics. In contrast to the daytime, the nighttime period showed poor statistical indexes with an average correlation coefficient of 0.02 and an average IOA of 0.41. The PBLH from ERA5 data presented a lower correlation coefficient (r = -0.07) and a relatively good IOA (= 0.42) in comparison to evaluated PBL schemes. Figure 4.31 shows Taylor diagrams for PBLH during the IOP3 in the daytime (a) and nighttime (b). The Taylor diagrams revealed how PBL schemes have a widespread performance in the PBLH forecasting, and that the ERA5 data outperforms the evaluated PBL schemes. The BouLac scheme presented a standard deviation closest to the observation, on the other hand, the UW scheme showed a lower CRMSE (≈ 300 m). Both nonlocal ACM2 and MRF schemes showed the highest standard deviation (σ = 542 m). Both nonlocal YSU and MRF schemes showed similar CRMSE (≈ 450 m).

Figure 4.31 - Taylor diagram for IOP3 PBL height on the daytime (a) and nighttime (b). Polar contours in grey are centered-root-mean-squared-error.

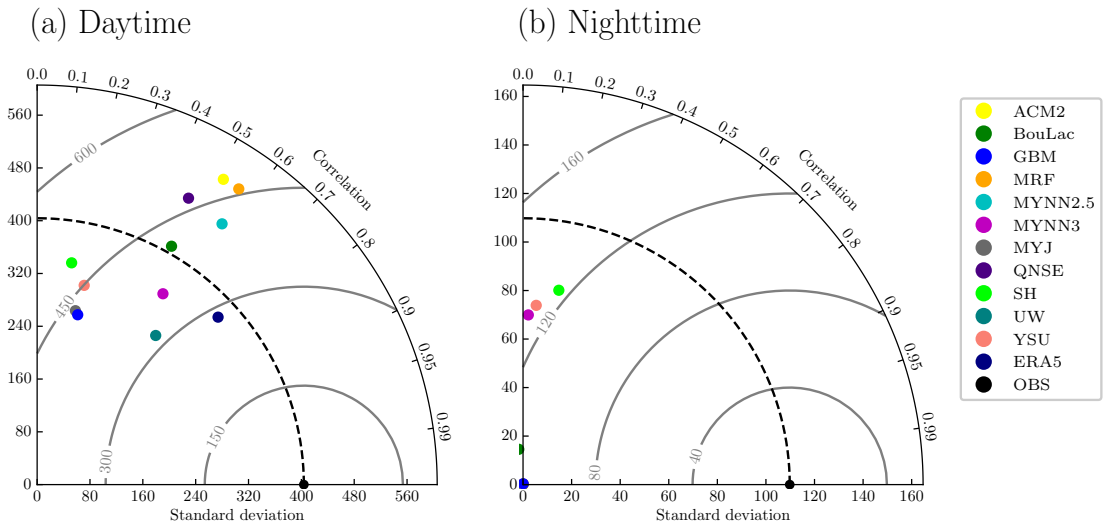

SOURCE: Author production.

During the nighttime, PBL schemes showed low performance with practically no

correlation among them. Some PBL schemes are not seen due to either higher standard deviation or negative correlation coefficient values. However, the nonlocal SH scheme may be considered as a less bad performance amongst PBL schemes.

Figure 4.32 shows the Taylor Skill scores (TSS) in a bar chart for both periods, which is useful to assist the definition of the best performance amongst evaluated PBL schemes, mainly during the nighttime. The TSS bar chart confirms that PBLH estimated from ERA5 data is better (TSS = 0.86) than the predicted amongst PBL schemes during the daytime.

Figure 4.32 - Taylor Skill score bar chart for IOP3 PBL height in the daytime (a) and nighttime (b).

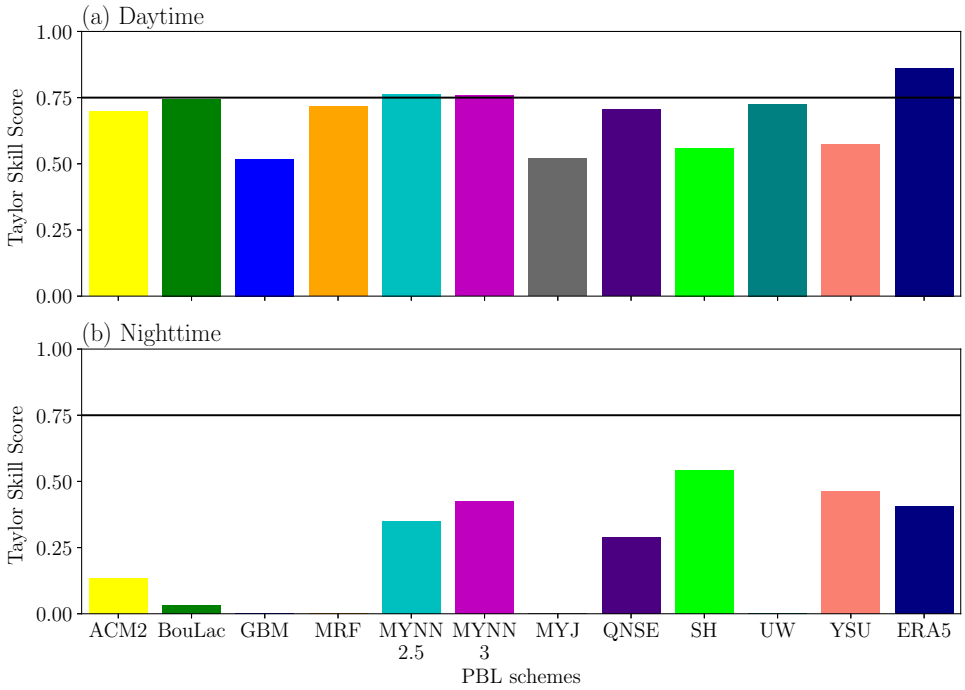

SOURCE: Author production.

The best performance amongst PBL schemes is produced with the local MYNN2.5 scheme (TSS = 0.76). Both local BouLac and MYNN3 schemes also presented a good performance (TSS $\approx$ 0.75). The worst TSS (= 0.52) is produced with both local GBM and MYJ schemes. During the nighttime, the TSS bar chart indicates the SH scheme (TSS = 0.54) as the best performance. The local GBM, MYJ, and

UW schemes and nonlocal MRF scheme showed TSS near zero. Although both local MYNN2.5 (TSS = 0.35) and MYNN3 (TSS = 0.42) schemes showed similar performance during the daytime, they presented different TSS at night.

Figure 4.33 shows PBLH for the inner domain (d03) at 02:00 LT on March 3. Non-local schemes (e.g., ACM2, MRF, SH, and YSU) reproduced the basin hydrography in their predicted PBLH contours. The MRF scheme (Figure 4.33d) showed a lower difference between overland (e.g., PBLH_{T3} = 85 m) and water bodies locations (e.g., PBLH_{Lake} = 187 m) compared to, for instance, the SH scheme (PBLH_{T3} = 43 m, PBLH_{Lake} = 224 m). The ACM2 scheme (Figure 4.33a) showed a generally higher PBLH over Manacapuru Lake. Both the local GBM (Figure 4.33c) and MYJ (Figure 4.33g) schemes presented a shallower PBL (PBLH ≈ 120 m) across the domain and do not reproduce the basin hydrography in their PBLH contours.

Figure 4.33 - Spatial field contoured with PBLH over the inner domain (d03) at 02:00 LT on March 3, 2015. PBL schemes are indicated in the panels.

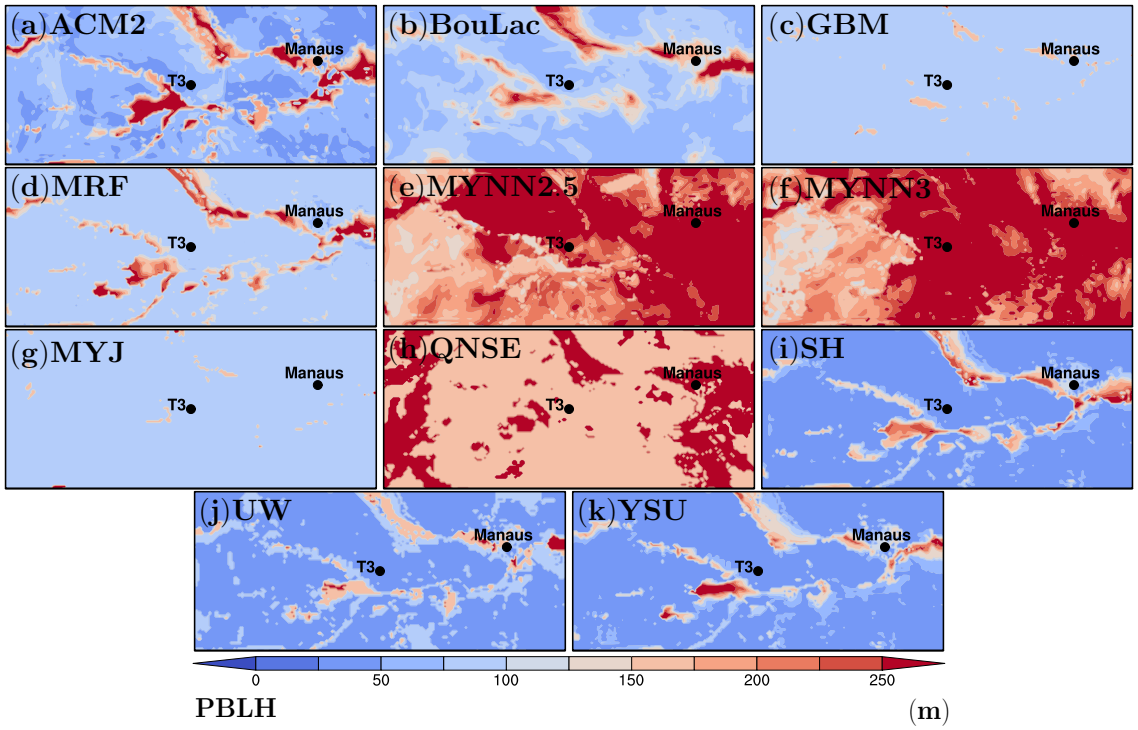

SOURCE: Author production.

Both local MYNN2.5 (Figure 4.33e) and MYNN3 (Figure 4.33f), and hybrid QNSE

(Figure 4.33h) schemes presented an overall higher PBLH (> 250 m) distribution in comparison to other PBL schemes. The average predicted PBLH among PBL schemes is 116 m for T3, 192 m for Manaus, 207 m for Negro River, and 210 m for Manacapuru Lake. The YSU scheme produced the highest PBLH (= 304 m) at Manacapuru Lake. The local UW scheme reproduced the basin hydrography in his PBLH distribution, differently from other local PBL schemes (e.g., GBM and MYJ). The local BouLac scheme also showed this behavior, although with a lesser detail.

Figure 4.34 shows PBLH for the inner domain (d03) at 14:00 LT on March 3. Non-local schemes reproduced the basin hydrography in their predicted PBLH contours as seen during the nighttime. The GBM ($PBLH_{T3}$ = 86 m), SH ($PBLH_{T3}$ = 43 m), and YSU ($PBLH_{T3}$ = 43 m) schemes showed lower PBLH over the T3 site.

Figure 4.34 - Spatial field contoured with PBLH over the inner domain (d03) at 14:00 LT on March 3, 2015. PBL schemes are indicated in the panels.

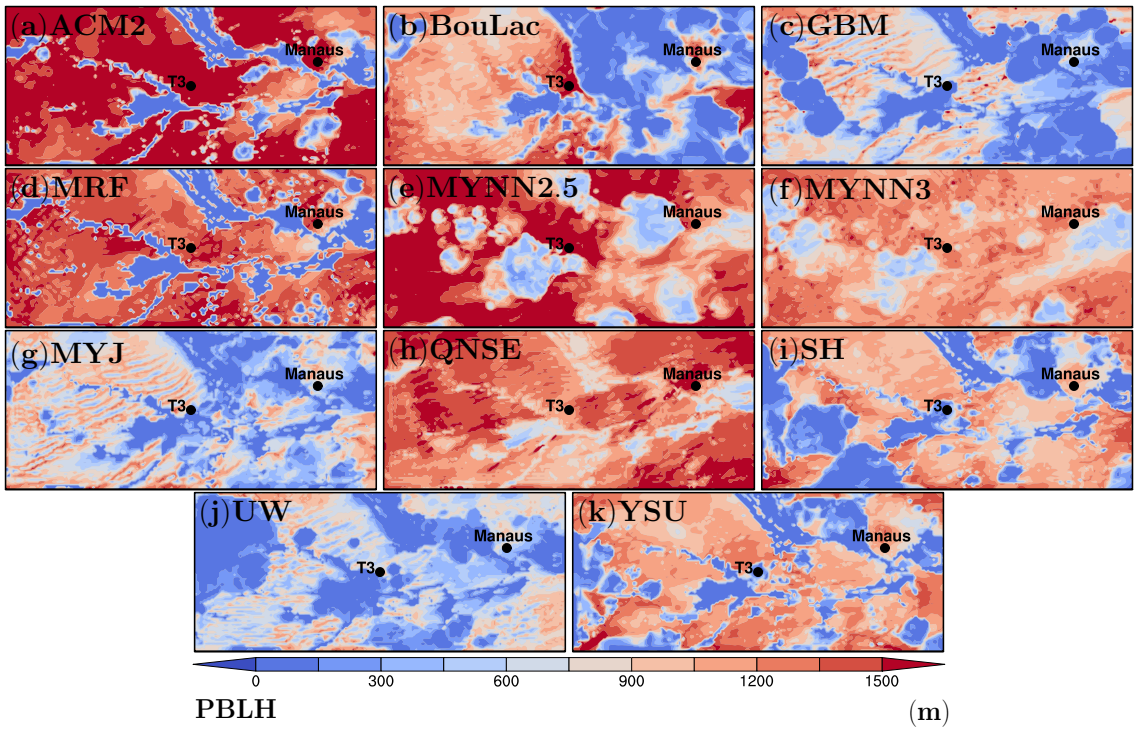

SOURCE: Author production.

The lower PBLH predicted with SH and YSU schemes is probably related to the predicted PCP at this time. Both local MYNN2.5 and MYNN3 schemes do not re-

produce the basin hydrography in their respective PBLH contours across the domain, which showed higher PBLH over the T3 site ($PBLH_{MYNN2.5}$ = 1820 m, $PBLH_{MYNN3}$ = 1090 m) and Manaus city ($PBLH_{MYNN2.5}$ = 1263 m, $PBLH_{MYNN3}$ = 1107 m). During the daytime, all PBL schemes predicted higher PBLH overland and lower PBLH over water bodies as seen in the previously studied periods. Nevertheless, the MYNN3 scheme predicted higher PBLH (= 1252 m) over Negro River compared to other PBL schemes. The average predicted PBLH among PBL schemes is 952 m for T3, 1113 m for Manaus, 317 m for Negro River, and 241 m for Manacapuru Lake. The local GBM, MYJ, and UW schemes showed streak patterns in the left-hand side of the domain, which are not viewed within other PBLH contours.

4.3.3 IOP3 synthesis

The statistical analysis of surface meteorological variables revealed that all PBL schemes produced relatively good T_2 forecasting, in which nonlocal schemes (e.g., ACM2, MRF, YSU) were slightly better. The local GBM scheme presents the best statistical indexes for RH_2 prediction and is indicated to the prediction of this variable. The local UW scheme showed good statistical indexes for U_{10}. Based on statistical indexes, the precipitation may be simulated with a less bad performance using the nonlocal YSU scheme.

The predicted PBL structures and PBLH daily cycle were also evaluated. All PBL schemes produced thermodynamic profiles during the nighttime, which are slightly closer to each other if compared to the daytime case (e.g., see Figure 4.28ab). The QNSE scheme produced warmer (colder) conditions at night (during the daytime) on the second day of the forecast. The MYJ scheme well reproduced the θ profile, showed a good agreement with the q profile, and depicted the U profile near-surface during the third day of the forecast. Nonlocal schemes showed warmer and drier conditions during the daytime compared to the rest of the PBL schemes. The evaluated PBL schemes showed different stability conditions through daytime θ profiles (e.g., see Figure 4.29a 14:00 LT).

The ERA5 reanalysis data produced a PBLH estimation that outperforms the evaluated PBL schemes for this period. The MYNN2.5 scheme produced the best performance, although the BouLac and MYNN3 schemes showed similar performance and also may be indicated to the prediction of the daytime PBL. Although both versions of local MYNN schemes showed good performance during the daytime, the nonlocal SH scheme is the best for the nighttime case. Despite this, MYNN schemes showed relatively good performance and perhaps could be employed to simulate the

PBL daily cycle. The nonlocal YSU scheme showed similar performance in both periods.

The PBLH spatial fields during the nighttime showed that GBM and MYJ (MYNN2.5, MYNN3, QNSE) schemes produced an (almost) homogeneous and shallower (deeper) PBLH distribution across the domain. The nonlocal ACM2, SH, and YSU schemes reproduced the basin hydrography in their PBLH distribution in contrast to most of the local schemes. In the daytime case, the ACM2 scheme showed higher PBLH overland. Both GBM and MYJ schemes produced streaks on the left side of the domain.

Figure 4.35 shows that independently of the PBL scheme all forecasts produced a homogeneous daily precipitation spatial field (< 2 mm) across the domain. At the same time, the estimate from MERGE data presents a different behavior with accumulated precipitation between 15-20 mm at the upper side of the domain. The PBL scheme may influence the precipitation presenting different results, however, it is not the case. Probably other physical packages such as microphysics and cumulus are influencing the precipitation distribution.

Figure 4.35 - Accumulated daily precipitation at 12:00 UTC on March 2, 2015. PBL schemes are indicated in the panels.

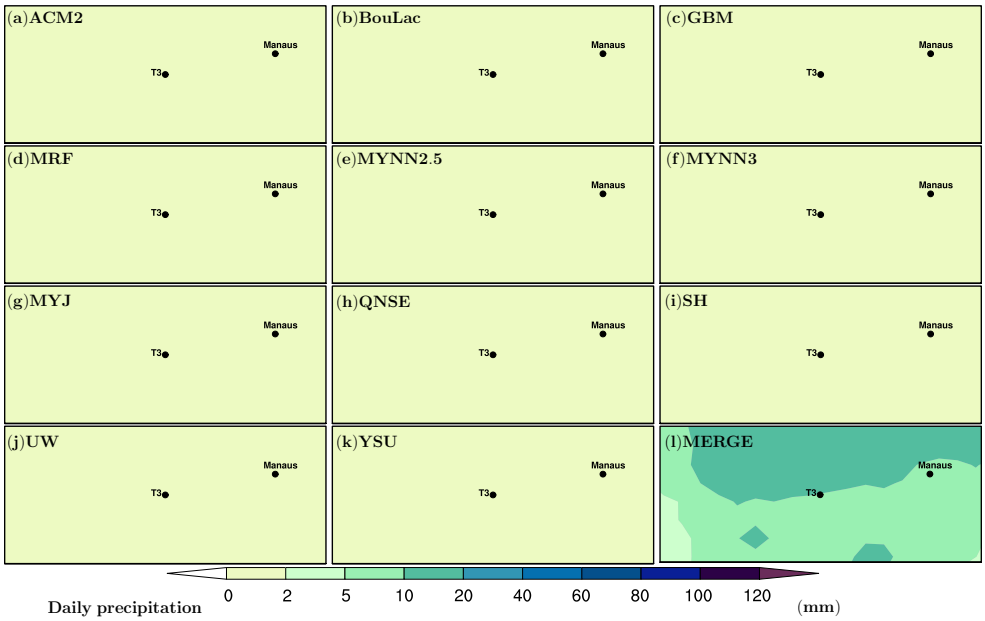

SOURCE: Author production.

In the case of the second day of comparison shown in Figure 4.36, PBL schemes presented differences in the daily precipitation among them. Most of the PBL schemes were unable to represent the observation in both Manaus and T3 site locations, which were either underestimate (e.g., ACM2) or overestimate (e.g., MYNN2.5). The higher amount of accumulated precipitation is located at the lower left-hand side of the domain in the MERGE data, apparently indicating that the precipitation moved from the upper part to the lower part of the domain between March 2 and 3. This behavior is not seen through the predictions, which show a "spread" rainfall distribution.

Figure 4.36 - Accumulated daily precipitation at 12:00 UTC on March 3, 2015. PBL schemes are indicated in the panels.

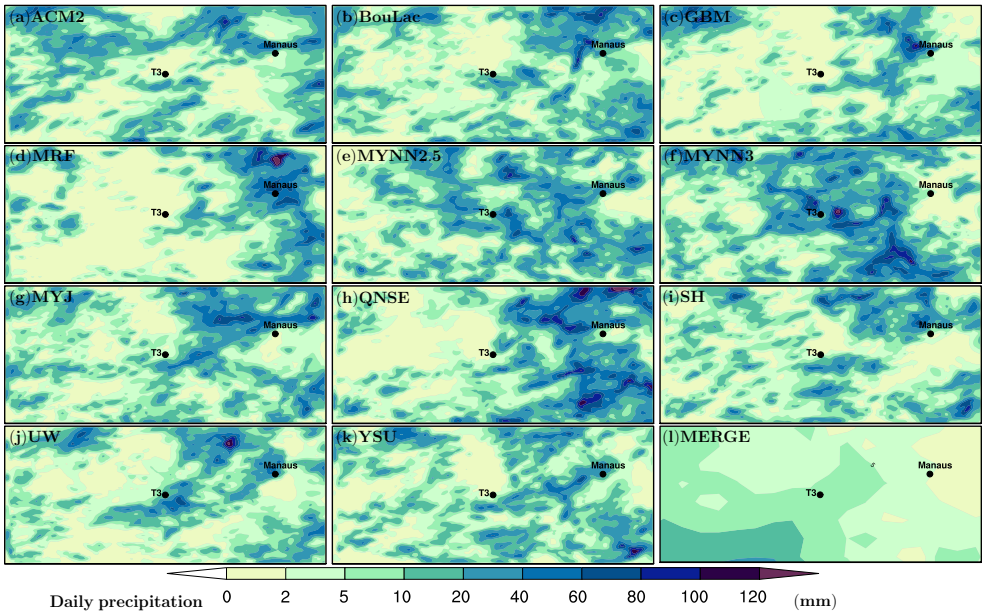

SOURCE: Author production.

Figure 4.37 shows the third day of comparison, which the MERGE data reveals both Manaus and T3 locations presenting daily precipitation of 2 mm. Nonlocal schemes such as ACM2, MRF, YSU, and SH schemes showed agreement with MERGE data over T3, however, showed a higher amount of precipitation over Manaus. Almost all PBL schemes were unable to match with MERGE data in both locations. The higher amount of observed precipitation is located on the left-hand side in the upper part of the domain with some PBL schemes, for instance, ACM2, GBM, and MYNN3 schemes also showing it. Both MRF and QNSE showed lesser agreement with this

behavior. Apparently, the precipitation system circulated within the central Amazon basin during this 60-h period. The model showed difficulties to represent the general pattern of the precipitation distribution, which certainly lead to impacts on surface meteorological variables and consequently the predicted PBLH.

Figure 4.37 - Accumulated daily precipitation at 12:00 UTC on March 4, 2015. PBL schemes are indicated in the panels.

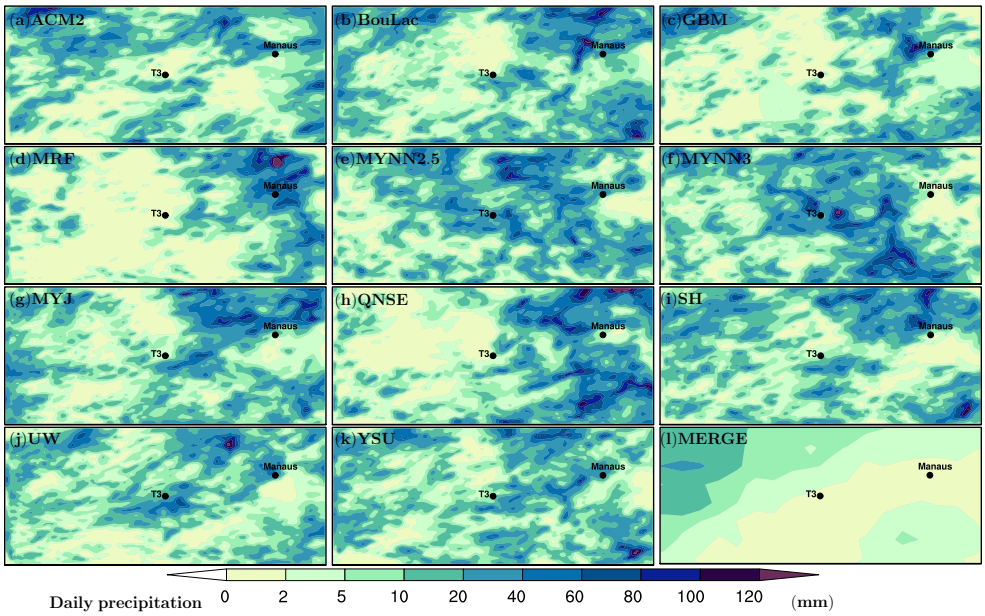

SOURCE: Author production.

4.4 IOP4 (2015 dry season)

4.4.1 Meteorological variables

Figure 4.38 shows the predicted meteorological variables from all the eleven inter-comparison experiments and corresponding observations. The daily cycle of observed T_2 shows the usual daily cycle pattern; with maximum temperatures during the afternoon and minimum temperatures near sunrise during the nighttime cooling. All tested PBL schemes presented the daily cycle shape, although underestimates (-1.3−2.7 °C) the observations along the period. The MYNN2.5 (UW) scheme produced the warmest (coldest) conditions during the daytime compared to other PBL schemes.

Whilst, the MYJ (MYNN3) scheme produced the warmest (coldest) conditions com-

Figure 4.38 - Time series of predicted 2-m air temperature (a), 2-m relative humidity (b), 10-m horizontal wind speed (c), and precipitation (d) for IOP4.

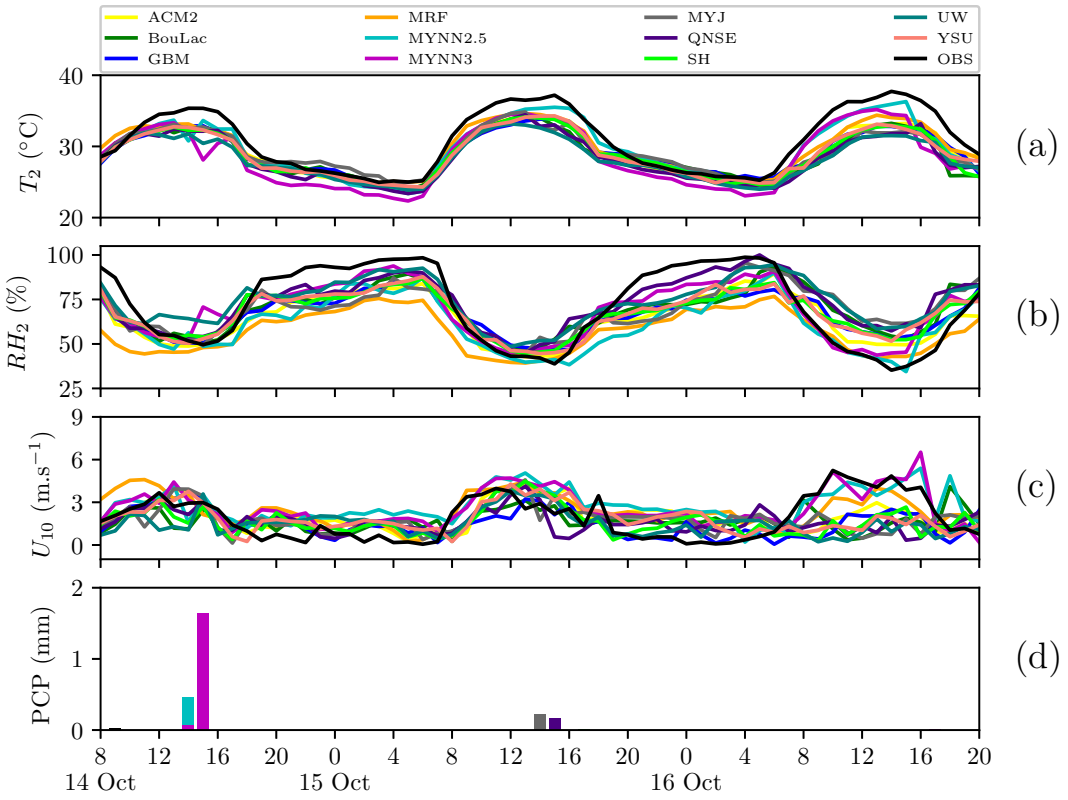

SOURCE: Author production.

pared to observations and other PBL schemes at night. The maximum observed T_2 was 37.7 °C at 14:00 LT on March 4, which the evaluated PBL schemes were unable to depict presenting 1.7−6.2 °C colder conditions. Most of the PBL schemes (e.g., YSU and SH schemes) depict the heating rates during the morning, as well as the nocturnal cooling. In the case of RH_2 predictions, the usual daily cycle is relatively well depicted with values closer to the nighttime saturation and drying during the daytime. All PBL schemes presented this behavior, however, they do not depict completely the saturation with differences between 10 % and 20 %. Some PBL schemes (e.g., nonlocal YSU and SH schemes or local MYNN2.5/3 schemes) better follow this behavior during the daytime. Most of the PBL schemes predicted 3−11 % wetter (8−25 % drier) conditions in comparison with observations during the daytime (nighttime), mainly on October 16. The nonlocal MRF scheme produced the driest (2−5% at daytime and 5−25% at night) conditions in both periods. The local

UW scheme produced 10−20% wetter conditions during the daytime. However, both MYNN3 and QNSE schemes produced wetter conditions at night, i.e. presented the minor differences (8−15% drier).

Almost all PBL schemes overestimated (+0.5−1.5 m.s^{-1}) the observed U_{10} during the nighttime. In the daytime case, some PBL schemes (e.g., MYNN2.5 and MYNN3 schemes) overestimate, and other PBL schemes (e.g., GBM and UW) underestimate. Both MYNN2.5 and MYNN3 schemes (UW and MYJ) presented the highest (lowest) wind speeds during the period. The increase of air wind speed during the convection initiation (between 07:00 and 10:00 LT) seen in both October 15 and 16 is relatively depicted by most of the PBL schemes. In the latter referred day, both MYNN schemes showed good agreement with the observed U_{10} increase during the CBL development stage. No rainfall is observed during the period. However, both local MYNN2.5 and MYNN3 schemes predicted a non-observed rain (lesser than 2 mm) between 14:00 and 15:00 LT on October 14. Another non-observed rain (lesser than 1 mm) was produced at the same period on October 15, using both the local MYJ scheme and the hybrid QNSE scheme.

Table 4.8 summarizes the statistical indexes computed for meteorological variables over the 60-h analysis period. The average observed T_2 is 31.0 °. Statistical indexes indicate that all PBL schemes underestimated as expected. The MYNN2.5 scheme presented the best indexes (= -1.2 °C, MAE = 1.3 °C, RMSE = 1.7 °C, IOA = 0.96). The MRF scheme showed the best correlation coefficient (r = 0.97), while the UW scheme produced the highest difference (MB = -2.6 °C, MAE = 2.6 °C, RMSE = 3.2 °C). The average observed RH_2 is 71 % and statistical indexes revealed the MYNN3 scheme as the best showing lower error (MAE = 8 %, RMSE = 9 %) and the best performance indicators (r = IOA = 0.92). The QNSE scheme presented the lowest MB (= 1 %), which is the only PBL scheme that overestimates the observed RH_2. The MRF scheme presents the worst statistical indexes with higher MB (= -14 %). The average observed U_{10} is 1.8 m.s^{-1}. The ACM2 (MB = 0.1 m.s^{-1}), MRF (MB = 0.6 m.s^{-1}), MYNN2.5 (MB = 0.8 m.s^{-1}), and MYNN3 (MB = 0.7 m.s^{-1}) schemes overestimated the observations. The ACM2 scheme showed the lowest MB. The MYNN3 scheme performed the best statistical indexes (MAE = 1.0 m.s^{-1}, RMSE = 1.2 m.s^{-1}, r = 0.76, IOA = 0.81), while BouLac scheme showed the worst performance indicators (r = 0.09, IOA = 0.40). No rainfall is observed during the period, thus all PCP statistical indexes are equal to zero.

Table 4.8 - Statistical indexes for IOP4 meteorological variables computed over the 60-h analysis period.

Variable	**Statistical index**	**PBL scheme**										
		ACM2	BouLac	GBM	MRF	MYNN2.5	MYNN3	MYJ	QNSE	SH	UW	YSU
T_2	AVG	29.1	28.9	29.2	29.7	29.7	28.6	29.2	28.4	28.9	28.3	29.0
	MB	-1.8	-2.0	-1.8	**-1.2**	**-1.2**	-2.3	-1.7	-2.5	-2.0	-2.6	-1.9
	MAE	1.9	2.1	1.9	1.4	**1.3**	2.4	2.1	2.5	2.1	2.6	2.0
	RMSE	2.2	2.7	2.4	1.8	**1.7**	2.7	2.7	3.0	2.5	3.2	2.4
	r	**0.97**	0.92	0.96	**0.97**	0.96	0.94	0.90	0.94	0.96	0.94	**0.97**
	IOA	0.92	0.87	0.89	0.94	**0.96**	0.90	0.86	0.85	0.89	0.82	0.90
RH_2	AVG	64	68	66	56	61	68	69	73	67	73	67
	MB	-7	-2	-4	-14	-10	-2	-2	**1**	-4	2	-4
	MAE	10	11	11	15	11	**8**	13	9	11	11	10
	RMSE	12	13	13	18	14	**9**	15	11	12	13	12
	r	0.91	0.81	0.89	0.91	0.91	**0.92**	0.70	0.85	0.90	0.83	0.89
	IOA	0.87	0.83	0.83	0.75	0.85	**0.92**	0.76	0.88	0.84	0.84	0.86
U_{10}	AVG	2.0	1.7	1.5	2.4	2.7	2.6	1.8	1.6	1.6	1.5	1.8
	MB	**0.1**	-0.2	-0.4	0.6	0.8	0.7	-0.1	-0.3	-0.3	-0.4	-0.1
	MAE	1.1	1.3	**1.0**	1.1	1.2	**1.0**	1.3	1.3	1.1	1.3	1.2
	RMSE	1.4	1.6	1.4	1.3	1.4	**1.2**	1.6	1.6	1.5	1.7	1.5
	r	0.46	0.09	0.51	0.63	0.67	**0.76**	0.18	0.20	0.35	0.14	0.34
	IOA	0.64	0.40	0.66	0.73	0.74	**0.81**	0.47	0.49	0.58	0.47	0.57
PCP	AVG	0.0	0.0	0.0	0.0	0.0	0.0	0.0	0.0	0.0	0.0	0.0
	MB	0.0	0.0	0.0	0.0	0.0	0.0	0.0	0.0	0.0	0.0	0.0
	MAE	0.0	0.0	0.0	0.0	0.0	0.0	0.0	0.0	0.0	0.0	0.0
	RMSE	0.0	0.0	0.0	0.0	0.0	0.0	0.0	0.0	0.0	0.0	0.0

* AVG is the average.

SOURCE: Author production.

4.4.2 Turbulent fluxes

Figure 4.39 shows the predicted turbulent fluxes from the eleven intercomparison experiments and corresponding observations. The turbulent heat fluxes time series (Figure 4.39ab) showed that the available net radiation (daytime conditions) is predominantly partitioned in H accordingly to observations. The average H is 74.0 W.m^{-2} with maximum values around 250.0 W.m^{-2}, while the average LE is 60.0 W.m^{-2} with maximum values around 150.0 W.m^{-2}. All PBL schemes showed a better agreement with observations for both H and LE during the nighttime than daytime.

Figure 4.39 - Time series of predicted sensible heat flux (a), latent heat flux (b), Bowen Ratio (c), and momentum flux (d) for IOP4.

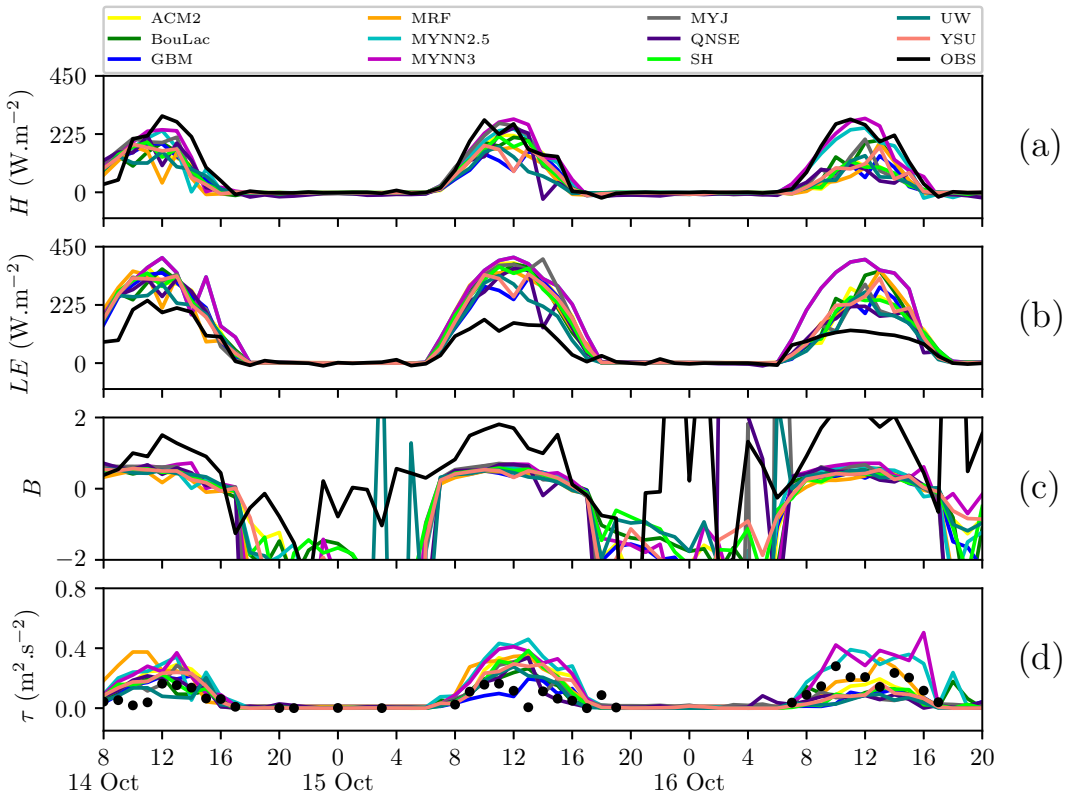

SOURCE: Author production.

In the H case, PBL schemes showed the observed diurnal cycle shape. All PBL

schemes relatively well depicted the H during the convection initiation, while most of them anticipate the increase of LE. Both MYNN2.5 and MYNN3 schemes presented a better agreement (mainly on October 16) with observed H when compared to other PBL schemes which underestimated the observations. All PBL schemes overestimated the observed LE showing higher values (more than 200 %) than the observations during the daytime. The MYNN3 (UW) scheme showed higher (lower) LE. The Bowen ratio indicates a poor agreement amongst predictions and observations. All PBL schemes produced a closer Bowen ratio at night in comparison amongst them. This period has more momentum flux (τ) observations compared to IOP2. Most of the PBL schemes overestimated (+0.1-0.3 $m^2.s^{-2}$) the observed τ during the daytime through the first two days. Both MYNN2.5 and MYNN3 (GBM and UW) schemes presented the highest (lowest) τ values. During the transition from nighttime on October 14 to the early morning on next day (October 15), all PBL schemes showed good agreement with the observations.

Table 4.9 presents the statistical indexes computed for turbulent heat fluxes over the 60-h analysis period. All PBL schemes underestimated H with the MYNN3 scheme showing the best statistical indexes (MB = -1.3 $W.m^{-2}$, MAE = 21.1 $W.m^{-2}$, RMSE = 34.8 $W.m^{-2}$, r = 0.94, IOA = 0.97). The UW scheme presented the highest error (MB = -38.9 $W.m^{-2}$, MAE = 45.7 $W.m^{-2}$, RMSE = 73.8 $W.m^{-2}$) compared to other PBL schemes. On the other hand, the UW scheme presented the best statistical indexes for LE (MB = 31.9 $W.m^{-2}$, MAE = 37.8 $W.m^{-2}$, RMSE = 62.9 $W.m^{-2}$, IOA = 0.88). The GBM scheme presented the best correlation coefficient (r = 0.93). The performance indexes indicated that PBL schemes depicted both turbulent heat fluxes with the relatively same quality. During the nighttime, both predicted turbulent heat fluxes presents a good agreement with observations. The average correlation coefficient for H was 0.86, while for LE was 0.91. In the case of IOA, the average IOA for H was 0.86 and for LE was 0.80.

Table 4.9 - Statistical indexes for IOP4 turbulent fluxes computed over the 60-h analysis period.

Variable	**Statistical index**	**PBL scheme**										
		ACM2	BouLac	GBM	MRF	MYNN2.5	MYNN3	MYJ	QNSE	SH	UW	YSU
H	AVG	43.9	48.7	38.9	35.6	62.1	72.9	50.6	40	43.8	35.4	42.7
	MB	-30.3	-25.6	-35.4	-38.6	-12.2	**-1.3**	-23.6	-34.2	-30.4	-38.9	-31.5
	MAE	37.8	33.7	41.4	43.4	22.1	**21.1**	35.3	44.0	38.6	45.7	38.5
	RMSE	65.3	55.8	70.7	74.7	40.6	**34.8**	58.2	72.1	65.7	73.8	66.8
	r	0.85	0.90	0.85	0.81	0.93	**0.94**	0.86	0.79	0.85	0.87	0.85
	IOA	0.85	0.90	0.81	0.80	0.96	**0.97**	0.90	0.83	0.85	0.79	0.84
LE	AVG	113.3	112.9	104.3	113	142.1	142.1	11.4	100.5	109.2	91.8	109.2
	MB	53.4	53.1	44.4	53.2	82.3	82.3	51.5	40.7	49.4	**31.9**	49.4
	MAE	58.6	57.9	49.7	58.3	84.8	84.8	56.6	46.0	54	**37.8**	54.1
	RMSE	91.7	93.4	76.5	91.6	128.1	128.1	91.9	73.0	83.9	**62.9**	83.7
	r	0.92	0.91	**0.93**	0.90	0.90	0.90	0.91	0.92	**0.93**	0.92	**0.93**
	IOA	0.81	0.80	0.85	0.80	0.71	0.71	0.80	0.85	0.83	**0.88**	0.83

* AVG is the average.

SOURCE: Author production.

4.4.3 PBL diurnal cycle and structure

Figure 4.40 presents obtained results for PBLH predictions and corresponding observations. A shallow PBL ($PBLH_{OBS}$ = 158 m) is observed at 08:00 LT on October 14. The GBM scheme predicted the closest PBLH (= 172 m) to the observed. The $PBLH_{OBS}$ increased with an average growth rate of 280 $m.h^{-1}$. Some PBL schemes presented a relatively good agreement during the morning until began to diverge (e.g., UW scheme at 11:00 LT). The maximum $PBLH_{OBS}$ was 1838 m at 14:00 LT. The QNSE scheme presented the best agreement (PBLH = 1716 m) at the observed peak time, although not shown the diurnal shape. The PBLH from ERA5 data overestimates the daytime $PBLH_{OBS}$. The QNSE, MYNN2.5, and MYNN3 schemes overestimated (+82−528 m) the observations during the transition from the late afternoon to nighttime. After the observed peak, the $PBLH_{OBS}$ decreased to 120 m at midnight. The average $PBLH_{OBS}$ was 232 m during the nighttime. The SH, UW, and YSU schemes produced the shallowest PBL with an average PBLH of 44 m, while the QNSE scheme overestimates presenting an average PBLH of 1174 m. The PBLH from ERA5 data underestimates with an average PBLH of 138 m.

Figure 4.40 - IOP4 planetary boundary layer height.

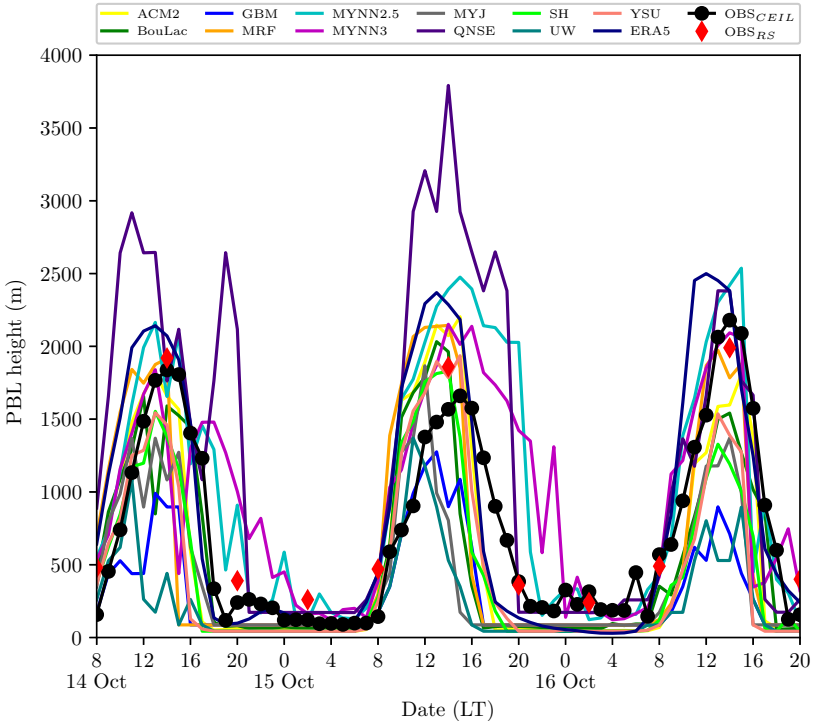

SOURCE: Author production.

Figure 4.41 shows θ, q, and U vertical profiles predicted for all PBL schemes and corresponding radiosonde soundings at 08:00 and 14:00 LT on October 14. All PBL schemes produced warmer (+1.0−1.3 K) and drier (-1.4−2.1 g.kg^{-1}) conditions in the first 2500 m height at 08:00 LT.

Figure 4.41 - Vertical profiles of potential temperature (θ) in (a), vapor mixing ratio (q) in (b), and horizontal wind speed (U) in (c) on October 14, 2015. The radiosonde soundings time are indicated in y-axis label.

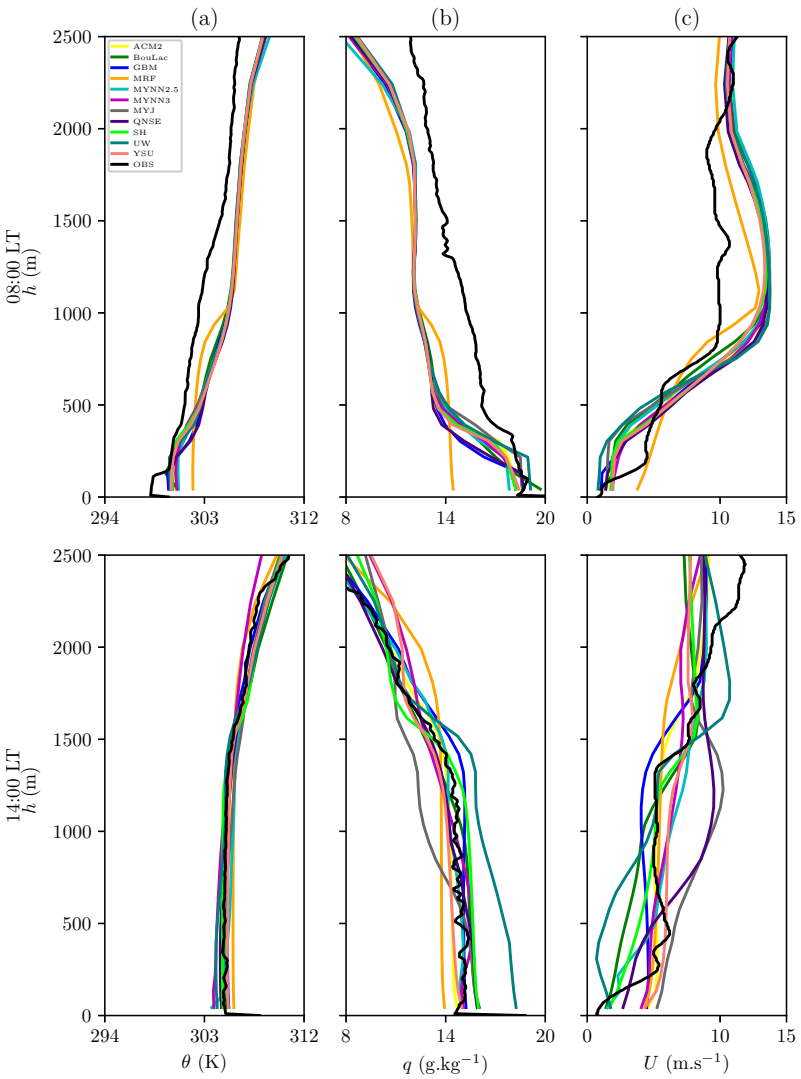

SOURCE: Author production.

The MRF (BouLac) scheme showed the warmest (coldest) conditions, while the UW (MRF) scheme produced the wettest (driest) conditions amongst evaluated

PBL schemes. Furthermore, the MRF scheme diverges from all other PBL schemes below the 1000 m height (which presents a similar shape) showing the warmest and driest conditions near-surface. The evaluated PBL schemes underestimate (-1.1−2.3 $m.s^{-1}$) the observed U profile below $\approx$ 300 m height, except the MRF scheme which overestimates (+1.0 $m.s^{-1}$). On the other hand, the MRF scheme slightly underestimates (-0.8 $m.s^{-1}$) above 2000 m height. In general, all PBL schemes overestimate (+0.5−1.1 $m.s^{-1}$) the observed U profile. After the CBL development during the morning, near-neutral profiles are seen at 14:00 LT. In the case of θ profile, all PBL schemes showed good agreement with observation. The QNSE, YSU, and SH schemes showed good agreement within PBL and were slightly warmer near the PBL top. The MRF (UW and MYNN3) scheme produced 0.8 K warmer (0.4−0.6 K colder) conditions in the first 1000 m height, while the MYNN3 scheme produced the coldest (-1.0 K) conditions from $\approx$ 1600 m height. The QNSE scheme showed a good agreement with the observed q profile. The MRF scheme showed the driest (-1.2 $g.kg^{-1}$) condition in the first 750 m height, while the UW scheme presents a wetter (2.0 $g.kg^{-1}$) bias in the first 1500 m height. The MYJ scheme produced around 1.8 $g.kg^{-1}$ drier condition in the middle of PBL (between 750 and 1500 m height). The observed U profile showed wind speed closer to 0.0 $m.s^{-1}$ near-surface and closer to 10.0 $m.s^{-1}$ near the PBL top. The UW scheme presents lower U near-surface and higher U above the PBL top in comparison with other PBL schemes. Both QNSE and MYJ schemes produced higher U ($\approx$ 10.0 $m.s^{-1}$) in the middle of PBL.

A nocturnal SBL is observed during the early morning with an average $PBLH_{OBS}$ of 107 m on October 15. The YSU (MYNN3) scheme predicted the shallowest (deepest) SBL with an average PBLH of 45 m (220 m). The PBLH from ERA5 is closer to the observations with an average PBLH of 117 m. The observed PBL heights (around 100 m) began to increase after sunrise. The maximum growth rate of 473 $m.h^{-1}$ was observed between 11:00 and 12:00 LT. The maximum $PBLH_{OBS}$ was 1660 m at 15:00 LT. All PBL schemes no depicted the observed daytime shape showing no consistency in time and depth. Apparently, most of the PBL schemes anticipate in $\approx$ 1-h their peak and overestimates the observation. The $PBLH_{OBS}$ began to decay from 16:00 LT, while nonlocal MRF, YSU, and ACM2 schemes were decreasing one hour earlier. The daytime PBL decaying occurred until 23:00 LT, when $PBLH_{OBS}$ was 182 m. The QNSE scheme showed good agreement with observation between 21:00 and 23:00 LT. The QNSE, MYNN2.5, and MYNN3 schemes overestimated (+637−827 m) the observed PBLH, while the other PBL schemes underestimated (-410−622 m) during the transition from the late afternoon to nighttime. The UW

scheme showed the shallowest PBLH with an average of 48 m. The PBLH from ERA5 overestimated (+596 m) the observations between the morning and early afternoon.

Figure 4.42 shows θ, q, and U vertical profiles predicted for all PBL schemes and corresponding radiosonde soundings at 02:00 and 14:00 LT on October 15. A quite stable θ profile is observed at 02:00 LT.

Figure 4.42 - Vertical profiles of potential temperature (θ) in (a), vapor mixing ratio (q) in (b), and horizontal wind speed (U) in (c) on October 15, 2015. The radiosonde soundings time are indicated in y-axis label.

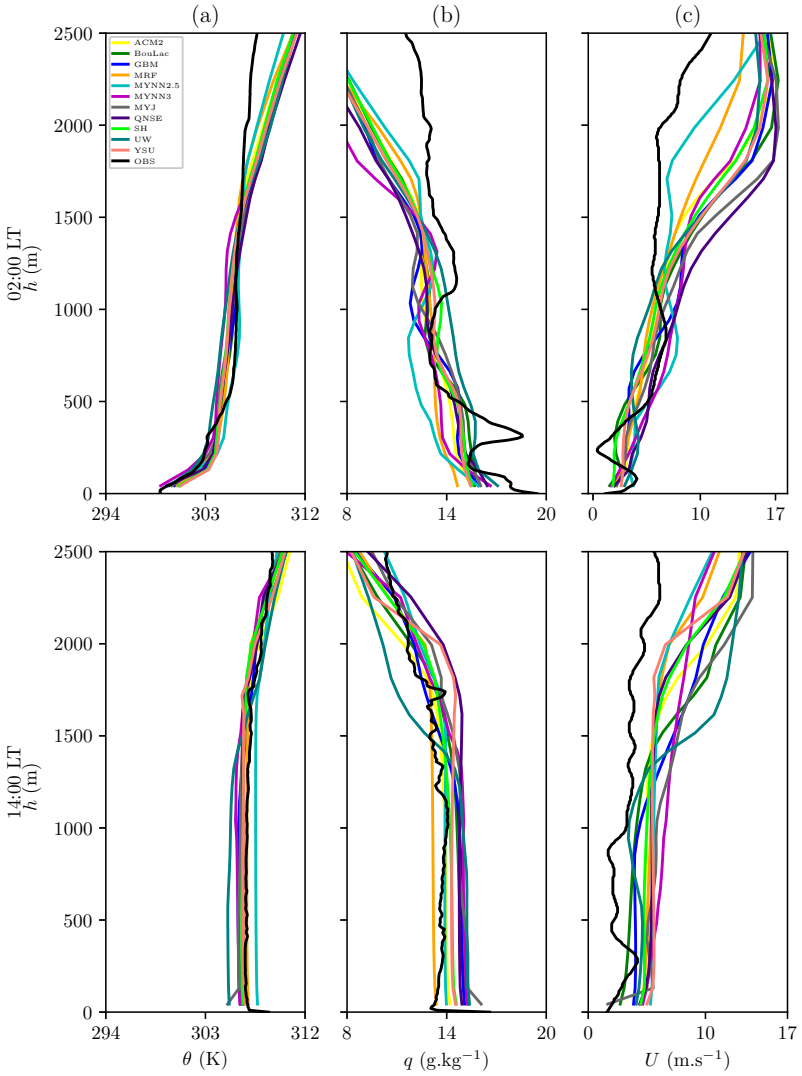

SOURCE: Author production.

A significant increase in θ is seen from 240 m height, which is approximately the same height where an inversion is seen in q profile (began to drying upwards) and coincides with the upper part of the LLJ observed in the U profile. The LLJ nose is around 90 m with 4.0 m.s^{-1}. All PBL schemes do not depict both the slight increase observed in θ profile near 240 m height as the inversion in q profile, showing smooth profiles. In general, almost all PBL schemes produced 0.2−0.8 K warmer conditions in both near-surface and 0.7−1.7 K warmer above 1500 m height. The MYNN2.5 showed good agreement with observations between 500 and 1250 m height. No PBL scheme depicts the observed LLJ and produces a higher overestimation (+5.0−10 m.s^{-1}) above 1000 m height with higher U, near 17.0 m.s^{-1}. A well-mixed θ profile is observed at 14:00 LT. The nonlocal schemes (e.g., MRF, YSU, ACM2, and SH) produced the closest θ profiles within the PBL in comparison with local schemes which showed either a warmer bias as the MYNN2.5 scheme (+0.8 K) or a colder bias as the UW scheme (-1.3 K). Despite the UW scheme showing the coldest conditions within the PBL, above the PBL top it was 0.4 K warmer than observations. The MRF scheme presents the driest (-0.5 g.kg^{-1}) conditions below 1500 m height, while all other PBL schemes produce 0.2−1.2 g.kg^{-1} wetter conditions. Above the 1500 m height, the UW scheme produced a 1.2 g.kg^{-1} drier bias. The QNSE scheme showed in general 1.5 g.kg^{-1} wetter conditions. The MYNN2.5 scheme is the only one that produced wetter conditions than observations near 2500 m height, while the ACM2 scheme is the driest. All PBL schemes overestimated (+7.0-10.0 m.s^{-1}) the observed U profile showing higher wind speeds ($>$ 10 m.s^{-1}) above 1500 m height while the observations remained nearly constant around 4.5 m.s^{-1}. The MYJ scheme produced the highest U ($\approx$ 14.0 m.s^{-1}) near 2500 m height.

The observed PBL was less stable compared to the previous days during the early morning presenting an average of 239 m on October 16. The YSU, SH, and UW schemes predicted a shallower PBL at this period with an average PBLH of around 43 m. The MYNN2.5 scheme presented the deepest PBL with an average PBLH of 208 m. After three hours of constant height, the PBLH$_{OBS}$ increased from 186 m at 05:00 LT to 446 m at 06:00 LT. No PBL scheme depicted this observed growth rate near sunrise. The PBLH$_{OBS}$ decreased to 146 m at 07:00 LT and began to increase from this time onward. Both QNSE and MYNN2.5 schemes overestimated the PBLH$_{OBS}$ during the daytime. The MYNN3 scheme underestimated the PBLH$_{OBS}$, despite being closer to daytime shape. The maximum PBLH$_{OBS}$ was 2180 m at 14:00 LT. The MYNN3 scheme predicted the closer PBLH (= 2092 m) to the observations. Both GBM (PBLH = 712 m) and UW (PBLH = 529 m) schemes presented the shallower PBL, while both MYNN2.5 (PBLH = 2420 m) and QNSE (PBLH =

2184 m) schemes a deeper PBL. The PBLH from ERA5 data overestimated (around 350 m) the observation and is not in phase with $PBLH_{OBS}$ shape. The MYNN2.5, MYNN3, and QNSE schemes are closer to $PBLH_{OBS}$ decaying during the afternoon. The MYNN3 scheme presented higher PBLH ($>$ 500 m) in the late afternoon.

Figure 4.43 shows vertical profiles of θ, q, and U vertical profiles predicted for all PBL schemes and corresponding radiosonde soundings at 02:00 and 14:00 LT on October 16. A stable θ profile is observed at 02:00 LT evolving from 299 K at the surface and remaining practically constant around 306 K until near 2500 m height. All PBL schemes produced 0.1−2.3 K colder conditions below 2000 m height. The UW scheme produces the coldest conditions, while the MYNN2.5 scheme is closer to observations. On the other hand, all PBL schemes are 0.4−1.2 K warmer above the 1700 m height. In regard to q profiles, the evaluated PBL schemes diverge amongst them presenting either a wetter or drier bias in the first 1500 m, mainly near-surface. The nonlocal MRF scheme presents a 1.1 g.kg^{-1} drier bias, while the local UW scheme is 0.9 g.kg^{-1} wetter than observations below 1700 m height. All PBL schemes produced 1.7−4.9 g.kg^{-1} drier conditions above 2000 m height. The evaluated PBL schemes predicted U profiles that diverge amongst them. The MYNN2.5 (MRF) scheme presents good agreement near-surface (near 2500 m height) and underestimates (overestimates near-surface) near 2500 m height. Almost all PBL schemes underestimated (-0.5−1.5 m.s^{-1}) the observed U profile below 1250 m height, except the MRF, MYNN2.5, MYNN3 schemes which overestimated (around 0.5 m.s^{-1}) the observations. Most of the PBL schemes overestimated (+1.4−2.7 m.s^{-1}) the observed wind speeds above 2000 m height presenting higher U (around 12.0−13.0 m.s^{-1}). A weakly unstable θ profile is observed at 14:00 LT. Only the MYNN2.5 scheme produces 0.6 K warmer bias in the first 1500 m height, while the MYNN3 scheme presenting 1.8 K colder than the observations above 1500 m height. The rest of the PBL schemes are 0.9−2.6 K colder than the observations below 1500 m height. Most of the PBL schemes are 0.4−3.2 g.kg^{-1} wetter than observations in the first 1000 m height, while the MRF scheme showed good agreement (0.1 g.kg^{-1} drier). No PBL scheme depicts the inversion near 1500 m height. All PBL schemes predicted 1.2−3.0 g.kg^{-1} wetter conditions than the observations above 2000 m height. The MYJ (MYNN3) scheme predicted the wetter (around 4.0 g.kg^{-1}) conditions near-surface (above PBL top). All PBL schemes underestimated (-1.0−3.7 m.s^{-1}) the observed U profile in general, however, some PBL schemes presented higher U in different portions of the PBL as the MYNN3 scheme in the first 500 m height (U = 6.5 m.s^{-1}) or the ACM2 scheme above 2000 m height (U = 18.0 m.s^{-1}). Both MRF and MYNN2.5 schemes predicted similar U profiles.

Figure 4.43 - Vertical profiles of potential temperature (θ) in (a), vapor mixing ratio (q) in (b), and horizontal wind speed (U) in (c) on October 16, 2015. The radiosonde soundings time are indicated in y-axis label.

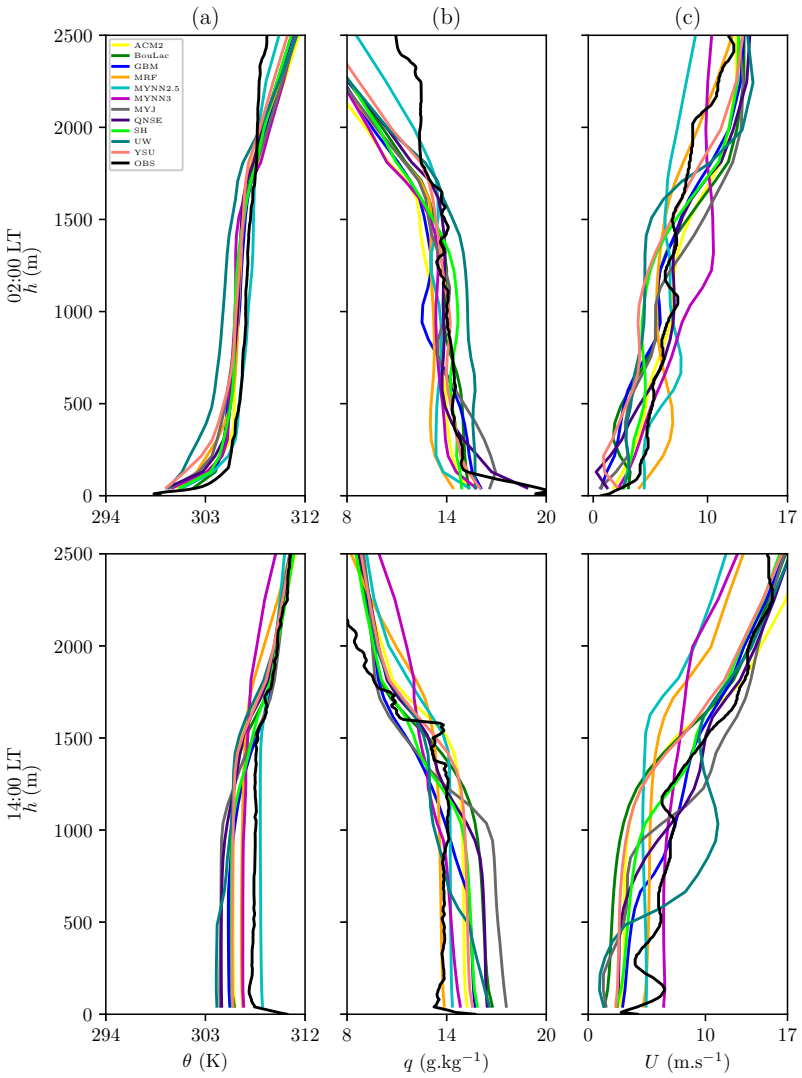

SOURCE: Author production.

Figure 4.44 shows the MAPE heatmap for PBLH at each hour on October 15. Both MYNN2.5 and MYNN3 schemes presented higher MAPE during the early morning, for instance, 277−391 % at 00:00 LT. Visually, the ERA5 data presented the best performance during this period including 0 % MAPE at 03:00 LT. The ACM2, SH, UW, and YSU schemes showed MAPE values near 60 %. The GBM, MRF, and MYJ showed lower MAPE (< 30 %) during the same period. Some PBL schemes began to present higher MAPE from the sunrise. Both SH and YSU schemes presented 0

% MAPE at 09:00 LT, while the MRF scheme presents MAPE equal to 135 %. The QNSE scheme showed higher MAPE (> 97 %) compared to other PBL schemes during the afternoon. All PBL schemes presented higher MAPE from 17:00 LT. Both MYNN2.5 and MYNN3 schemes presented the highest MAPE values at night, for instance, the MYNN3 scheme presented 527 % at 21:00 LT. The QNSE scheme presents lower MAPE values during the nighttime with 4 % at midnight. The PBLH from ERA5 presented higher MAPE too (> 60 %).

Figure 4.44 - MAPE heatmap for predicted PBLH on October 15, 2015. MAPE for ERA5 data is also presented.

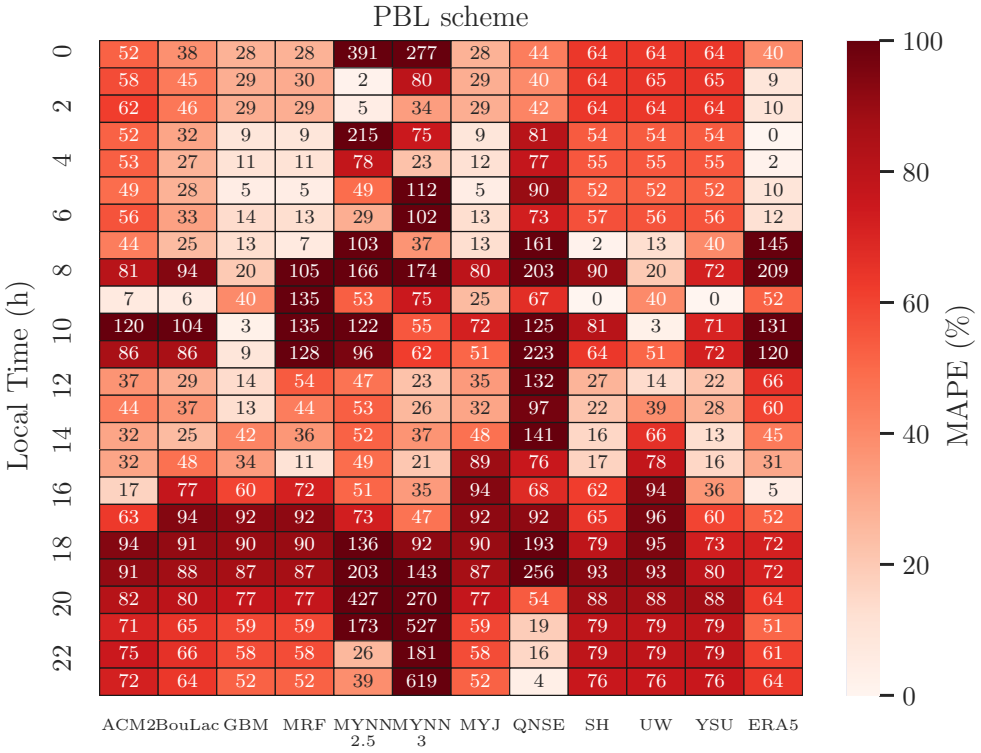

SOURCE: Author production.

Table 4.10 summarizes the statistical indexes for PBLH during both daytime and nighttime. The average $PBLH_{OBS}$ during the daytime was 1119 m. The UW scheme presented the highest MB (= -723 m). The ACM2 scheme showed both the lowest MB (= -70 m) and RMSE (= 508 m) and the best IOA (= 0.84). The MYNN3 scheme presented the lowest MAE (= 394 m). The MYNN2.5 scheme performed

the best correlation coefficient (r = 0.81). The evaluated PBL schemes presented an average correlation coefficient of 0.75 and an average IOA of 0.80. The UW scheme presented both the lowest correlation coefficient (r = 0.28) and IOA (= 0.51). The average $PBLH_{OBS}$ was 216 m at night. The MYNN2.5 (MB = 191 m), MYNN3 (MB = 337 m), and QNSE (MB = 221 m) schemes overestimated the nocturnal $PBLH_{OBS}$. The GBM scheme showed lowest error (MB = -130 m, MAE = 130 m, RMSE = 181 m). The YSU scheme showed the best correlation coefficient (r = 0.73), while the SH scheme presented a negative correlation (r = -0.14). The MYNN2.5 scheme showed the best IOA (= 0.46). The average correlation coefficient is 0.37 and the average IOA is 0.39. The PBLH estimated from ERA5 data no outperforms any of the evaluated PBL schemes.

Table 4.10 - Statistical indexes for IOP4 PBL height on daytime and nighttime.

	Average		**MB**		**MAE**		**RMSE**		**r**		**IOA**	
PBL scheme	Day	Night	Day	Night	Day	Night	Day	Night	Day	Night	Day	Night
ACM2	1012	51	**-107**	-165	428	165	**508**	207	0.74	0.29	**0.84**	0.41
BouLac	928	71	-191	-145	447	145	544	191	0.64	0.41	0.78	0.42
GBM	484	86	-635	**-130**	643	**130**	793	**182**	0.6	0.44	0.6	0.41
MRF	1024	86	-95	-130	601	130	736	182	0.51	0.35	0.71	0.41
MYNN2.5	1490	407	370	191	477	247	574	469	**0.81**	0.67	0.82	**0.46**
MYNN3	1280	553	161	337	**395**	394	510	552	0.69	0.43	0.82	0.32
MYJ	672	86	-447	-130	597	130	712	182	0.51	0.29	0.64	0.41
QNSE	1797	438	678	221	786	302	1028	708	0.60	0.35	0.61	0.25
SH	799	46	-320	-170	482	170	578	214	0.66	-0.14	0.75	0.39
UW	396	43	-723	-173	762	173	939	215	0.28	0.26	0.51	0.40
YSU	810	47	-309	-169	486	169	598	205	0.65	**0.73**	0.76	0.42
ERA5	1406	111	287	-104	492	132	587	181	0.77	-0.05	0.82	0.35

SOURCE: Author production.

Figure 4.45 shows the Taylor diagrams for PBLH during the IOP4 period in the daytime (a) and nighttime (b). The PBL schemes showed a widespread performance during the daytime, with the BouLac scheme prediction (σ = 616 m) closest to the observed standard deviation (σ = 603 m). Despite the MYNN2.5 scheme showing a higher σ (= 750 m), it presents the lowest CRMSE ($\approx$ 450 m) and the best correlation coefficient (r = 0.81). The YSU, MYNN3, and BouLac schemes showed relatively similar performance. The QNSE scheme is not seen in the Taylor diagram plot due to the highest σ (= 979 m). The Taylor diagram reveals how clustered are the performance amongst PBL schemes at night. The reference σ is 130 m. Most of the PBL schemes are not seen in the Taylor diagram plot due to their standard deviation close to zero. The YSU scheme shows σ equal to 17.3 m and a correlation

coefficient of 0.73, the QNSE scheme presents a standard deviation of 720 m and a correlation coefficient of 0.35. The GBM, ACM2, BouLac, and YSU schemes showed similar performance.

Figure 4.45 - Taylor diagram for IOP4 PBL height on daytime (a), and nighttime (b). Polar contours in grey are centered-root-mean-squared-error.

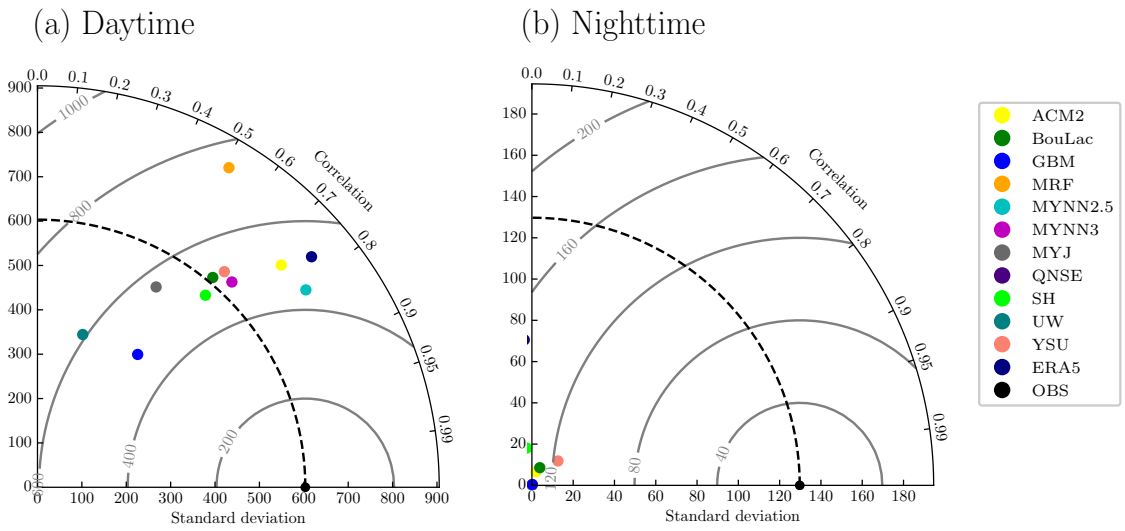

SOURCE: Author production.

Figure 4.46 shows the Taylor Skill scores (TSS) in a bar chart for both periods, which provides a useful way to indicate the best or some of the best performances. The ACM2, BouLac, MYNN2.5, MYNN3, SH, and YSU schemes performed TSS higher than 0.80. The MYNN2.5 scheme presents the best TSS (= 0.86) in comparison with other PBL schemes during the daytime. On the other hand, the UW scheme showed a lower TSS (= 0.50). The ACM2, BouLac, GBM, MRF, MYJ, and UW schemes showed poor performance with TSS closer to zero during the nighttime. Both MYNN2.5 and MYNN3 schemes were the best TSS at night, and the MYNN2.5 scheme (TSS = 0.19) is slightly better than the MYNN3 scheme (TSS = 0.18). The TSS revealed that PBLH estimated from ERA5 outperforms the evaluated PBL schemes presenting a TSS equal to 0.33 at night.

Figure 4.47 shows PBLH for the inner domain (d03) at 02:00 LT on October 15. Both the MRF scheme (Figure 4.47d) and UW scheme (Figure 4.47j) show opposite behavior. Whilst the MRF scheme showed higher PBLH overland ($PBLH_{T3}$ = 85 m)

Figure 4.46 - Taylor Skill score bar chart for IOP4 PBL height in the daytime (a) and nighttime (b).

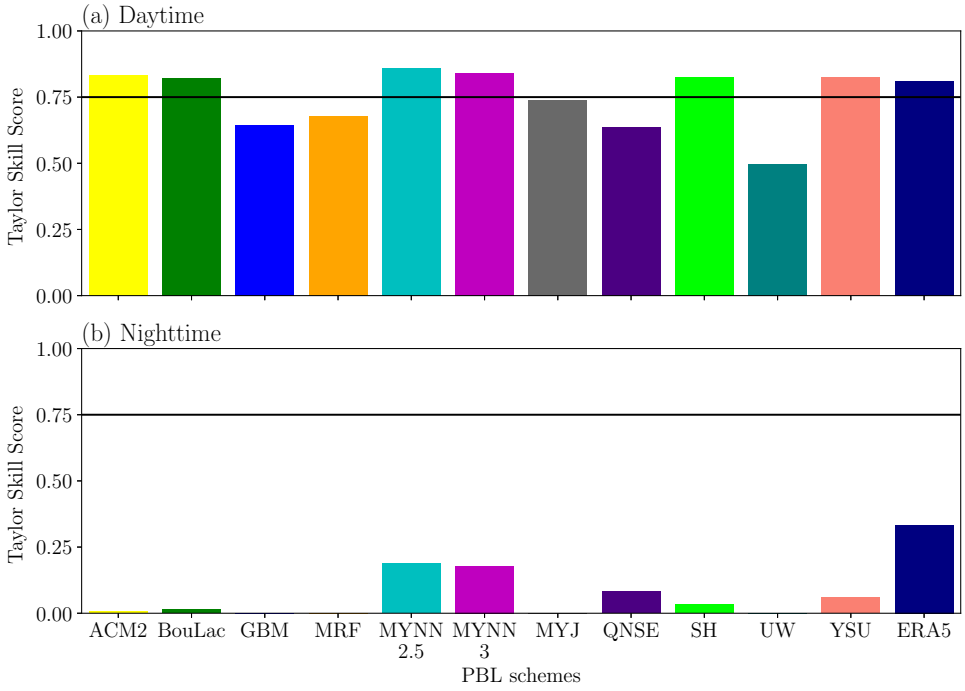

SOURCE: Author production.

and lower over the river ($PBLH_{River}$ = 49 m), the UW scheme showed lower PBLH overland ($PBLH_{T3}$ = 43 m) and higher PBLH over the river ($PBLH_{River}$ = 85 m). The GBM scheme (Figure 4.47c) and MYJ scheme (Figure 4.47g) showed a homogeneous PBLH distribution ($\approx$ 85 m). The ACM2 scheme (Figure 4.47a) reproduced the less river-influenced PBLH distribution amongst nonlocal PBL schemes. The average predicted PBLH among PBL schemes is 86 m for T3, 101 m for Manaus, 101 m for Negro River, and 91 m for Manacapuru Lake at night. The MYNN2.5 (Figure 4.47e), MYNN3 (Figure 4.47f), and QNSE (Figure 4.47h) schemes produced the deepest PBL with no river influence.

Figure 4.48 shows PBLH for the inner domain (d03) at 14:00 LT on October 15. Both MYNN2.5 and MYNN3 schemes predicted a homogeneous and higher PBLH distribution across the domain, with higher PBLH ($>$ 1500 m) over rivers/water bodies. Nonlocal schemes (e.g., ACM2, MRF, SH, YSU) reproduced the basin hydrography in their respective PBLH contours. The GBM scheme (Figure 4.48c) and

Figure 4.47 - Spatial field contoured with PBLH over the inner domain (d03) at 02:00 LT on October 15, 2015. PBL schemes are indicated in the panels.

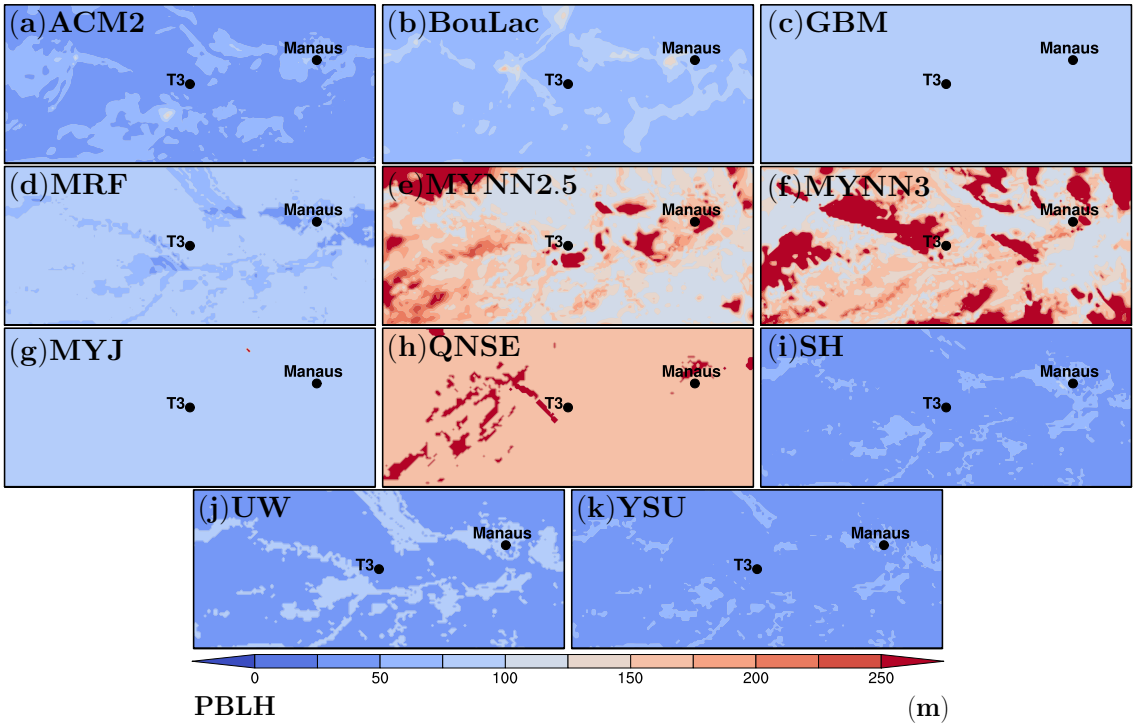

SOURCE: Author production.

UW scheme (Figure 4.48j) produced lower PBLH in comparison with other PBL schemes. The GBM, MYJ, and UW schemes showed streaks over the domain, i.e. regions of higher and lower PBLH interleaved. As seen in previously studied periods, during the daytime all PBL schemes produced higher PBLH overland and lower over water bodies. The average predicted PBLH among PBL schemes is 1851 m for T3, 1741 m for Manaus, 701 m for Negro River, and 400 m for Manacapuru Lake during the daytime. The QNSE scheme produced the deepest PBL across the domain.

4.4.4 IOP4 synthesis

The statistical analysis of the surface meteorological variables shows that all PBL schemes predicted reasonably the observed T_2. The MYNN2.5 scheme presents the best performance amongst the evaluated PBL schemes. The MYNN3 scheme performed both the best RH_2 and U_{10} predictions in comparison with other PBL schemes. No precipitation was observed during the period, however MYNN2.5, MYNN3, MYJ, and QNSE schemes predicted a non-observed rainfall.

Figure 4.48 - Spatial field contoured with PBLH over the inner domain (d03) at 14:00 LT on October 15, 2015. PBL schemes are indicated in the panels.

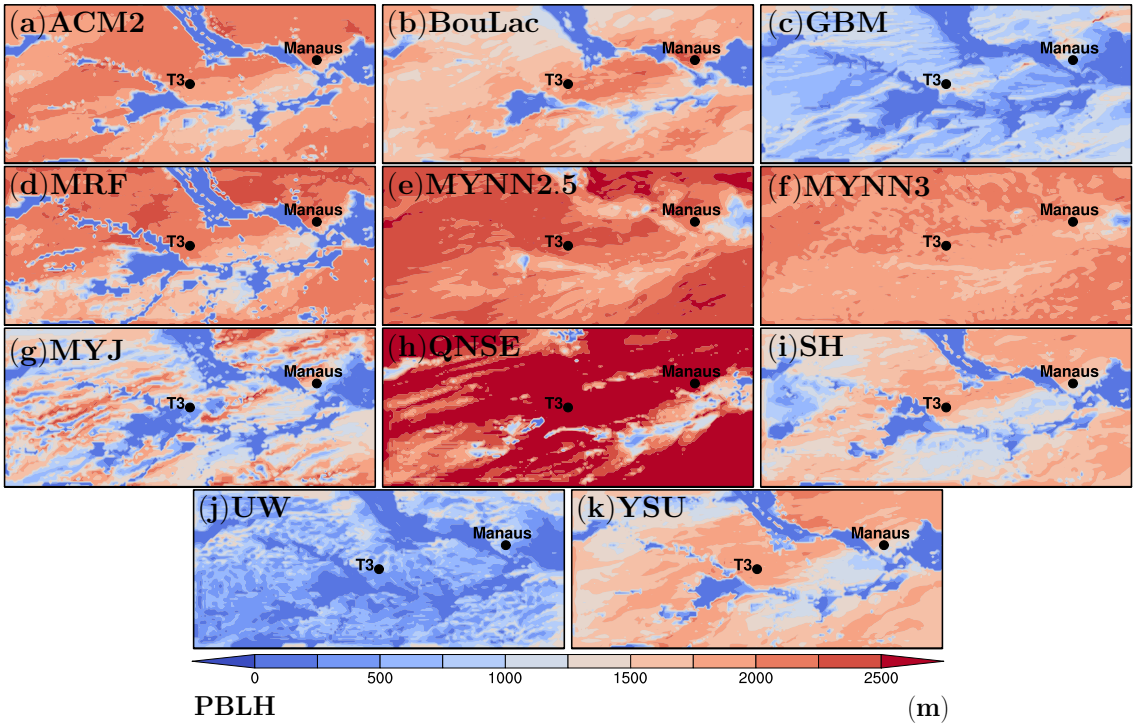

SOURCE: Author production.

The evaluated PBL schemes better predicted thermodynamic profiles during the daytime compared to the nighttime profiles (e.g., see Figure 4.42). The observed θ profile is better predicted than both q and U profiles. For this period, the observed θ profile may be considered better predicted on the second day of forecast. On the other hand, the SBL profiles are better depicted on the third day of the forecast. The observed U profile is the less good predicted in comparison with thermodynamic structures, with the predictions showing a better agreement from the second day of forecast. Nonlocal PBL schemes presented a better agreement in the prediction of the well-developed CBL during the afternoon than nighttime SBL, which is better predicted by local PBL schemes.

The statistical indexes computed for PBLH showed that the best indexes are spread amongst the evaluated PBL schemes in both periods (see Table 4.10), which makes it difficult to indicate the best performing PBL scheme. However, the local MYNN2.5 and nonlocal ACM2 schemes showed the best performance indicators for the day-

time. The MYNN2.5 and YSU schemes presented the best performance indicators for nighttime. The MAPE heatmap (Figure 4.44) revealed how PBL schemes produced higher error across the day, with the GBM, MRF, and MYJ schemes producing the lower MAPE values during the early morning. In the transition from afternoon to nighttime, higher MAPE values are seen. Both the Taylor diagrams (Figure 4.45) and Taylor Skill Score bar chart (Figure 4.46) assist in the indication of the best PBL scheme to PBLH prediction. The Taylor diagram for the daytime indicates both the local BouLac and nonlocal SH schemes as the best choice, while the Taylor Skill Score revealed the MYNN2.5 scheme as the best. For the night case, in which the Taylor diagram indicates that all PBL schemes produced a poor performance. The TSS reveals both the local MYNN2.5 and MYNN3 schemes as the best performance with the MYNN2.5 scheme being slightly better.

The PBLH spatial fields for nighttime showed that during the studied IOP4, all PBL schemes showed a relatively shallower PBL with nonlocal schemes being more river-influenced than local schemes. The MYNN2.5, MYNN3, and QNSE schemes showed the higher PBLH as seen in previous periods (IOP1, IOP2, IOP3). Both local GBM and MYJ schemes produced a homogeneous and shallower PBLH distribution, while the local UW scheme presents the basin hydrography in its predicted PBLH contours. In contrast to nighttime, almost all local PBL schemes presented PBLH contours that are influenced by the water bodies across the central Amazon basin during the daytime. However, both MYNN2.5 and MYNN3 schemes are the exception, in which predicted a homogeneous and deeper PBLH distribution. The QNSE scheme produces the deepest PBL in comparison with other PBL schemes.

5 CONCLUSIONS

The predictability of the Amazonian PBL was assessed using the state-of-the-art ARW model experiments and compared with in situ observations from the GOAmazon2014/5 field campaign. The performance of five nonlocal PBL parameterization schemes (i.e., ACM2, MRF, SH, YSU, QNSE) and six local PBL schemes (i.e., BouLac, GBM, MYNN2.5, MYNN3, MYJ, UW) was compared over the central Amazon basin focusing on the prediction of surface meteorological variables, turbulent fluxes, and both PBL depth and vertical structure. Short-term forecasts with the eleven PBL schemes were conducted for 72-h periods from the GOAmazon2014/5 IOPs covering the rainy and dry seasons of both typical (2014) and ENSO-influenced (2015) years. Several differences were found amongst forecasts using the evaluated PBL schemes revealing uncertainties from the numerical experiments.

The principal results are outlined below:

1. Nonlocal PBL schemes better predicted the T_2 than local PBL schemes in most of the evaluated periods (MRF in IOP1, YSU in IOP2, ACM2 in IOP3, and MYNN2.5 in IOP4). In contrast, the RH_2 was better predicted in all periods by local PBL schemes (MYJ in IOP1, MYNN3 in both IOP2 and IOP4, and GBM in IOP3). This pattern of better prediction by local PBL schemes also occurred in the case of U_{10} (UW in both IOP1 and IOP3, MYJ in IOP2, and MYNN3 in IOP4). The comparison of performance indicators amongst the IOPs reveals that both T_2 and RH_2 are better predicted than U_{10} suggesting that thermodynamical processes are better depicted in the surface layer than mechanical ones.

2. In the case of precipitation, in both the 2014 and 2015 rainy seasons the numerical experiments were unable to depict the rainfall episodes in timing and location. The analysis of the daily accumulated precipitation spatial fields for rainy seasons revealed that the model, independently of the PBL scheme option, could not depict the evolution of the convective system which brought major differences between predicted and observed weather variables. Both studied dry seasons were better predicted than rainy seasons, probably due to the non-presence of rainfall. The major differences seen between forecasts and observations for the dry seasons occurred when the model predicted non-observed (spurious) precipitation.

3. The available net radiation for daytime conditions during the IOP2 is predominantly partitioned in LE, which is better predicted than H. In general, all PBL schemes overestimated the daytime H. The BouLac scheme better predicted the

H, while the QNSE scheme better predicted the LE for the IOP2. In contrast, the available net radiation during the 2015 dry season was predominantly converted in H. The MYNN3 scheme better predicted the H, while the UW scheme better predicted the LE for the IOP3. The visual analysis for momentum flux showed that in general for both the 2014 and 2015 dry seasons the PBL schemes overestimated the observations during the daytime indicating excessive mechanical turbulence and mixing in the models.

4. The PBLH is better predicted during the daytime rather than at night. A general analysis considering all cases reveals that local PBL schemes presented a better performance during the daytime (MYJ in IOP1, MYNN3 in IOP2, MYNN2.5 in both IOP3 and IOP4), while a nonlocal PBL scheme during the nighttime in most of the studied periods (SH in IOP1, IOP3, and IOP4, with local MYNN2.5 scheme in IOP2). The differences found between observations and predictions can be attributed to the excessive vertical mixing in the model as well as incorrect methods of PBLH detection.

5. The thermodynamic structures (θ and q profiles) are better predicted during the well-developed CBL stage (14:00 LT) than during the development stage (11:00 LT). All PBL schemes showed in general a good agreement with observations during the SBL stage (02:00 LT), with predictions presenting major differences from observations mainly on the first day of forecast. This pattern corroborates the better prediction of the diurnal PBLH in comparison with nocturnal PBLH. Nonlocal PBL schemes, mainly the ACM2 and MRF schemes, tend to produce warmer and drier conditions near-surface and colder and wetter conditions above the PBL top during the daytime, which is certainly associated with the nonlocal mixing and entrainment processes incorporated in their formulations. All PBL schemes showed difficulties in the prediction of U profiles.

6. There are no observations to indicate which PBL scheme better reproduced the PBLH distribution over the domain. However, the predictions may be useful to show the PBLH distribution and corresponding differences produced amongst PBL schemes. The nighttime PBLH spatial fields revealed that nonlocal PBL schemes are influenced by the basin hydrography, while the local PBL schemes are lesser influenced. Both local GBM and MYJ schemes showed a homogeneous and shallower PBLH distribution at night independently of the evaluated period. The local PBL schemes showed to be relatively influenced by the large water bodies present in the central Amazon basin during the daytime. On the other hand, the nonlocal PBL

schemes notably depicted the basin hydrography in their PBLH distributions. In general, the PBL schemes predicted a deeper (lower) PBLH over the land and a lower (deeper) PBLH over water bodies during the daytime (nighttime).

As the main conclusion of this study, we can say that the PBL schemes predicted the diurnal cycles and overall variations of weather variables, eddy covariance fluxes, and PBL features with correspondence to observations, however, presenting significant differences in magnitude. There is no single PBL scheme that was the best for all investigated variables which makes the indication of the best overall model setup difficult, on the other hand, the best PBL scheme to predict each variable under a specific condition has been identified. The model is capable to predict the dry seasons with better quality than rainy seasons. Probably, this is linked to the non-capability of the model to represent convection during the rainy season. This impacts the correct representation of the atmosphere, which brought differences between forecasts and observations. The daytime PBL is better predicted than the nocturnal counterpart, which was expected due to the well-known difficulty of PBL schemes to represent the nocturnal SBLs.

Future studies should investigate the impact of microphysics and cumulus schemes since the PBL schemes did not show great differences in daily precipitation. Further investigations using a single-column approach (one-dimensional modeling) to exclude real-world complexities and focus purely on PBL processes of both SBL and CBL over the Amazon rainforest may reveal new features of these schemes. In addition, focus on evaluating the vertical profiles of the diffusion coefficients (K_m, K_h). Moreover, apply the PBLH diagnostics from independent methods like bulk Richardson number, parcel method, or potential temperature gradient method by using the predicted weather variables. An ensemble-based approach may be applied due to the case-to-case variability regarding the performance of PBL schemes. Furthermore, investigate the sensibility and impact of the initial conditions, especially those related to the turbulent length scales. Note that, all PBL schemes were conceptualized and designed under different environments from the Amazon basin consequently they are not adjusted to work there. This could be investigated to set up the mixing length scales adequately for the Amazon basin, optimizing each PBL scheme.

REFERENCES

ANABOR, V.; PUHALES, F. S.; PIVA, E. D.; ACEVEDO, O. C. Parametrização convectivas e simulação explícita: testes de sensibilidade para sistemas convectivos amazônicos. **Ciência e Natura**, v. 38, p. 467–476, 2016. 2, 21

ANDREAE, M. O. et al. The Amazon tall tower observatory (atto): overview of pilot measurements on ecosystem ecology, meteorology, trace gases, and aerosols. **Atmospheric Chemistry and Physics**, v. 15, n. 18, p. 10723–10776, 2015. 2

ANGEVINE, W. M.; JIANG, H.; MAURITSEN, T. Performance of an eddy diffusivity–mass flux scheme for shallow cumulus boundary layers. **Monthly Weather Review**, v. 138, n. 7, p. 2895–2912, 2010. 1, 2

ARAVIND, A.; SRINIVAS, C.; SHRIVASTAVA, R.; HEGDE, M.; SESHADRI, H.; MOHAPATRA, D. Simulation of atmospheric flow field over the complex terrain of kaiga using wrf: sensitivity to model resolution and pbl physics. **Meteorology and Atmospheric Physics**, v. 134, n. 1, p. 1–25, 2022. 2

BELA, M.; LONGO, K.; FREITAS, S.; MOREIRA, D.; BECK, V.; WOFSY, S.; GERBIG, C.; WIEDEMANN, K.; ANDREAE, M.; ARTAXO, P. Ozone production and transport over the Amazon basin during the dry-to-wet and wet-to-dry transition seasons. **Atmospheric Chemistry and Physics**, v. 15, n. 2, p. 757–782, 2015. 3, 21

BISCARO, T. S.; MACHADO, L. A.; GIANGRANDE, S. E.; JENSEN, M. P. What drives daily precipitation over the central Amazon? differences observed between wet and dry seasons. **Atmospheric Chemistry and Physics**, v. 21, n. 9, p. 6735–6754, 2021. 3, 26

BLACKADAR, A. K. The vertical distribution of wind and turbulent exchange in a neutral atmosphere. **Journal of Geophysical Research**, v. 67, n. 8, p. 3095–3102, 1962. 9, 11

BOPAPE, M.-J. M.; WAITOLO, D.; PLANT, R. S.; PHADULI, E.; NKONDE, E.; SIMFUKWE, H.; MKANDAWIRE, S.; RAKATE, E.; MAISHA, R. Sensitivity of simulations of zambian heavy rainfall events to the atmospheric boundary layer schemes. **Climate**, v. 9, n. 2, p. 38, 2021. 1

BOUGEAULT, P.; LACARRERE, P. Parameterization of orography-induced turbulence in a mesobeta–scale model. **Monthly Weather Review**, v. 117, n. 8, p. 1872–1890, 1989. 1, 2, 8, 10

BRETHERTON, C. S.; PARK, S. A new moist turbulence parameterization in the community atmosphere model. **Journal of Climate**, v. 22, n. 12, p. 3422–3448, 2009. 8, 13

CARNEIRO, R.; FISCH, G.; NEVES, T.; SANTOS, R.; SANTOS, C.; BORGES, C. Nocturnal boundary layer erosion analysis in the Amazon using large-eddy simulation during goAmazon project 2014/5. **Atmosphere**, v. 12, n. 2, p. 240, 2021. 2

CARNEIRO, R. G.; FISCH, G. Observational analysis of the daily cycle of the planetary boundary layer in the central Amazon during a non-el niño year and el niño year (goAmazon project 2014/5). **Atmospheric Chemistry and Physics**, v. 20, n. 9, p. 5547–5558, 2020. 2, 26

CARNEIRO, R. G.; FISCH, G.; BORGES, C. K.; HENKES, A. Erosion of the nocturnal boundary layer in the central Amazon during the dry season. **Acta Amazonica**, v. 50, p. 80–89, 2019. 2

CHAMECKI, M.; FREIRE, L. S.; DIAS, N. L.; CHEN, B.; DIAS-JUNIOR, C. Q.; MACHADO, L. A. T.; SÖRGEL, M.; TSOKANKUNKU, A.; ARAÚJO, A. C. d. Effects of vegetation and topography on the boundary layer structure above the Amazon forest. **Journal of the Atmospheric Sciences**, v. 77, n. 8, p. 2941–2957, 2020. 3

COHEN, A. E.; CAVALLO, S. M.; CONIGLIO, M. C.; BROOKS, H. E. A review of planetary boundary layer parameterization schemes and their sensitivity in simulating southeastern us cold season severe weather environments. **Weather and Forecasting**, v. 30, n. 3, p. 591–612, 2015. 2, 6, 14, 23

DEARDORFF, J. W. Numerical investigation of neutral and unstable planetary boundary layers. **Journal of Atmospheric Sciences**, v. 29, n. 1, p. 91–115, 1972. 6

DYER, A. A review of flux-profile relationships. **Boundary-Layer Meteorology**, v. 7, n. 3, p. 363–372, 1974. 18

DZEBRE, D. E.; ADARAMOLA, M. S. A preliminary sensitivity study of planetary boundary layer parameterisation schemes in the weather research and forecasting model to surface winds in coastal ghana. **Renewable Energy**, v. 146, p. 66–86, 2020. 1, 2, 6, 23

FERNANDEZ, J. INPE CPTEC-WRF (CPT-WRF) Version 1.1. p. 00–34, 11 2020. Available from https://www.researchgate.net/publication/349641316_INPE_CPTEC-WRF_CPT-WRF_Version_11. 29

FISCH, G.; ROCHA, E.; SOUZA, S.; CULF, A.; NOBRE, C.; ROCHA, H. D.; LYRA, R.; COSTA, A.; UBARANA, V.; CALVET, J.; WRIGHT, I. **Pre-LBA Rondonia Boundary Layer Experiment (RBLE) Data**. ORNL Distributed Active Archive Center, 2009. Available from: <http://daac.ornl.gov/cgi-bin/dsviewer.pl?ds_id=917>. 2

GARSTANG, M. et al. The Amazon boundary-layer experiment (able 2b): A meteorological perspective. **Bulletin of the American Meteorological Society**, v. 71, n. 1, p. 19–32, 1990. 2

GHOLAMI, S.; GHADER, S.; KHALEGHI-ZAVAREH, H.; GHAFARIAN, P. Sensitivity of wrf-simulated 10 m wind over the persian gulf to different boundary conditions and pbl parameterization schemes. **Atmospheric Research**, v. 247, p. 105147, 2021. 2, 24

GIANGRANDE, S. E.; WANG, D.; MECHEM, D. B. Cloud regimes over the Amazon basin: perspectives from the GOAmazon2014/5 campaign. **Atmospheric Chemistry and Physics**, v. 20, n. 12, p. 7489–7507, 2020. 3

GRENIER, H.; BRETHERTON, C. S. A moist pbl parameterization for large-scale models and its application to subtropical cloud-topped marine boundary layers. **Monthly Weather Review**, v. 129, n. 3, p. 357–377, 2001. 1, 2, 8, 10, 11

HACKEROTT, J. **Momentum fluxes in the marine atmospheric surface layer: a study on the Southwestern Atlantic Ocean**. PhD Thesis (PhD) — Universidade de São Paulo, São Paulo., 2018. Available from: <https://bityli.com/TqeYX>. 7

HARIPRASAD, K.; SRINIVAS, C. V.; SINGH, A. B.; RAO, S. V. B.; BASKARAN, R.; VENKATRAMAN, B. Numerical simulation and intercomparison of boundary layer structure with different pbl schemes in wrf using experimental observations at a tropical site. **Atmospheric Research**, v. 145, p. 27–44, 2014. 23

HARRISS, R. et al. The Amazon boundary layer experiment (able 2a): Dry season 1985. **Journal of Geophysical Research: Atmospheres**, v. 93, n. D2, p. 1351–1360, 1988. 2

HEGARTY, J. et al. **Evaluating WRF simulations of planetary boundary layer processes during the Baltimore–Washington, DC DISCOVER-AQ Field Campaign**. 2017. Available from: <https://ams.confex.com/ams/97Annual/webprogram/Paper313073.html>. 45

HENKES, A.; FISCH, G.; MACHADO, L. A. T.; CHABOUREAU, J.-P. Morning boundary layer conditions for shallow to deep convective cloud evolution during the dry season in the central Amazon. **Atmospheric Chemistry and Physics Discussions**, p. 1–29, 2021. 2

HERSBACH, H. et al. The era5 global reanalysis. **Quarterly Journal of the Royal Meteorological Society**, v. 146, n. 730, p. 1999–2049, 2020. 26

HOLTSLAG, A.; BOVILLE, B. Local versus nonlocal boundary-layer diffusion in a global climate model. **Journal of Climate**, v. 6, n. 10, p. 1825–1842, 1993. 14, 18

HOLTSLAG, A.; MOENG, C.-H. Eddy diffusivity and countergradient transport in the convective atmospheric boundary layer. **Journal of the Atmospheric Sciences**, v. 48, n. 14, p. 1690–1698, 1991. 14

HOLTSLAG, B.; STEENEVELD, G.-J. Single column modeling of atmospheric boundary layers and the complex interactions with the land surface. In: MEYERS, R. (Ed.). **Extreme environmental events**. [S.l.]: Springer, 2021. p. 844–857. 6, 7, 8, 9

HONG, S.-Y.; NOH, Y.; DUDHIA, J. A new vertical diffusion package with an explicit treatment of entrainment processes. **Monthly Weather Review**, v. 134, n. 9, p. 2318–2341, 2006. 1, 2, 7, 15, 16, 29

HONG, S.-Y.; PAN, H.-L. Nonlocal boundary layer vertical diffusion in a medium-range forecast model. **Monthly Weather Review**, v. 124, n. 10, p. 2322–2339, 1996. 1, 2, 7, 14

HU, X.-M.; NIELSEN-GAMMON, J. W.; ZHANG, F. Evaluation of three planetary boundary layer schemes in the wrf model. **Journal of Applied Meteorology and Climatology**, v. 49, n. 9, p. 1831–1844, 2010. 1, 23

IACONO, M. J.; DELAMERE, J. S.; MLAWER, E. J.; SHEPHARD, M. W.; CLOUGH, S. A.; COLLINS, W. D. Radiative forcing by long-lived greenhouse gases: calculations with the AER radiative transfer models. **Journal of Geophysical Research: Atmospheres**, v. 113, n. D13, 2008. 29

JAHN, D. E.; TAKLE, E. S.; GALLUS, W. A. Wind-ramp-forecast sensitivity to closure parameters in a boundary-layer parametrization scheme. **Boundary-Layer Meteorology**, v. 164, n. 3, p. 475–490, 2017. 9

JANJIC, Z. Nonsingular implementation of the mellor–yamada level 2.5 scheme in the ncep meso model. **NCEP Office Note**, v. 436, 01 2002. Available from: <https://repository.library.noaa.gov/view/noaa/11409/noaa_11409_DS1.pdf>. 11, 12

JANJIĆ, Z. I. The step-mountain coordinate: physical package. **Monthly Weather Review**, v. 118, n. 7, p. 1429–1443, 1990. 1, 2, 8, 11

_____. The step-mountain eta coordinate model: further developments of the convection, viscous sublayer, and turbulence closure schemes. **Monthly Weather Review**, v. 122, n. 5, p. 927–945, 1994. 8, 11

JANKOV, I.; JR, W. A. G.; SEGAL, M.; KOCH, S. E. Influence of initial conditions on the wrf–arw model qpf response to physical parameterization changes. **Weather and Forecasting**, v. 22, n. 3, p. 501–519, 2007. 27

JIA, W.; ZHANG, X. The role of the planetary boundary layer parameterization schemes on the meteorological and aerosol pollution simulations: a review. **Atmospheric Research**, v. 239, p. 104890, 2020. 2, 23

JIMÉNEZ, P. A.; DUDHIA, J.; GONZÁLEZ-ROUCO, J. F.; NAVARRO, J.; MONTÁVEZ, J. P.; GARCÍA-BUSTAMANTE, E. A revised scheme for the wrf surface layer formulation. **Monthly Weather Review**, v. 140, n. 3, p. 898–918, 2012. 29

JO, H.-Y. et al. A case study of heavy pm2. 5 secondary formation by n2o5 nocturnal chemistry in seoul, korea in january 2018: model performance and error analysis. **Atmospheric Research**, v. 266, p. 105951, 2022. 2

KAUFMANN, T.; FISCH, G. Validação do modelo les palm por meio de dados de radiosondagens e de aeronave coletados durante o experimento goAmazon. **Ciência e Natura**, v. 38, p. 34–40, 2016. 2

KEELER, E.; COULTER, R.; KYROUAC, J. **Balloon-Borne Sounding System (SONDEWNPN)**. 2014. Available from: <https://dx.doi.org/10.5439/1021460>. 26

KLEMP, J. B.; SKAMAROCK, W. C.; DUDHIA, J. Conservative split-explicit time integration methods for the compressible nonhydrostatic equations. **Monthly Weather Review**, v. 135, n. 8, p. 2897–2913, 2007. 26

KYROUAC, J.; SPRINGSTON, S. **Meteorological Measurements associated with the Aerosol Observing System (AOSMET)**. 2014. Available from: <https://dx.doi.org/10.5439/1025153>. 26

LANGE, A. D.; NAIDOO, M.; GARLAND, R. M.; DYSON, L. L. Sensitivity of meteorological variables on planetary boundary layer parameterization schemes in the wrf-arw model. **Atmospheric Research**, Elsevier, v. 247, p. 105214, 2021. 1, 2

LANGE, A. de; NAIDOO, M.; GARLAND, R. M.; DYSON, L. L. The sensitivity of simulated surface-level pollution concentrations to wrf-arw-model pbl parameterisation schemes over the highveld of South Africa. **Atmospheric Research**, v. 254, p. 105517, 2021. 1, 2, 24

LIU, S.; LIANG, X.-Z. Observed diurnal cycle climatology of planetary boundary layer height. **Journal of Climate**, v. 23, n. 21, p. 5790–5809, 2010. 1

LOUIS, J.-F. A parametric model of vertical eddy fluxes in the atmosphere. **Boundary-Layer Meteorology**, v. 17, n. 2, p. 187–202, 1979. 1, 2, 7, 8

MACHADO, L. A. T. et al. How weather events modify aerosol particle size distributions in the Amazon boundary layer. **Atmospheric Chemistry and Physics Discussions**, p. 1–31, 2021. 3

MARONEZE, R.; ACEVEDO, O. C.; COSTA, F. D.; PUHALES, F. S.; ANABOR, V.; LEMES, D. N.; MORTARINI, L. How is the two-regime stable boundary layer reproduced by the different turbulence parametrizations in the weather research and forecasting model? **Boundary-Layer Meteorology**, v. 178, n. 3, p. 383–413, 2021. 12, 24

MARTIN, S. T. et al. Introduction: observations and modeling of the Green Ocean Amazon (GOAmazon2014/5). **Atmospheric Chemistry and Physics**, v. 16, n. 8, p. 4785–4797, 2016. 2, 25

MATHER, J. H.; VOYLES, J. W. The arm climate research facility: a review of structure and capabilities. **Bulletin of the American Meteorological Society**, v. 94, n. 3, p. 377–392, 2013. xv, 25

MEDEIROS, A. S. et al. Power plant fuel switching and air quality in a tropical, forested environment. **Atmospheric Chemistry and Physics**, v. 17, n. 14, p. 8987–8998, 2017. 3, 21

MELLOR, G. L.; YAMADA, T. A hierarchy of turbulence closure models for planetary boundary layers. **Journal of Atmospheric Sciences**, v. 31, n. 7, p. 1791–1806, 1974. 8, 9, 12

_____. Development of a turbulence closure model for geophysical fluid problems. **Reviews of Geophysics**, v. 20, n. 4, p. 851–875, 1982. 1, 2, 8, 11

MORRIS, V.; BRIAN. **Boundary-layer height data with CEIL (CEILPBLHT)**. 2014. Available from: <https://dx.doi.org/10.5439/1021460>. 26

NAKANISHI, M.; NIINO, H. An improved mellor–yamada level-3 model: its numerical stability and application to a regional prediction of advection fog. **Boundary-Layer Meteorology**, v. 119, n. 2, p. 397–407, 2006. 8, 12

_____. Development of an improved turbulence closure model for the atmospheric boundary layer. **Journal of the Meteorological Society of Japan. Serie II**, v. 87, n. 5, p. 895–912, 2009. 1, 2, 8, 12

NASCIMENTO, J. P. et al. Aerosols from anthropogenic and biogenic sources and their interactions–modeling aerosol formation, optical properties, and impacts over the central Amazon basin. **Atmospheric Chemistry and Physics**, v. 21, n. 9, p. 6755–6779, 2021. 3, 22

NOH, Y.; CHEON, W. G.; HONG, S.; RAASCH, S. Improvement of the k-profile model for the planetary boundary layer based on large eddy simulation data. **Boundary-Layer Meteorology**, v. 107, n. 2, p. 401–427, 2003. 14

OLAFSSON, H.; BAO, J.-W. **Uncertainties in numerical weather prediction**. [S.l.: s.n.], 2020. 1, 6

OLIVEIRA, A. P.; FITZJARRALD, D. R. The Amazon river breeze and the local boundary layer: I. observations. **Boundary-Layer Meteorology**, v. 63, n. 1, p. 141–162, 1993. 2

PARK, S.-H.; SKAMAROCK, W. C.; KLEMP, J. B.; FOWLER, L. D.; DUDA, M. G. Evaluation of global atmospheric solvers using extensions of the jablonowski and williamson baroclinic wave test case. **Monthly Weather Review**, v. 141, n. 9, p. 3116–3129, 2013. 26

PENG, Y.; WANG, H.; ZHANG, X.; ZHAO, T.; JIANG, T.; CHE, H.; ZHANG, X.; ZHANG, W.; LIU, Z. Impacts of pbl schemes on pm2. 5 simulation and their responses to aerosol-radiation feedback in grapes_cuace model during severe haze episodes in jing-jin-ji, china. **Atmospheric Research**, v. 248, p. 105268, 2021. 2

PERGAUD, J.; MASSON, V.; MALARDEL, S.; COUVREUX, F. A parameterization of dry thermals and shallow cumuli for mesoscale numerical weather prediction. **Boundary-Layer Meteorology**, v. 132, n. 1, p. 83–106, 2009. 20, 21

PLEIM, J. E. A combined local and nonlocal closure model for the atmospheric boundary layer. part i: model description and testing. **Journal of Applied Meteorology and Climatology**, v. 46, n. 9, p. 1383–1395, 2007. 1, 2, 7, 8, 17, 20

_____. A combined local and nonlocal closure model for the atmospheric boundary layer. part ii: application and evaluation in a mesoscale meteorological model. **Journal of Applied Meteorology and Climatology**, v. 46, n. 9, p. 1396–1409, 2007. 8, 17, 19

PLEIM, J. E.; CHANG, J. S. A non-local closure model for vertical mixing in the convective boundary layer. **Atmospheric Environment. Part A. General Topics**, v. 26, n. 6, p. 965–981, 1992. 17

POPE, S. B. **Turbulent flows**. [S.l.]: Cambridge University Press, 2000. 6

POWERS, J. G. et al. The weather research and forecasting model: overview, system efforts, and future directions. **Bulletin of the American Meteorological Society**, v. 98, n. 8, p. 1717–1737, 2017. 2

RAFEE, S. A. A. et al. Assessing the impact of using different land cover classification in regional modeling studies for the manaus area, brazil. **Journal of Geoscience and Environment Protection**, v. 3, n. 06, p. 77, 2015. 3, 21

_____. Contributions of mobile, stationary and biogenic sources to air pollution in the Amazon rainforest: a numerical study with the wrf-chem model. **Atmospheric Chemistry and Physics**, v. 17, n. 12, p. 7977–7995, 2017. 3, 21

ROGERS, E.; BLACK, T.; FERRIER, B.; LIN, Y.; PARRISH, D.; DIMEGO, G. Changes to the ncep meso eta analysis and forecast system: increase in resolution, new cloud microphysics, modified precipitation assimilation, modified 3dvar analysis. **NWS Technical Procedures Bulletin**, v. 488, p. 15, 2001. 29

ROZANTE, J. R.; MOREIRA, D. S.; GONCALVES, L. G. G. de; VILA, D. A. Combining trmm and surface observations of precipitation: technique and validation over south america. **Weather and Forecasting**, v. 25, n. 3, p. 885–894, 2010. 47

SÁTYRO, Z. C.; FARIAS, C.; CANDIDO, L. A.; VEIGA, J. A. The relative and joint effect of rivers and urban area on a squall line in the central Amazonia. **Science of the Total Environment**, v. 755, p. 142178, 2021. 22

SEGURA, R.; BADIA, A.; VENTURA, S.; GILABERT, J.; MARTILLI, A.; VILLALBA, G. Sensitivity study of pbl schemes and soil initialization using the wrf-bep-bem model over a mediterranean coastal city. **Urban Climate**, v. 39, p. 100982, 2021. 2

SHIN, H. H.; HONG, S.-Y. Intercomparison of planetary boundary-layer parametrizations in the wrf model for a single day from cases-99. **Boundary-Layer Meteorology**, v. 139, n. 2, p. 261–281, 2011. 6, 23, 55

_____. Representation of the subgrid-scale turbulent transport in convective boundary layers at gray-zone resolutions. **Monthly Weather Review**, v. 143, n. 1, p. 250–271, 2015. 1, 2, 7, 8, 16

SHRIVASTAVA, M. et al. Urban pollution greatly enhances formation of natural aerosols over the Amazon rainforest. **Nature Communications**, v. 10, n. 1, p. 1–12, 2019. 3

SIEBESMA, A. P.; SOARES, P. M.; TEIXEIRA, J. A combined eddy-diffusivity mass-flux approach for the convective boundary layer. **Journal of the Atmospheric Sciences**, v. 64, n. 4, p. 1230–1248, 2007. 8

SKAMAROCK, W. C. et al. A description of the advanced research wrf model version 4. **National Center for Atmospheric Research: Boulder, CO, USA**, p. 145, 2019. 2, 6, 9, 12, 26, 27

SOARES, P.; MIRANDA, P.; SIEBESMA, A.; TEIXEIRA, J. An eddy-diffusivity/mass-flux parametrization for dry and shallow cumulus convection. **Quarterly Journal of the Royal Meteorological Society: A Journal of the Atmospheric Sciences, Applied Meteorology and Physical Oceanography**, v. 130, n. 604, p. 3365–3383, 2004. 1, 20

SRIVASTAVA, N.; BLOND, N. Impact of meteorological parameterization schemes on ctm model simulations. **Atmospheric Environment**, Elsevier, v. 268, p. 118832, 2022. 2

STENSRUD, D. J. **Parameterization schemes: keys to understanding numerical weather prediction models**. [S.l.]: Cambridge University Press, 2009. 1, 6, 9

STULL, R. B. **An introduction to boundary layer meteorology**. [S.l.]: Springer Science & Business Media, 1988. 1, 5, 6, 8

SUKORIANSKY, S.; GALPERIN, B.; PEROV, V. Application of a new spectral theory of stably stratified turbulence to the atmospheric boundary layer over sea ice. **Boundary-Layer Meteorology**, v. 117, n. 2, p. 231–257, 2005. 1, 2, 8, 20

SULLIVAN, R.; BILLESBACH, D.; KEELER, E.; ERMOLD, B. **Eddy Correlation Flux Measurement System (30ECOR)**. 2014. Available from: <https://dx.doi.org/10.5439/1025039>. 26

TAI, S.-L.; FENG, Z.; MA, P.-L.; SCHUMACHER, C.; FAST, J. D. Representations of precipitation diurnal cycle in the Amazon as simulated by observationally constrained cloud-system resolving and global climate models. **Journal of Advances in Modeling Earth Systems**, v. 13, n. 11, p. e2021MS002586, 2021. 3

TASTULA, E.-M.; LEMONE, M. A.; DUDHIA, J.; GALPERIN, B. The impact of the qnse-edmf scheme and its modifications on boundary layer parameterization in wrf: modelling of cases-97. **Quarterly Journal of the Royal Meteorological Society**, v. 142, n. 695, p. 1182–1195, 2016. 20, 21

TAYLOR, K. E. Summarizing multiple aspects of model performance in a single diagram. **Journal of Geophysical Research: Atmospheres**, v. 106, n. D7, p. 7183–7192, 2001. Available from: <https://doi.org/10.1029/2000JD900719>. 30, 42

TEWARI, N. M. et al. Implementation and verification of the unified noah land surface model in the wrf model (formerly paper number 17.5). In: CONFERENCE ON WEATHER ANALYSIS AND FORECASTING, 20. **Proceedings...** [S.l.], 2004. p. 11–15. 29

THERRY, G.; LACARRÈRE, P. Improving the eddy kinetic energy model for planetary boundary layer description. **Boundary-Layer Meteorology**, Springer, v. 25, n. 1, p. 63–88, 1983. 10

TROEN, I.; MAHRT, L. A simple model of the atmospheric boundary layer; sensitivity to surface evaporation. **Boundary-Layer Meteorology**, Springer, v. 37, n. 1, p. 129–148, 1986. 7, 14

TURNER, J. **Buoyancy effects in fluids**. [S.l.]: Cambridge University Press, 1973. 11

WANG, C. et al. Assessing the sensitivity of land-atmosphere coupling strength to boundary and surface layer parameters in the wrf model over Amazon. **Atmospheric Research**, v. 234, p. 104738, 2020. 2, 22, 24

WANG, C.; QIAN, Y.; DUAN, Q.; HUANG, M.; YANG, Z.; BERG, L. K.; JR, W. I. G.; FENG, Z.; LIU, J.; QUAN, J. Quantifying physical parameterization uncertainties associated with land-atmosphere interactions in the wrf model over Amazon. **Atmospheric Research**, v. 262, p. 105761, 2021. 2, 22, 24, 42

WANG, W.; SHEN, X.; HUANG, W. A comparison of boundary-layer characteristics simulated using different parametrization schemes. **Boundary-Layer Meteorology**, v. 161, n. 2, p. 375–403, 2016. 2, 24

WANG, Y.; SAYIT, H.; MAMTIMIN, A.; ZHU, J.; ZHOU, C.; HUO, W.; YANG, F.; YANG, X.; GAO, J.; ZHAO, X. Evaluation of five planetary boundary layer schemes in wrf over China's largest semi-fixed desert. **Atmospheric Research**, v. 256, p. 105567, 2021. 2

WICKER, L. J.; SKAMAROCK, W. C. Time-splitting methods for elastic models using forward time schemes. **Monthly Weather Review**, v. 130, n. 8, p. 2088–2097, 2002. 26

YANG, J.; TANG, Y.; HAN, S.; LIU, J.; YANG, X.; HAO, J. Evaluation and improvement study of the planetary boundary-layer schemes during a high pm2. 5 episode in a core city of bth region, China. **Science of The Total Environment**, v. 765, p. 142756, 2021. 1, 2

ZAVERI, R. A.; WANG, J.; FAN, J.; ZHANG, Y.; SHILLING, J. E.; ZELENYUK, A.; MEI, F.; NEWSOM, R.; PEKOUR, M.; TOMLINSON, J.; COMSTOCK, J. M.; SHRIVASTAVA, M.; FORTNER, E.; MACHADO, L. A. T.; ARTAXO, P.;

MARTIN, S. T. Rapid growth of anthropogenic organic nanoparticles greatly alters cloud life cycle in the Amazon rainforest. **Science Advances**, v. 8, 2022. 3

ZHANG, C.; WANG, Y. Projected future changes of tropical cyclone activity over the western north and south pacific in a 20-km-mesh regional climate model. **Journal of Climate**, v. 30, n. 15, p. 5923–5941, 2017. 29

ZHANG, C.; WANG, Y.; XUE, M. Evaluation of an e–ε and three other boundary layer parameterization schemes in the wrf model over the southeast pacific and the southern great plains. **Monthly Weather Review**, v. 148, n. 3, p. 1121–1145, 2020. 1, 2, 7, 9

ZHANG, D.; COMSTOCK, J.; MORRIS, V. Comparisons of planetary boundary layer height from ceilometer with arm radiosonde data. **Atmospheric Measurement Techniques Discussions**, p. 1–28, 2021. 26

ZHANG, X. Chapter 7 - subgrid turbulence mixing. In: ÓLAFSSON, H.; BAO, J.-W. (Ed.). **Uncertainties in numerical weather prediction**. [S.l.]: Elsevier, 2021. p. 205–227. 1, 5, 6